Spatial Scan Double Crystal Monochromator for JET (Diagnostic System KS2)[+]

C. Andelfinger, J. Fink, G. Fußmann, H. Krause,
H. Röhr, H.-B. Schilling, U. Schumacher
P. Becker, H. Siegert[++]
H. Belzig, A. Berghausen, R. Veigel, H. Zech[+++]

IPP 1/226 March 1984

MAX-PLANCK-INSTITUT FÜR PLASMAPHYSIK
8046 GARCHING BEI MÜNCHEN

MAX-PLANCK-INSTITUT FÜR PLASMAPHYSIK

GARCHING BEI MÜNCHEN

Spatial Scan Double Crystal Monochromator for JET (Diagnostic System KS2)[+]

C. Andelfinger, J. Fink, G. Fußmann, H. Krause,
H. Röhr, H.-B. Schilling, U. Schumacher

P. Becker, H. Siegert [++]

H. Belzig, A. Berghausen, R. Veigel, H. Zech [+++]

IPP 1/226 March 1984

[+] This work was done under Contract No. JE 2/9017 "Detailed Design of the Broadband X-ray Crystal Diagnostic System for JET"

[++] Physikalisch-Technische Bundesanstalt
3300 Braunschweig

[+++] Dornier System GmbH
7990 Friedrichshafen

Die nachstehende Arbeit wurde im Rahmen des Vertrages zwischen dem Max-Planck-Institut für Plasmaphysik und der Europäischen Atomgemeinschaft über die Zusammenarbeit auf dem Gebiete der Plasmaphysik durchgeführt.

IPP 1/226

C. Andelfinger, J. Fink,
G. Fußmann, H. Krause,
H. Röhr, H.-B. Schilling,
U. Schumacher

P. Becker, H. Siegert

H. Belzig, A. Berghausen,
R. Veigel, H. Zech

Spatial Scan Double Crystal Monochromator for JET (Diagnostic System KS2)

Abstract

The spatial dependence of the main impurity concentrations of the JET plasma can be determined by absolute radiation measurements in a wide spectral range using a double crystal monochromator device, which enables spatial scan over the minor plasma radius during a time interval short compared to the plasma energy confinement time. The report describes the engineering design and tests for a spatial scan double crystal spectrometer that fulfills the conditions of crystal orientation according to the Bragg condition, of continuous spatial scanning using a swivel motion around the axis defined by the two crystal centres and of operating during the hydrogen and the deuterium experimental phases of JET.

Contents

1. Introduction

One of the most important physics problems in present magnetic confinement experiments is the plasma impurity behaviour. The determination of the concentrations and the transport of impurities in high-temperature plasmas is an important task of plasma diagnostics and contributes much to the understanding of the plasma behaviour and the radiation losses.

Since at high electron temperatures as in JET plasmas most of the radiation is emitted in the soft X-ray region it is aimed at diagnosing the impurities by their appropriate X-ray spectral lines.

The main goal of the spatial scan soft X-ray monochromator is to determine the spatial dependence of the main impurity concentrations of the JET plasma by absolute radiation measurements in a wide spectral range to be spatially scanned over the minor plasma radius during a time interval short compared to the plasma energy confinement time and lifetime (discharge time). The monochromator should be able to operate during the hydrogen and the deuterium experimental phases of JET, but it will probably not be able to work during the D-T operation (the "active phase") of JET with its high neutron and gamma fluxes.

The present report treats the basic properties of the broadband spatial scan soft X-ray monochromator in section 2, followed by the discussion of the components of the monochromator and results of component tests in section 3, while section 4 presents the engineering design of the device.

Because of the similarity of this spatial scan double crystal monochromator (JET Diagnostic System KS2) with the active phase double crystal monochromator (JET Diagnostic System KS1) some sections are similar (but specifically different) to those in IPP/225.

2. Basic Properties of the Broadband Spatial Scan Soft X-Ray Monochromator

2.1 Spectral Range and Crystal Choice

The choice of the spectral range is influenced by the plasma parameters and the main impurities of interest. We roughly expect three groups of impurities:

1) The ubiquitous elements as oxygen, nitrogen, carbon or iron, which are mostly low-Z impurities;
2) the constituents of the wall material (INCONEL 600), which are predominantly nickel, chromium, iron and - at very low concentrations - carbon, manganese, sulfur, silicon and copper with mainly intermediate Z and
3) those elements as neon or argon that might be purposely added into the JET plasma as tracer elements for plasma diagnostics.

The fractional abundances f_z of the charge states of the main INCONEL constituents chromium, iron, and nickel as functions of the electron temperature T_e for coronal equilibrium as calculated by C. Breton et al. /1/ are given in Fig. 1, those for oxygen and the possibly added elements neon and argon in Fig. 2.

These graphs are examples of the charge state distributions of some of the impurity elements to be expected. They indicate that for the plasma centre at electron temperatures of several keV the low-Z impurities are completely ionized while for the medium-Z impurities hydrogen-, helium-, lithium- or beryllium-like transitions are to be expected. The plasma boundary region with its lower temperature is dominated by lower charge state transitions.

Most of these transitions belong to spectral lines in the wavelength region of about 1 Å to about 25 Å, which is accessible by crystal spectroscopy as, e.g., proposed in the broadband crystal spectrometer design study for JET /3/. The figures 3 to 5 give examples of the relation of several typical spectral lines that are expected to be emitted from intermediate and high electron temperature plasmas of JET. Fig. 3 illustrates that the most prominent hydrogen- and helium-like lines of oxygen and many spectral lines of lower charge-state

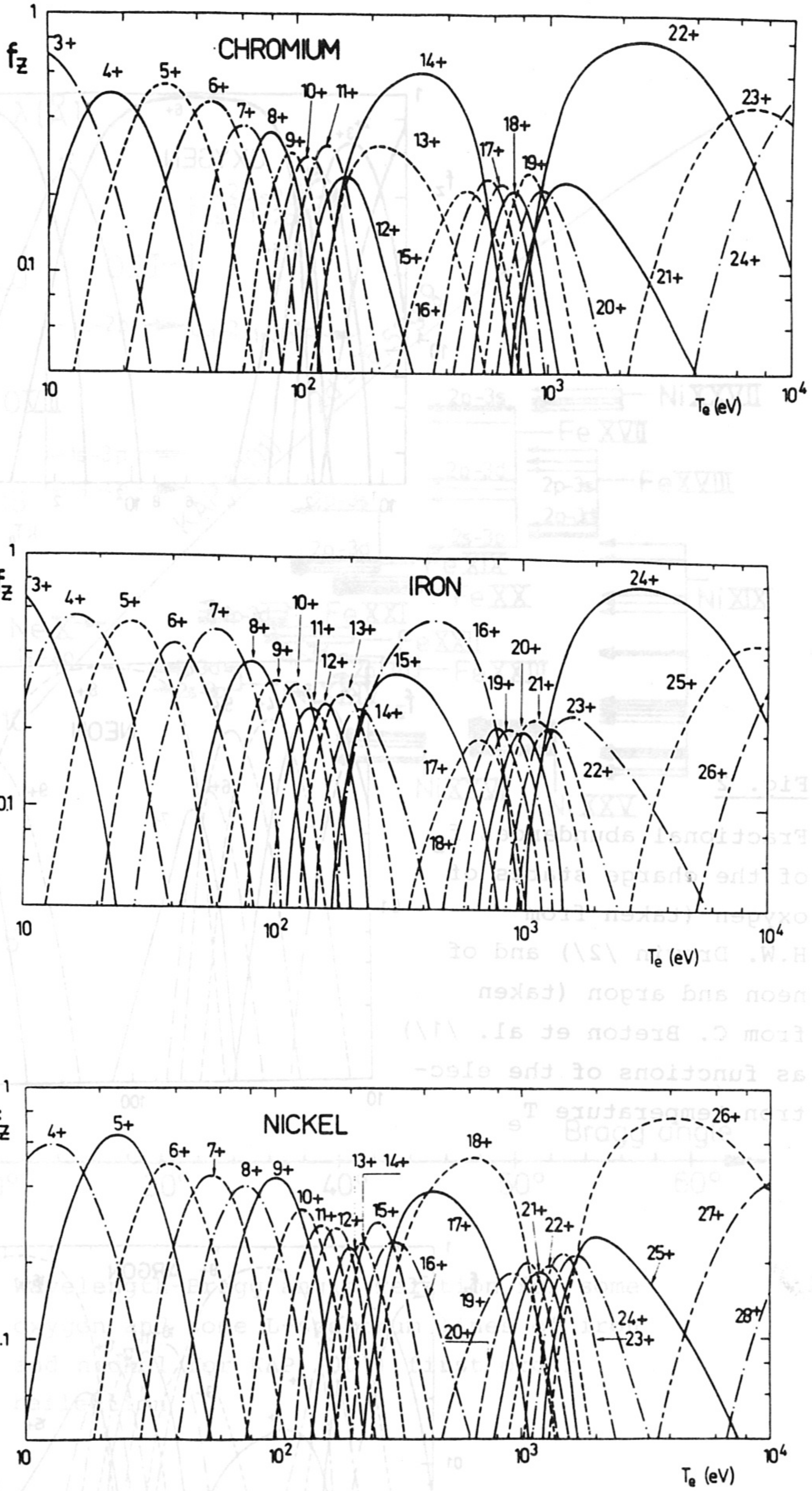

Fig. 1 Fractional abundances f_z of the charge states of chromium, iron, and nickel as functions of the electron temperature T_e (taken from C. Breton et al. /1/)

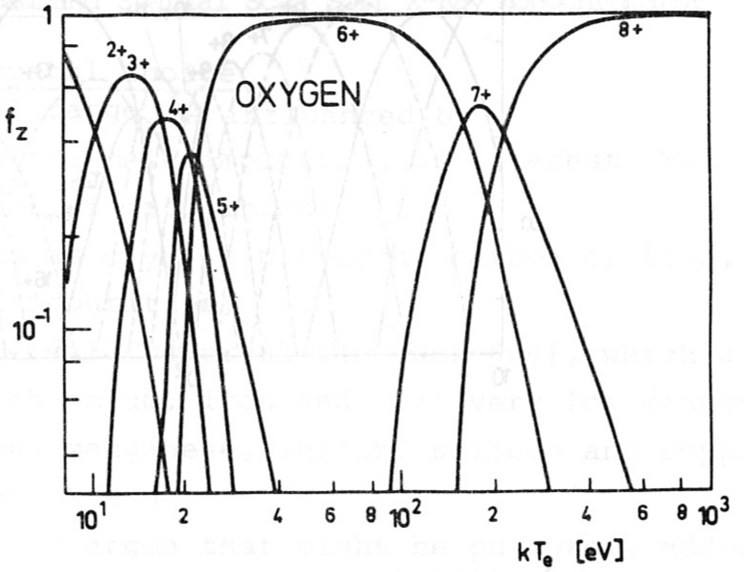

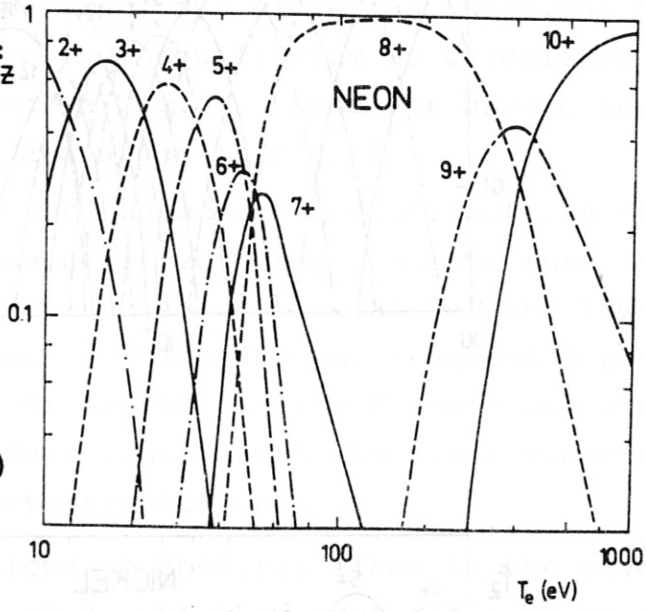

Fig. 2

Fractional abundances f_z of the charge states of oxygen (taken from H.W. Drawin /2/) and of neon and argon (taken from C. Breton et al. /1/) as functions of the electron temperature T_e

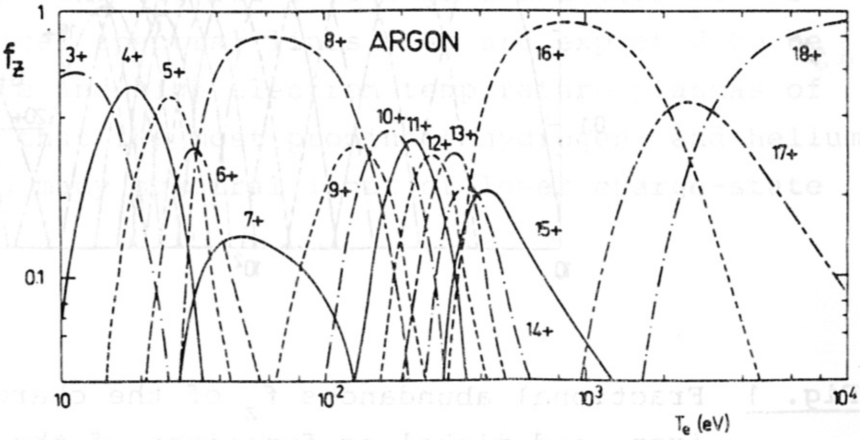

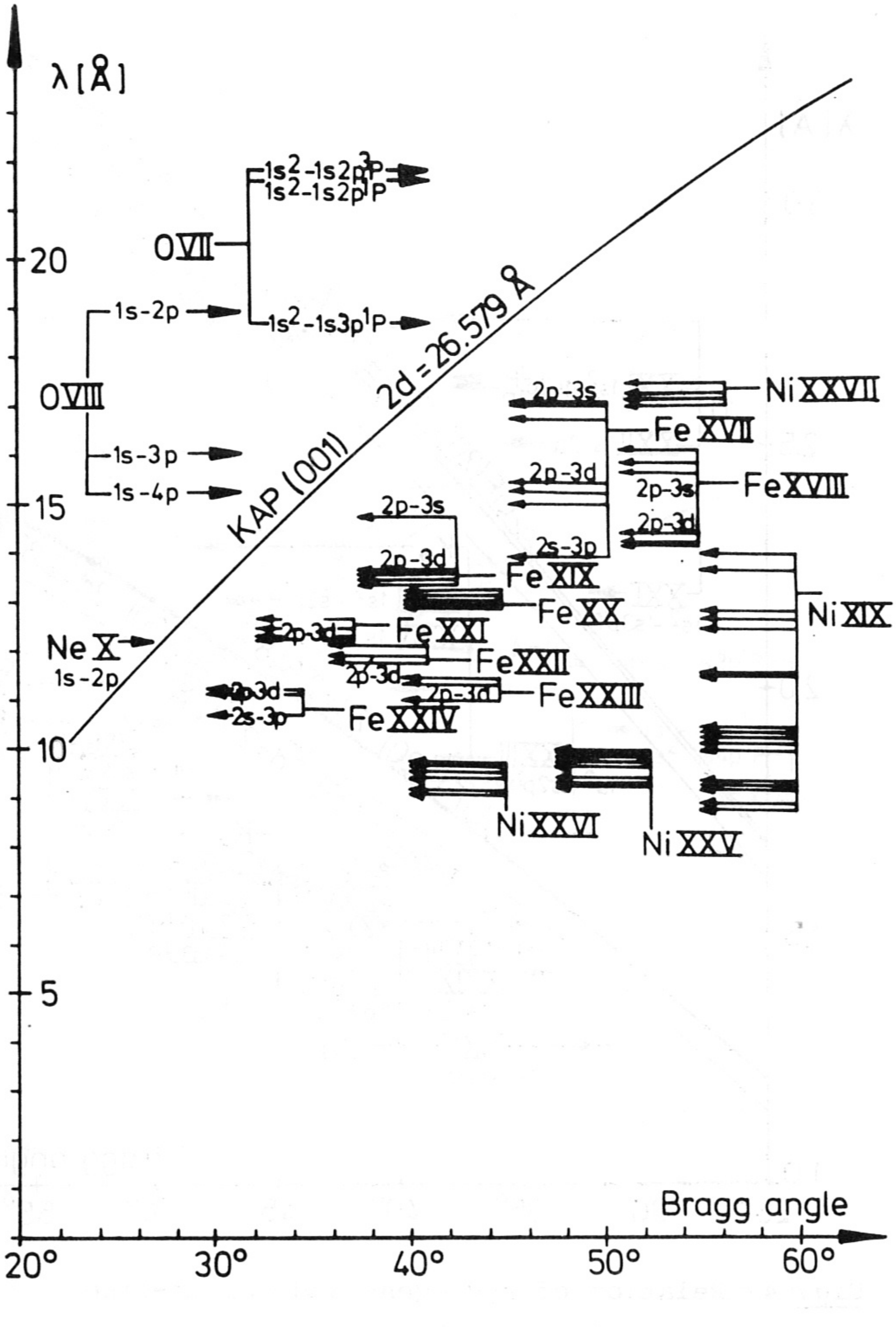

Fig. 3 Wavelength-Bragg angle relation for some oxygen and some L-spectrum lines of iron and nickel for KAP (001) first order reflection

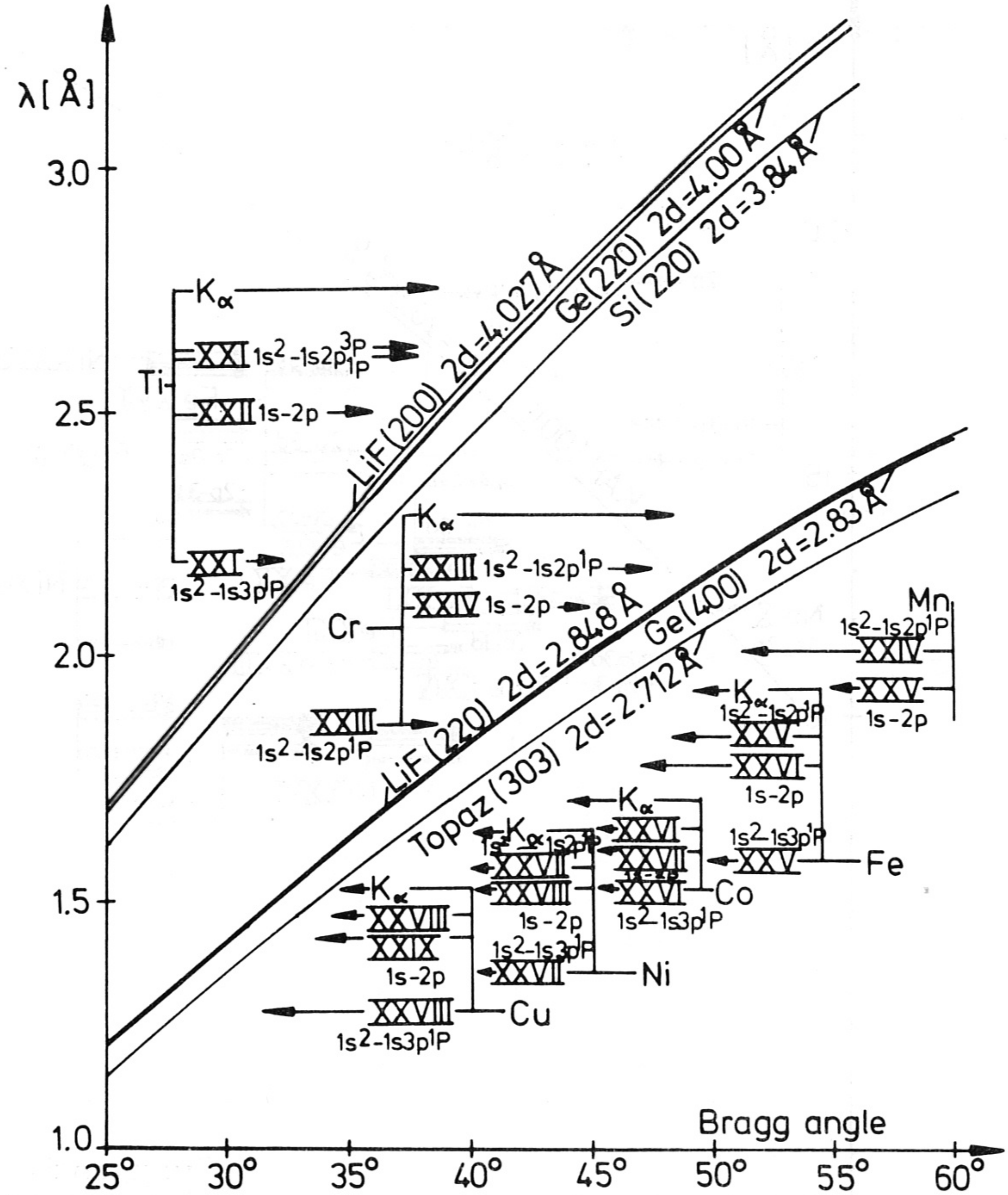

Fig. 4 Relation of hydrogen- and helium-like transitions to the Bragg angle

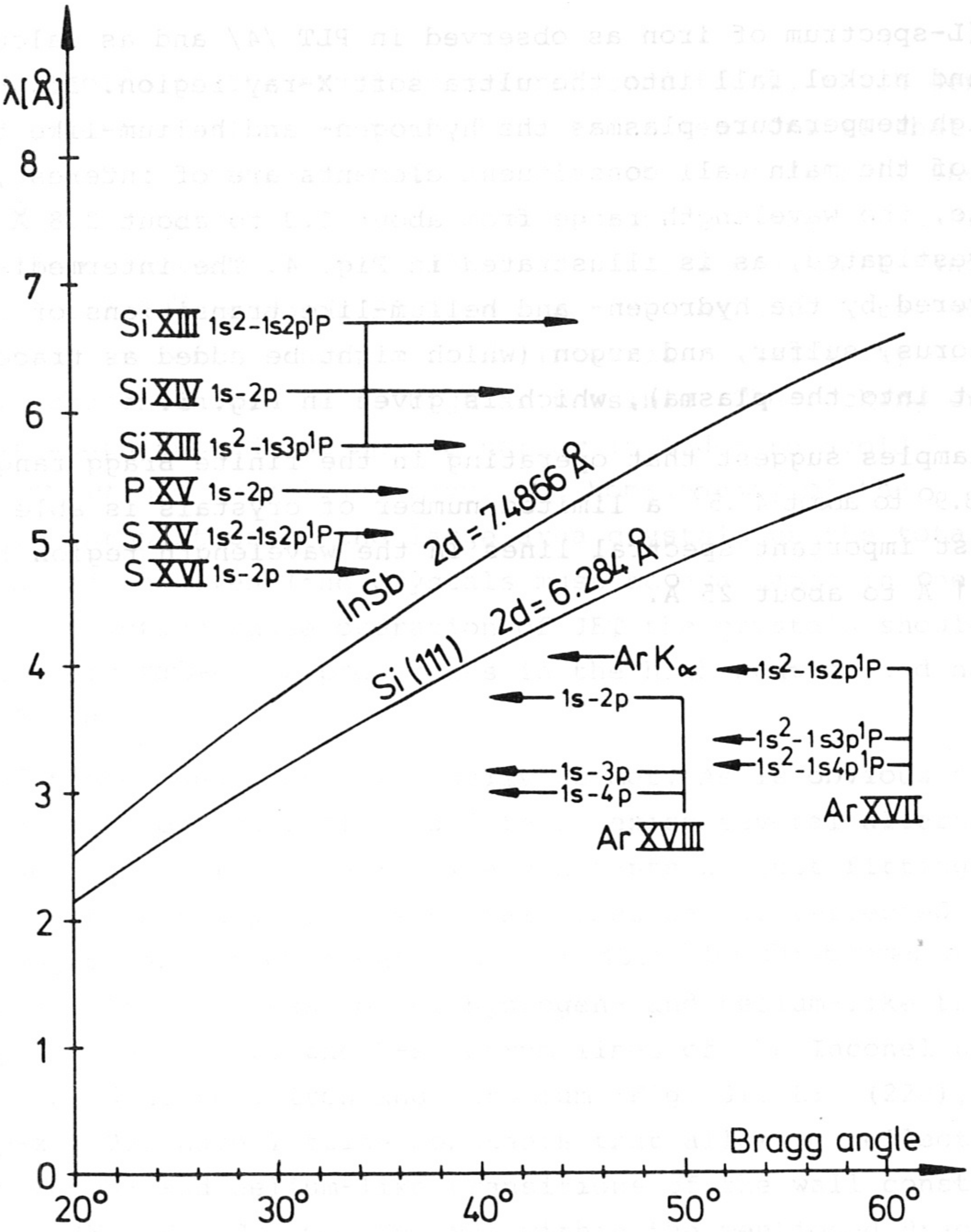

Fig. 5 Wavelength-Bragg angle relation of hydrogen- and helium-like transitions of intermediate-Z elements for first order reflection of InSb and Si(111)

iron (L-spectrum of iron as observed in PLT /4/ and as calculated /5/) and nickel fall into the ultra soft X-ray region. If, however, for high temperature plasmas the hydrogen- and helium-like transitions of the main wall constituent elements are of interest, for example, the wavelength range from about 1.3 to about 2.8 Å has to be investigated, as is illustrated in Fig. 4. The intermediate region is covered by the hydrogen- and helium-like transitions of silicon, phosphorus, sulfur, and argon (which might be added as tracer element into the plasma), which is given in Fig. 5.

The examples suggest that operating in the finite Bragg range of about 23.9° to about 45.5° a limited number of crystals is able to cover the most important spectral lines in the wavelength region from about 1 Å to about 25 Å.

For the choice of the crystals several conditions, which depend on the experimental parameters, have to be met. One is that the crystal lattice constant 2d should be such as to fulfill the Bragg condition for first order reflection in the wavelength and Bragg angle range envisaged, which asks for lattice constants ranging from about 2.5 Å to about 25 Å in order to get access to the above mentioned wavelength interval. The integral reflectivity of the crystal chosen should be as high as possible. The rocking curve angular width should not be too narrow in order to avoid non feasible mechanical accuracy. The homogeneity of the reflection properties of the large area crystals on the total surface should be given (the crystals must be available in the desired size). For active phase operation of JET the crystals should not change their reflection properties in the high neutron and hard X-ray fluxes.

Most of these conditions can easily be met. As is obvious from Figs. 3 to 5 some crystals - and there exist several alternatives to these (see /3/) - have lattice constants 2d just fitting the requirement that important spectral lines can be reflected in the Bragg angle range from about 23.9° to 45.5° for first order reflection. KAP (001) offers access to the hydrogen- and helium-like transitions of oxygen and e.g. to the L-spectrum lines of the Inconel 600 wall constituents nickel, iron and chromium (Fig. 3). LiF (220), Ge (400) or Topaz (303) have lattice constants that allow to reflect just the hydrogen- and helium-like transitions of the wall constituent elements (Ni, Fe, Cr, Co, Cu, Mn) within the mentioned Bragg angle interval, while LiF (200), Ge (220) or Si (220) have suitable lattice constants for the corresponding Ti-transitions (Fig. 4). For the intermediate-Z elements (Si, P, S) and for Ar, which might be arbitrarily added to the JET plasma for diagnostic reasons, InSb and Si (111) are appropriate crystals (Fig. 5).

The integral reflectivities of the crystals given as examples are relatively high (some are already listed in /3/): A. Burek /6/

gives values for the KAP (001) integral reflectivity of about $5 \cdot 10^{-5}$, while data for the integral reflectivity and the rocking curve widths, respectively, of the other crystals are found elsewhere /7,8,9,10,11/.

Concerning the rocking curve widths the crystals KAP (001) /6/ and InSb /7/ have large enough values, such that the conditions for mechanical accuracy are relatively moderate and hence crystal spectroscopy for low- and intermediate-Z elements (according to Figs. 3 and 5) can be performed without treatment of crystals. At a Bragg angle of 25° the rocking curve width is of the order of one arc minute /6/. However, for crystal spectroscopy in the few Å wavelength region (Fig. 4) most of the crystals have relatively narrow rocking curve widths /7,8/ and rocking curve "widening" methods /11/ have to be applied (see chapter 3.2), in order to meet the mechanical accuracy.

This latter group of crystals contains some with limited lattice perfection /12,13,14,15/, which might result in inhomogeneities of the reflection characteristics on the crystal surface and hence are unsuitable for double crystal monochromators. Mainly natural crystals (like e.g. LiF and Topaz) show these inhomogeneities /10,15/ (see chapter 3.2 on crystal tests). By abrading techniques /11/ and choice of individual crystal pairs, however, all reflection conditions can be fulfilled.

With respect to the resistance of the crystal reflection properties against radiation damage from high neutron and hard X-ray fluxes as well as from power dissipated on the crystal very little information is available in the literature.

For crystals like quartz very high neutron fluences ($> 10^{19}$ n/cm^2) are necessary to affect the X-ray reflectivity and line shape /16/. These fluences will by far not be reached at the crystal location for JET /3/. Organic crystals, however, like KAP might be influenced by high neutron fluences. Hence these crystals were tested in a reactor (see chapter 3.2 on crystal tests).

Radiation damage from X-ray energy dissipated on most of the crystal surfaces will not be expected for the JET experimental conditions since elsewhere radiation damage started not before about 4 $kW \cdot h \cdot cm^{-2}$ integrated radiation exposure /7/. Exceptions are organic crystals like PET, EDdT, ADP, SHA, KAP or RAP /17,18/, since they are highly temperature sensitive and suffer radiation damage when exposed for long period of time to an extensive X-ray beam. However, for the JET conditions of power densities of less than 0.2 $W\ cm^{-2}$ (which are comparable with the present power densities on the crystals at DORIS) no deleterious thermal effects should occur /20/.

Hence the question of radiation damage of KAP by neutrons and hard X-rays remains. However, in the D - D phase of JET these crystals can be replaced by Na-ß-alumina ($NaAl_{11}O_{17}$) with slightly smaller lattice constant (2d = 22.49 Å) than KAP, but high peak reflectivity and convenient rocking curve widths. Its stability to radiation is adequate and the crystals are almost perfect /18,19/.

Summarizing, for the three regions of interest, as roughly characterized by Figs. 3, 4 and 5, there exist first choices of crystals, KAP (001), LiF (220), and InSb, respectively, and alternatives, Na-ß-alumina, Ge (400), and Si (111), respectively (and many others).

2.2 General spatial scan monochromator configuration

The double crystal device was chosen as the monochromator configuration for reasons of relatively easy wavelength scan over a wide spectral range, of efficient shielding of the detector at fixed spatial position against high neutron and hard X-ray fluxes and mainly for fast spatial scan by crystal rotation around the beam axis. As proposed in /3/ the spatial scan double crystal monochromator should be located on top of vertical flange No. 3. Fig. 6 shows the general scheme of the monochromator. The Bragg angles of crystals 1 and 2 are set to the value corresponding to the desired wavelength. If crystal 1 is swivelled about the axis connecting both crystal centres the entering beam scans the minor plasma dimension as indi-

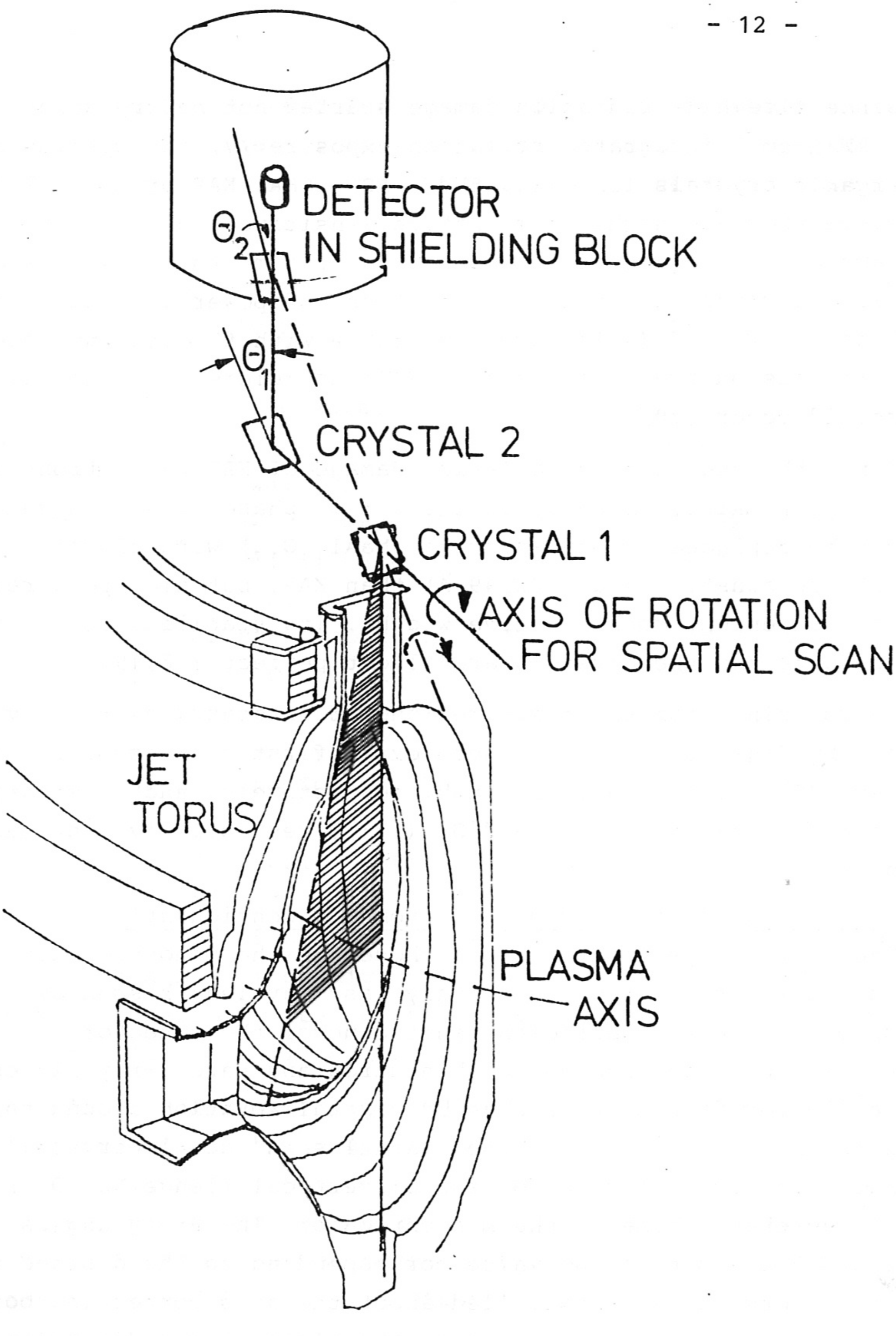

Fig. 6 Scheme of the spatial scan double crystal monochromator above vertical port No. 3 of JET

cated by the hatching.

The wavelength (and beam direction) is defined by crystal 2 in conjunction with a (low resolution) collimator. The spatial resolution is given by a collimator (perpendicularly oriented to the latter) in front of the detector in the shielding block, which also serves as neutron collimator for detector shielding reasons.

Both crystals and the collimator have to be placed in fixed relative orientation to each other in the spectrometer vacuum vessel. This vessel must be mechanically decoupled from the vertical JET flange (e.g. by a bellows) to avoid misalignment originating from forces in connection with major current disruptions. Moreover the vessel that contains the crystals and the crystal positioning mechanics should be thermally decoupled from the JET torus, because the crystals and the mechanics should not take part in the temperature excursions of the torus vessel.

Since the spectrometer vessel cannot be baked, it is separated from the torus vacuum system by a thin foil, in order to allow a moderate vacuum (in the order of 10^{-6} mbar) in the monochromator vessel with its fast swivelling mechanical components. The foil must be thin enough to allow high transmission for the soft X-rays to be detected, but thick enough to separate even atmospheric pressure from ultra-high vacuum with very low permeation rate. The detector is shielded against neutrons and gammas by a cylindrical shielding block on a platform supported by the transformer limbs, which platform also carries the monochromator vessel. The detector is designed as large area (about 100 x 100 mm^2) high count rate multiwire proportional counter without spatial resolution, using e.g. P10 as detector gas.

3. Results of Component Tests

Due to the small rocking curve widths of some crystals the overall mechanical inaccuracies of the monochromator must be below certain limits. These limits are set either by the condition that two neighbouring spectral lines have to be clearly separated, which normally can be fulfilled with angular tolerances being less than a few arc minutes, or that line profile measurements should be possible, where inaccuracies less than 20 arc seconds are demanded.

As a result of these considerations the aim was to perform tests in two different respects:
One test group was devoted to the determination of the mechanical accuracy of all components of the design that contribute to the Bragg angle. These are the longitudinal displacement table in quasi-static and fast motion and the rotation units with their corresponding incremental transducers. Most important is the simultaneous fulfilling of the Bragg angle condition of both crystals, to be determined especially for the control system operating.

The other group of tests was related to the optical properties of the crystals, especially their rocking curve widths and the means to change these widths towards desired values. Closely related to this question is the test of local dependence of crystal reflectivity on its surface, which may strongly influence the integral reflectivity of a double crystal device if imperfect crystals /12,13,14,15/ are applied.

It is the results of these both groups of tests that determine the reliability and the range of applicability of the double crystal monochromator in question.

Further tests are related to the other components of the device, the thin foil, the collimator, and the detector.

3.1 Tests of mechanical components

The tests of mechanical components all aimed at determining the angular accuracy of the components to find out their influence on the Bragg angle positioning.

The test apparatus for the double crystal monochromator components to check the accuracy of both crystal positioning and the control system consists of a Michelson interferometer with equal lengths of both optical paths. This interferometer is installed on a 1 m by 2 m large and 0.3 m thick granite block. For stable operation the interferometer is housed to reduce air convection, it uses tubes filled with helium to reduce refractive index gradient effects,and its mechanisms are optimally damped.

The interferometer is complemented by a linear displacement table (Jacob) plus motor for the spindle drive, two motors for the rotational motion, two electro-optical incremental transducers (Heidenhain ROD 700) and the corresponding control system (MANIA) as well as a laser.

The test can be performed placing a parallel glassplate into the optical path(s), in order to determine the angular motion of this plate by the measurement of the interferometer fringe shift. Using a thickness of 1.5 cm for the plate of refractive index n = 1.5 or n = 1.71736, respectively, one obtains the angular sensitivity of this interferometric device as function of angle of incidence as indicated in the Fig. 7 for two different laser wavelengths, that of the He-Ne-laser at 6238 Å and that of the Argon-laser at 4880 Å respectively. With the 60 mm glass block the sensitivity is increased by a factor of 4.

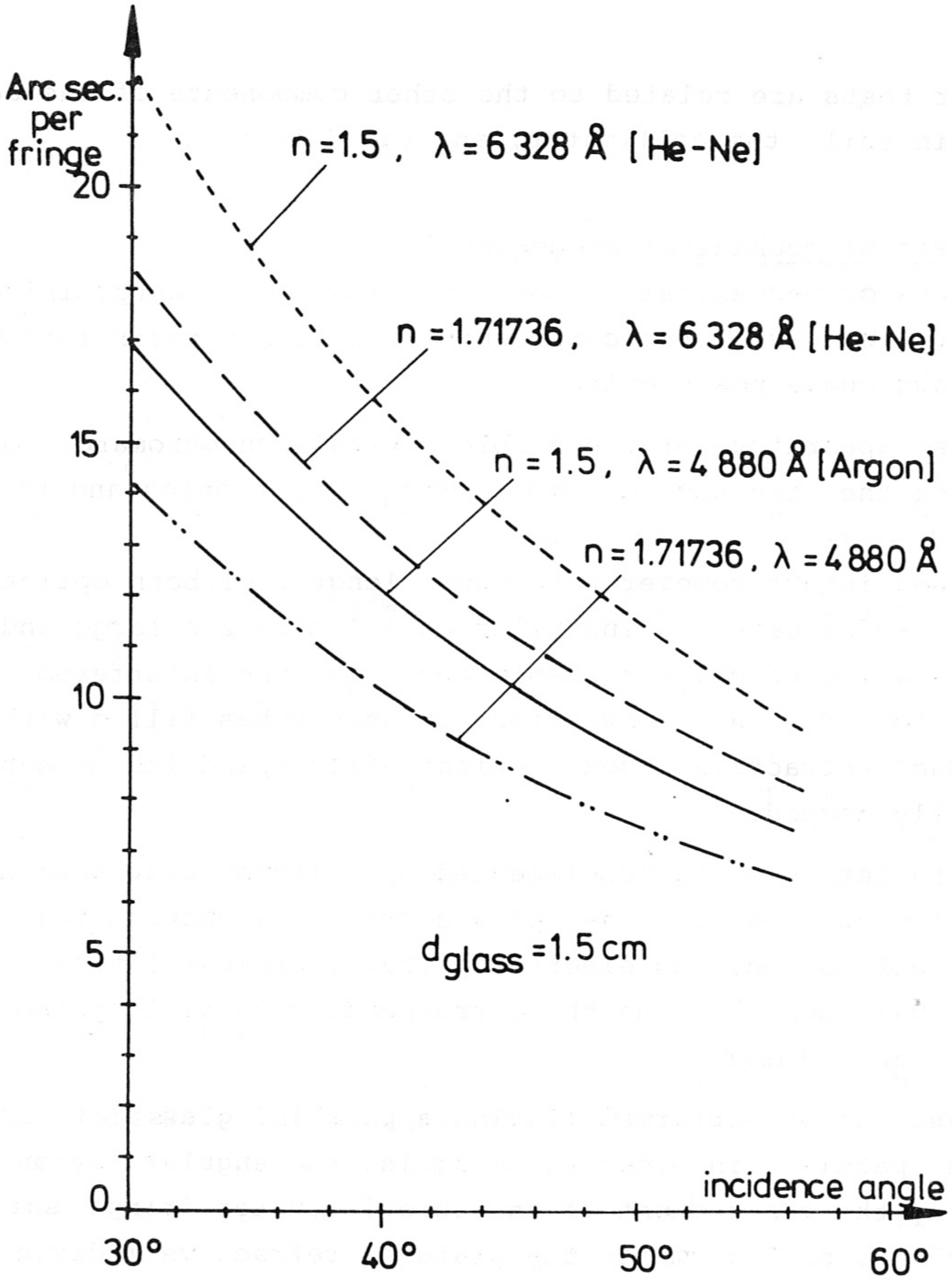

Fig. 7 Angular sensitivity of the interferometer for two different laser wavelengths versus the light incidence angle on 1.5 cm thick glass block

3.1.1 Test of linear displacement table

The linear displacement table (Jacob) plus motor for the spindle drive was tested in quasi-static version and in fast motion using the He-Ne-laser and a glass block as indicated in the upper part of Fig. 8. The lower part of this figure gives the test result. The table shows long-scale excursions in transverse angular direction as well as equidistant short-scale "spikes" related to the sphere entrance into the roller gears. These results of the Michelson interferometer applying the He-Ne-laser were confirmed by direct reflectance measurements (over long distances), which also gave the vertical angular excursions (of about the same magnitude), as well as by autocollimation measurements - as proposed by R. Deslattes /15/.

This presently insufficient accuracy of the Jacob linear displacement table has its origin in the design features of this system, since the accuracy of the linear displacement of this table is limited by the lateral guidance, which is mechanically overdetermined. A further deterioration results from the roller gears, the entering spheres giving rise to the observed (see Fig. 8) small spike-like angular deviations. The design of the linear displacement units proposed for this monochromator will reduce these inaccuracies and promises to get the desired high accuracy. Testing of this device in its final form, however, should be carefully performed.

Fig. 9 gives a photo of the Michelson interferometer on the granite block. The linear displacement table (Jacob) is in the foreground, the motor for the spindle drive at right. The He-Ne-laser is in the background. The two interferometer arms contain the helium filled cylindrical glass tubes. The linear displacement table carries the aluminium tower that contains the crystal rotation unit with the motor for the rotational motion and the electrooptical incremental transducer (Heidenhain ROD 700).

For the tests a MANIA position control system consisting of a central controller and a positioning module has been used. The positioning module handles two motions, either one translational and one rotational motion or two rotational motions. The motion of each axis is controlled by a feedback loop consisting of the motor and a position transducer. During the tests, however, it turned out that the MANIA control system was not reliable enough for remotely controlled operation. Most of the problems were caused by the early development stage of the software delivered, such that for the control system of the spatial scan double crystal monochromator the positioning control system of chapt. 4.3 will be proposed.

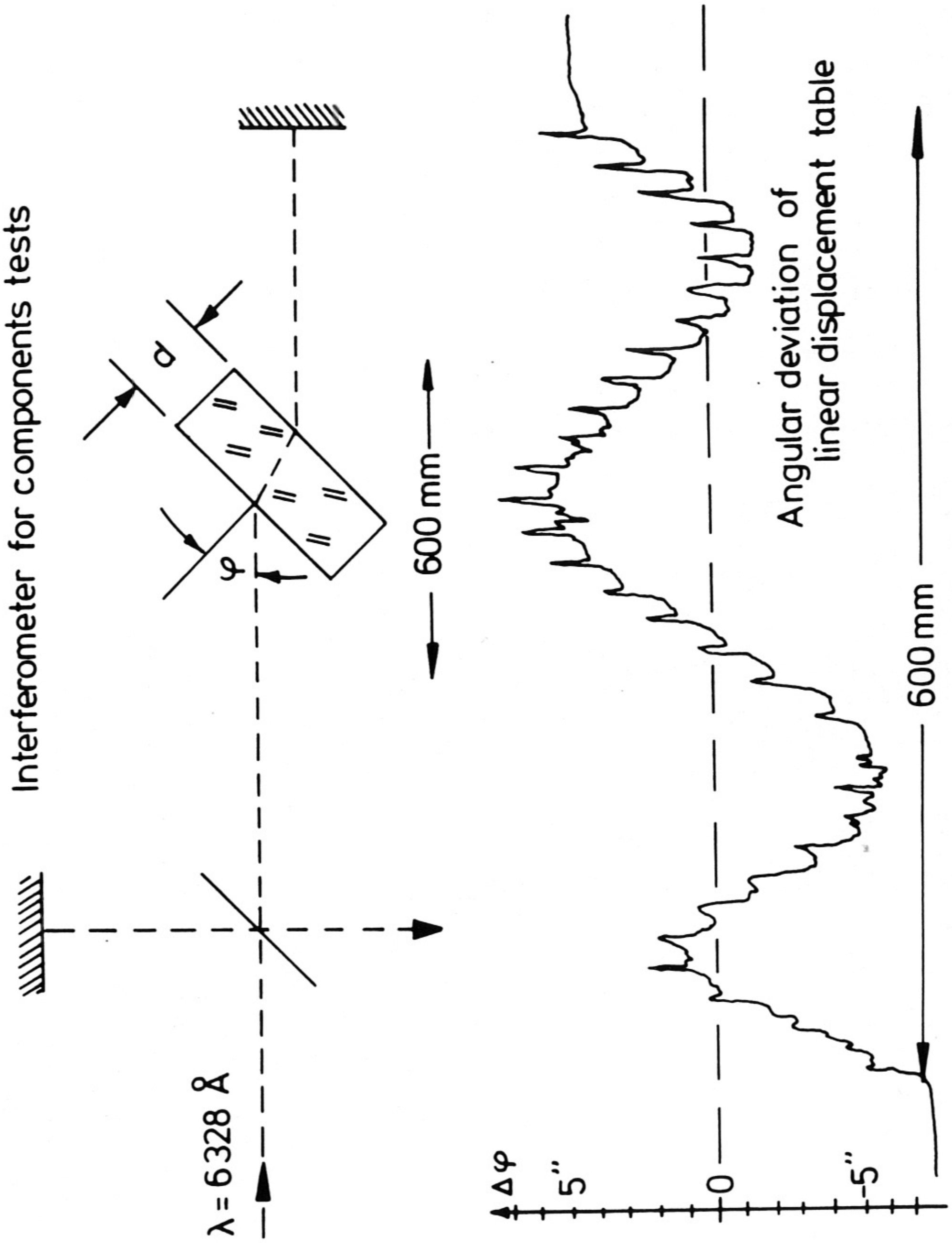

Fig. 8 Scheme of the glass block in the He-Ne-laser operated interferometer for angular deviation measurement of linear displacement table and result of angular excursions of the table during 600 mm longitudinal drive.

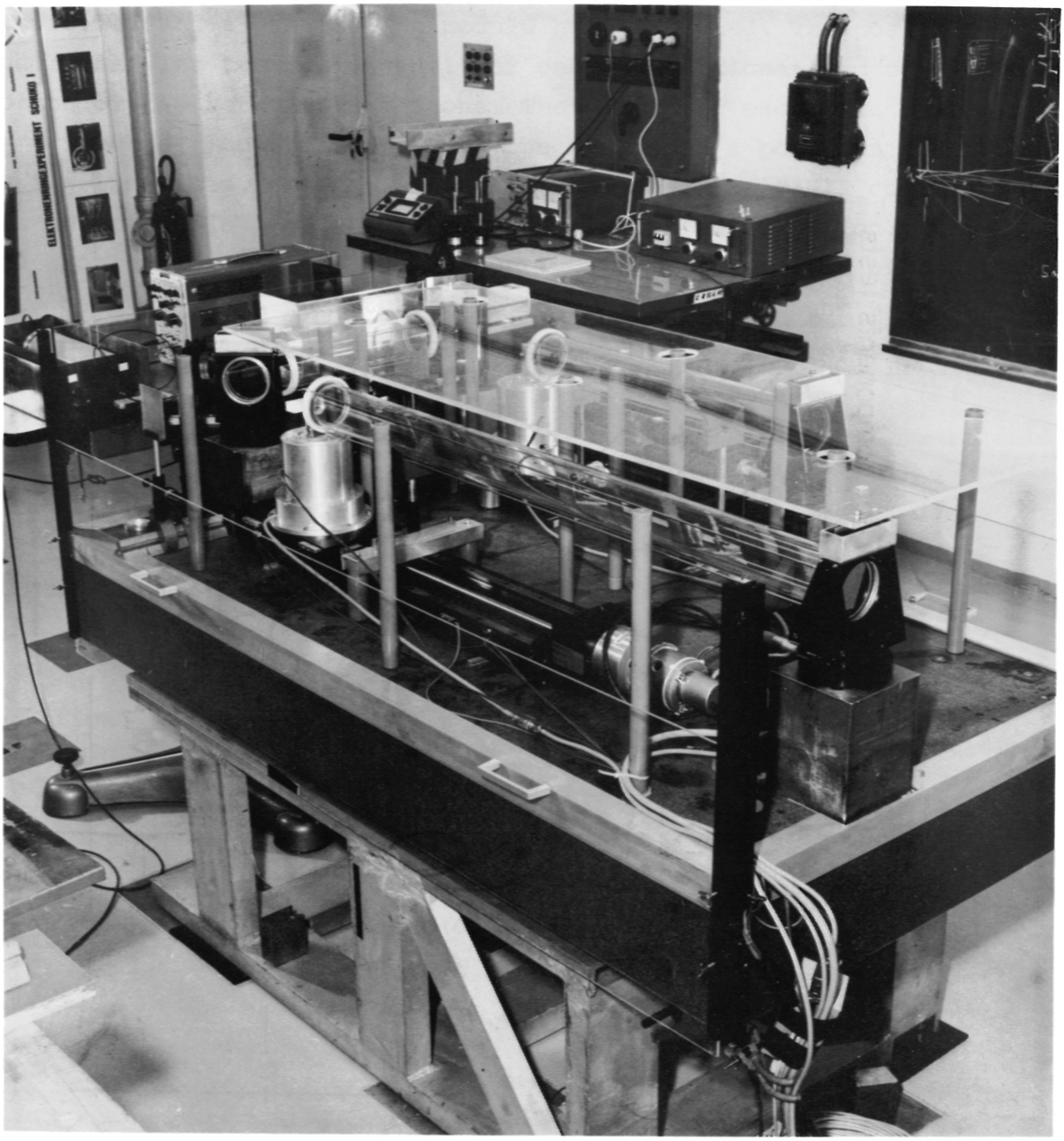

Fig. 9 The Michelson interferometer for tests of the linear displacement table (foreground). The He-Ne-laser is in the background.

3.2 Crystal Tests

The double crystal monochromator configuration built with crystals of relatively small rocking curve widths is very sensitive to crystal lattice imperfections/12,13,14,15,22/. If the deviations of the lattice orientation on the crystal surfaces are larger than the (locally determined) rocking curve widths the integral reflectivity of the double crystal device will substantially go down. Mainly natural crystals show these inhomogeneities /10,15,22/.

Since LiF (220) has a convenient lattice constant (2d = 2.848 Å) for diagnosing the hydrogen- and helium-like transitions of the wall constituent elements in the Bragg angle range from about 23.9° to 45.5° (see Fig. 4 on p. 6), this type of crystal was tested for several different samples.

At first cleaved LiF (220) crystals of 70 x 100 mm^2 surface area and 3 mm thickness, delivered by Quartz and Silice, were investigated using the 30 kW X-ray source of PTB with the $\mathrm{MoK}_{\alpha 1}$ line at a wavelength of about 0.709 Å. The surface of the crystals was scanned in four different strips of 20 mm hight and 1.2 mm width (resulting from 0.3 mm width of the tungsten aperture) along the long side (100 mm) of the crystal. At every local position the angle Θ of maximum reflection was determined and plotted as deviation $\Theta - \bar{\Theta}$ from an average angle $\bar{\Theta}$.

An example of these measurements is plotted in Fig. 10. The maximum reflection angle deviation varies by up to about 100 arc seconds, which is much more than the (local) rocking curve width, which is indicated as the error bar. The variation, however, is of long-scale character; there seem to exist areas of dimensions in the cm-range which are of high crystal quality.

In order to find out the reason for the strong variations, which might originate from $\Delta d/d$ effects or from tilting of the lattice elements, the crystal was reversed by 180°, and the same strip was measured (now with the complementary angle). As is obvious from Fig. 10

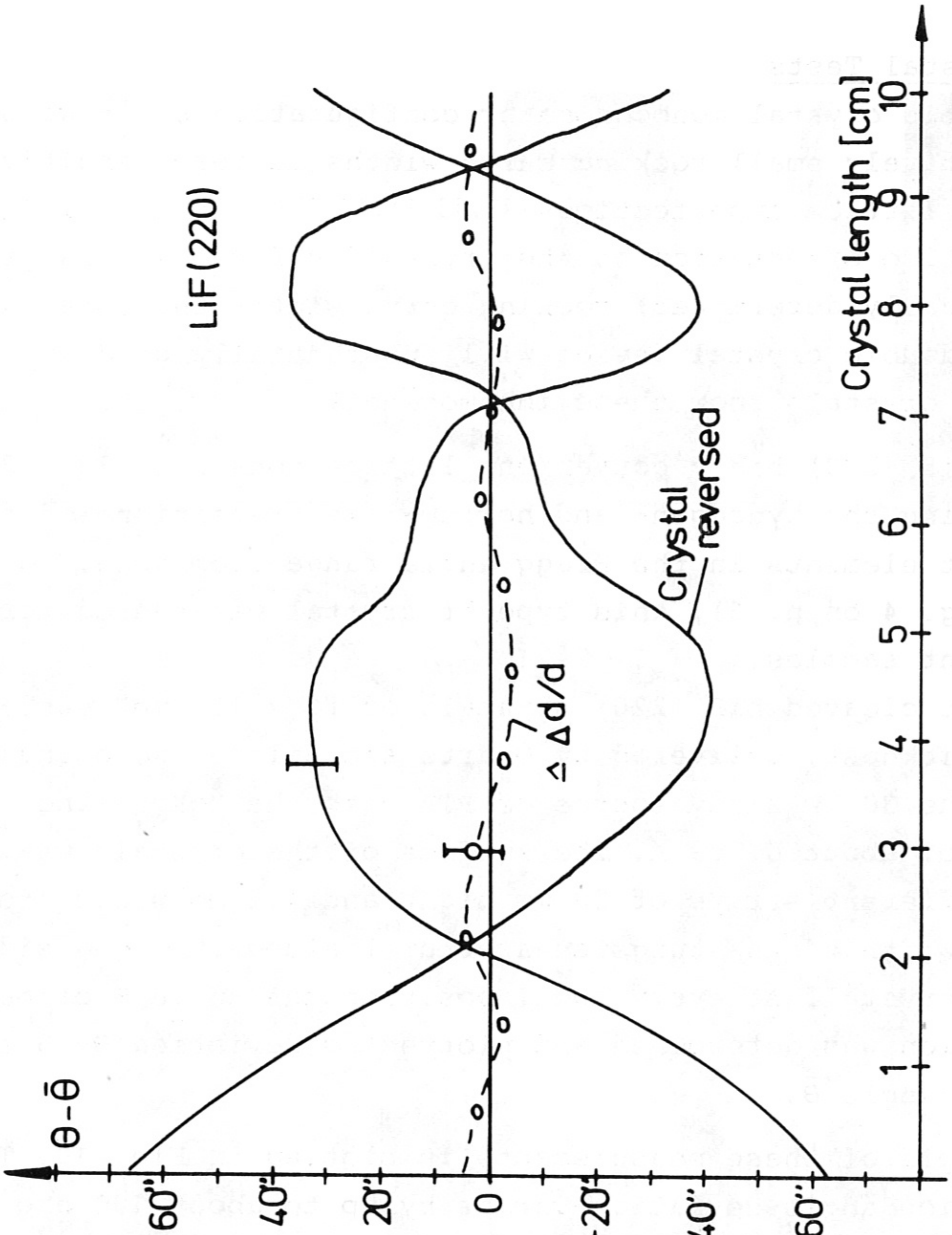

Fig. 10 Position of maximum reflection angle versus location on the crystal surface of LiF (220) together with that of reversed crystal

the maximum reflection angle deviation from the mean value $\bar{\Theta}$ represents nearly the original curve just reflected at the abscissa. Hence if taking half of the sum of both curves the $\Delta d/d$-effect appears. It is smaller than 4" over the total length of the investigated strip.

From this result one can conclude, that tilting of the lattice elements, not the $\Delta d/d$-effect is the origin for the maximum reflection angle variations along the crystal surface. The amount of a possible contribution of the lattice constant variation $\Delta d/d$ to the observed maximum reflection angle variation given by

$$|\Delta d/d| \leq |\Delta\Theta/\tan\Theta| < 7.5\cdot 10^{-5}$$

is by more than one order of magnitude smaller than the tilting angle variation

$$|\Delta\Theta/\Theta| \simeq 1.2\cdot 10^{-3}$$

observed at $\Theta = 14.42^{\circ}$.

Pairing of LiF (220) crystals of these properties does not seem feasible for a double crystal monochromator.

As a consequence of this result abraded LiF (220) crystals were investigated. These crystals (delivered and surface-treated by Quartz and Silice) were abraded according to the process developed at Saclay /11,21,10/. Their properties turned out to be very much more suitable for the use in the designed double crystal monochromator.

For these abraded LiF (220) crystals the double crystal device as sketched in the upper part of Fig. 11 could be applied, because of the much higher integral reflectivity of the abraded crystals. The spatial dependence (on the crystal surface) of both successive reflections was accomplished by moving a 2 kW X-ray source with its MoK_{α} line radiating) and the NaJ (Tl) detector (with 1.25 mmx30 mm

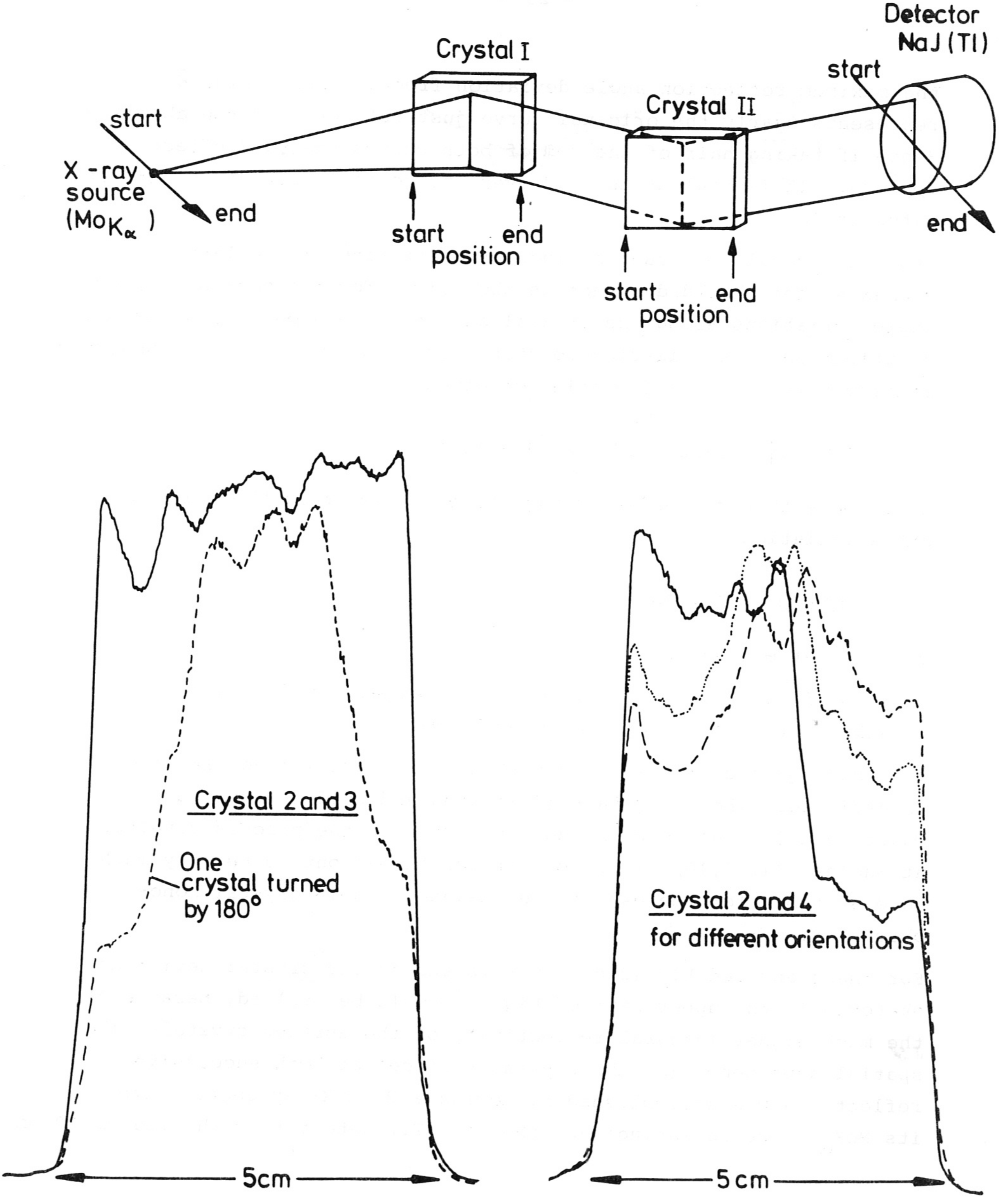

Fig. 11 Test of double crystal local reflectivity of abraded LiF (220) crystals with the arrangement sketched in the upper part. The scanning along the 5 cm long side of the crystal shows nearly spatially constant (high) reflectivity (solid line in left lower plot) for certain crystal combinations, while turning one of the crystals (dotted plot in left lower part) or other combinations (right lower part of figure) result in lower and spatially dependent reflectivity.

aperture) simultaneously. Hence the crystals (of 30 x 50 mm^2 area and 3 mm thickness) were scanned along their 50 mm dimension. As can be seen in the lower part of Fig. 11 there exist combinations of two of the four tested crystals that show a (local) integral reflectivity, which does not vary much over the crystal length. If, however, one of these crystals is turned by 180° (see left plot in lower part of Fig. 11) the reflectivity is worse and shows pronounced spatial dependence. For other combinations optimization by changes of relative orientation was tried without success, as is obvious from the right plot in the lower part of Fig. 11.

Among the four crystals being tested with its six combinations and six reversals three crystal combinations showed very good reflectance behaviour, the reflectivity varying by less than 10% along the total crystal length. The results were reproducible after crystal replacement and reorientation.

The double crystal rocking curve as determined with the 1.25 mm beam is plotted in Fig. 12. Its width is relatively large (with 2'40"), and it is interesting to note that the rocking curve width of the rear side of the crystals (which looks polished in contrast to the abraded top side) is nearly as large (2'6"), which might result from depth effects of the abrading procedure.

Although these results nicely fulfill the requirements imposed by the finite mechanical accuracy of the double crystal monochromator design, the rocking curve width found here might be too wide for line separation (and certainly for line profile) measurements. However, there will certainly be means of adjusting the rocking curve width just in between at prescribed values by applying less effective abrading or by using artificial LiF crystals as will be done in the future.

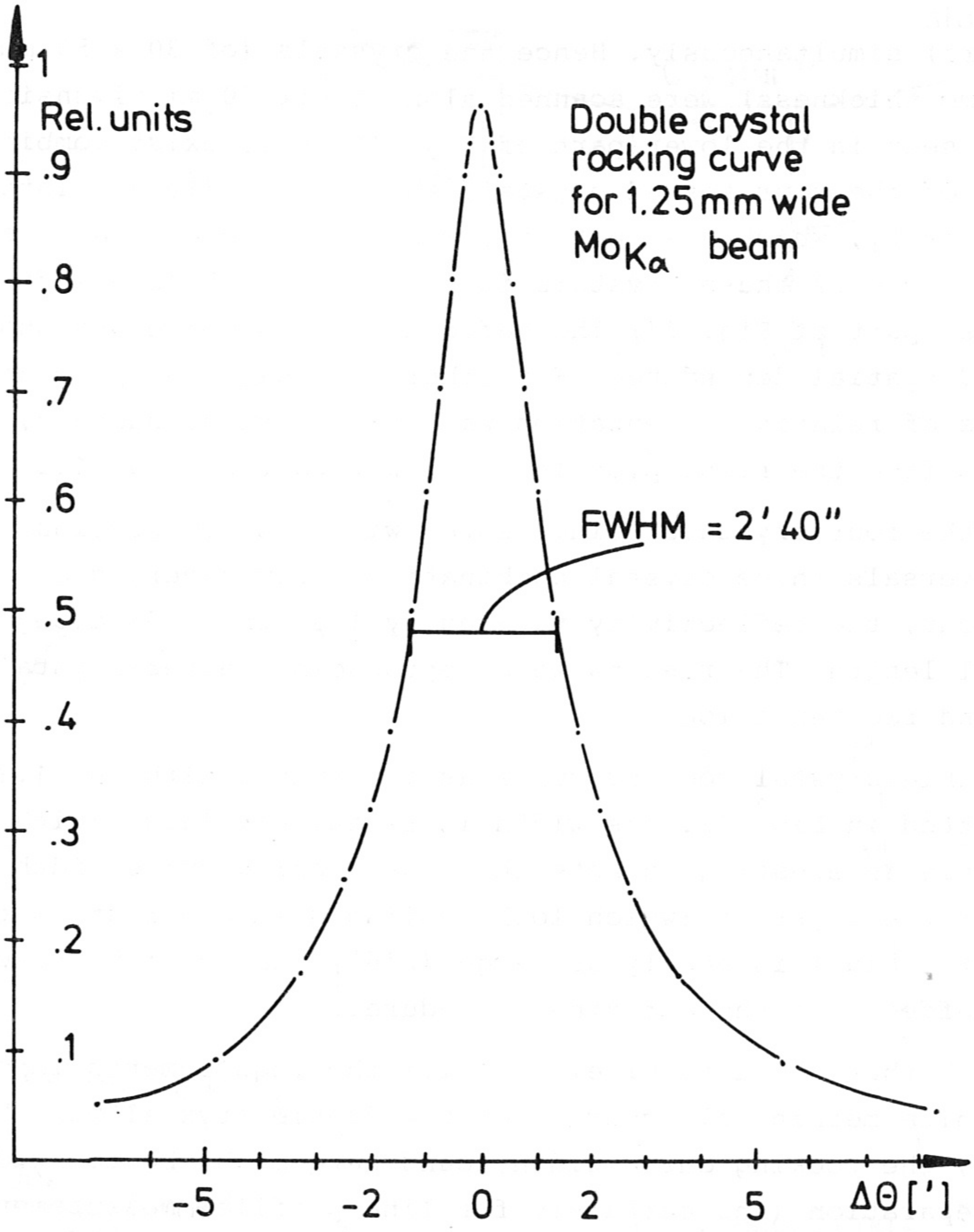

Fig. 12 Double crystal rocking curve (locally determined) for abraded LiF (220) crystals at MoK_{α} .

3.3 Test of thin foils

For the separation of the JET torus from the spectrometer with its less qualified vacuum conditions (because of movable elements) a thin window is to be placed at the end of the beam line from the torus to the active phase double crystal monochromator, at the entrance of the first module. Eight different thin window materials have been considered and tested with respect to the many conditions they should meet: Relatively high transmission for photons, also for those slightly above 20 Å (e.g. the hydrogen- and helium-like oxygen lines), mechanical reliability under combined action of atmospheric pressure difference and high temperatures (up to about 150° C), as well as low permeability for air and - if possible - for tritium.

The transmission of some typical foils of different thickness considered is plotted in Fig. 13 versus the wavelength.

The results of the testing indicated the foil HOSTAPHAN RE2 of 2 µm thickness being a reliable candidate for the thin window, although the transmission is only T = 0.044 at 21.6 Å and T = 0.1 at 19 Å.

This foil, however, is mechanically stable for pressure differences of more than 2.5 bar, if being supported by a mesh of 1.5 mm distance or less, even if being heated up to 180° C. It stays mechanically intact unless it is not stretched in area by more than a factor of two, then monotonically increasingly becoming porous.

Leakage measurements were performed according to the "accumulation testing" /23/: At atmospheric pressure difference the leak rate of an effective area of more than 2.5 cm^2 was

$$Q = V\, dp/dt = 30\ \mathrm{l} \cdot 10^{-3}\ \mathrm{mbar} / 60\ \mathrm{s} = 5 \cdot 10^{-4}\ \mathrm{mbar\ l/s},$$

which for an area of about 75 cm^2 and a pressure difference of 10^{-6} mbar will result in a leak rate of less than

$$Q = 1.5 \cdot 10^{-8}\ \mathrm{mbar\ l/s}.$$

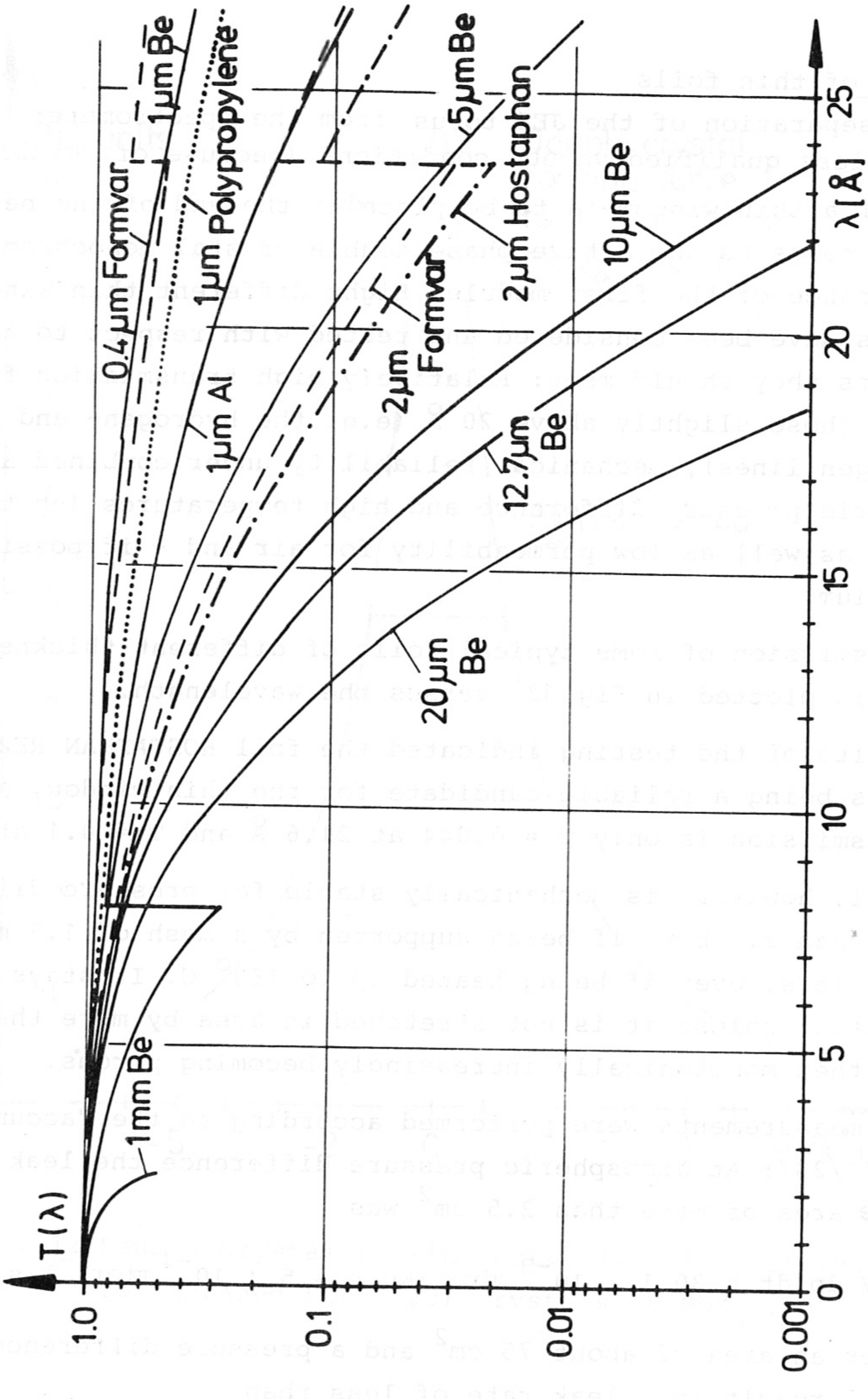

Fig. 13 The transmission of some typical thin foils with different thickness versus wavelength

This still unsatisfactorily high leak rate can certainly be reduced by a more appropriate supporting mesh and/or by covering the foil by a layer of a few 1000 Å of aluminium, which just can be afforded from soft X-ray transmission arguments.

Long-duration tests were performed under combined action of pressure difference of up to 1 bar and heat on these 2 μm thick HOSTAPHAN RE2 foils of about 5 cm Ø size supported by a frame of 1.5 mm Ø holes over a time interval of about 80 days. The number of total pressure load cycles was 300.

The result is sketched in Fig.14 . Although the foils were mechanically stressed very often by the frequent pressure changes during and after heating periods, they survived for long times of about 40 days before getting small holes leading to increased leak rate.

It is obvious that the survival of these foils even at higher temperatures will be very much longer if - as is intended - the pressure difference between both sides of the foils is kept much below atmospheric pressure difference.

Measurements of the evaporation rate of the thin window foil HOSTAPHAN RE2 were performed with a foil of 300 cm^2 area. The vacuum system was baked in preliminary measurements at 130° C with and without the foil, resulting in a final pressure of $p < 4 \cdot 10^{-9}$ mbar, both with and without foil, so that the pressure difference is assumed to be less than $2 \cdot 10^{-10}$ mbar. For the assumption of this difference being due to H_2 evaporating from the foil and the nominal pumping speed of the turbopump of 100 l/s as well as the tube conductivity, the evaporation rate of a 75 cm^2 foil area would be less than

$$Q \lesssim 5 \cdot 10^{-9} \text{ mbar} \cdot \text{l/s}.$$

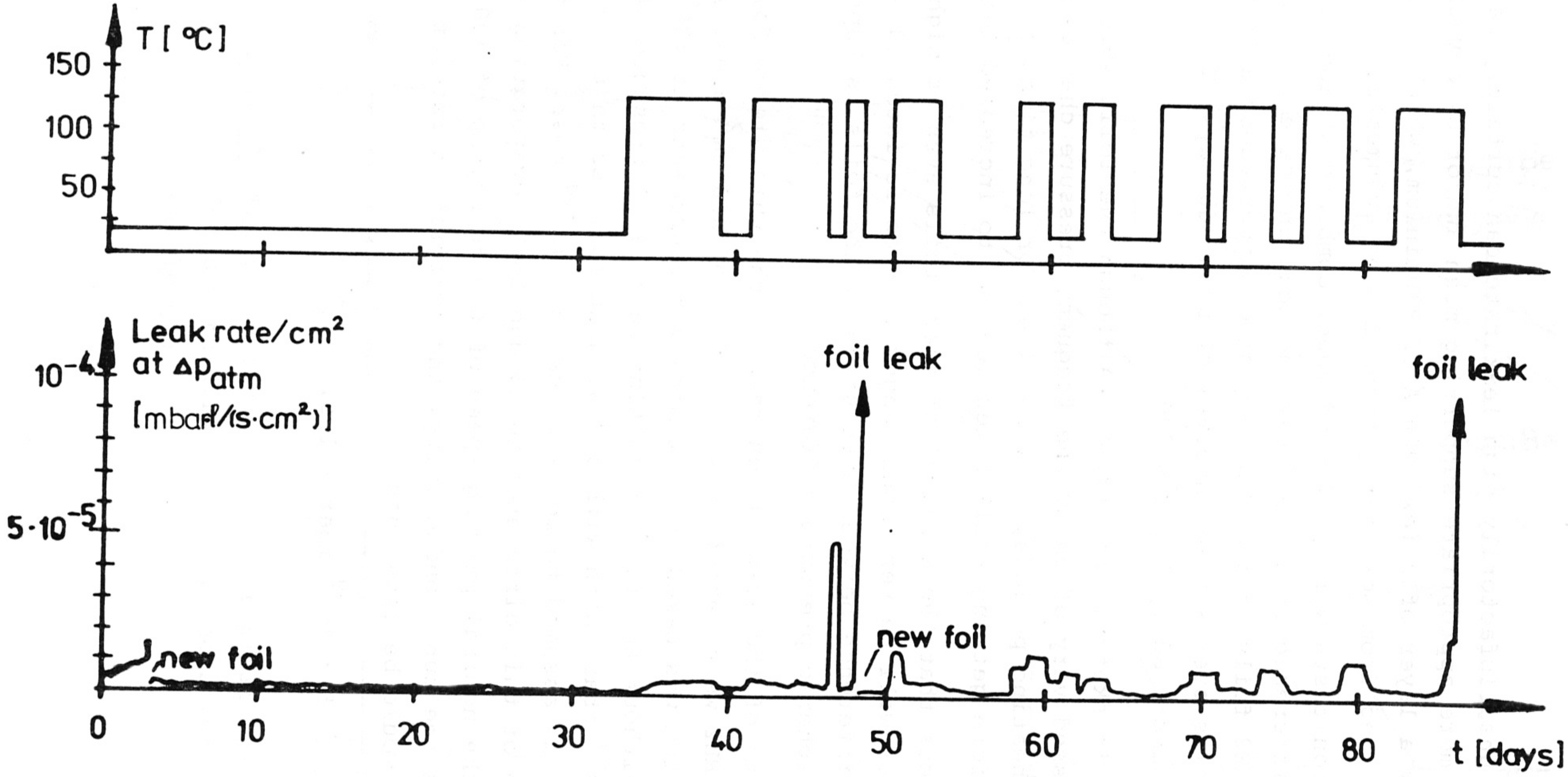

Fig. 14 Long duration tests of 2 µm thick HOSTAPHAN RE2 foils under combined action of heat and atmospheric pressure difference

The HOSTAPHAN RE2 foils hence seem to be reliable, although their transmission above 20 Å is relatively low.

Alternatives to the HOSTAPHAN RE2 foil might be the 0.4 µm Formvar-window, which - supported by a mesh - can only be applied at temperatures below 70° C, having high transmission values (0.56 at 21.6 Å and 0.64 at 19 Å), the thin alumina (Al_2O_3) - windows, to be made according to U. Hauser and W. Kerler /24/ and H. Johnson and R. Deslattes /25/ which seem to be tritium barriers /15/, the thin (0.5 µm) Kapton foil, to be made according to /26/, the Carbon-covered Polyprophylen foil (1.0 µm) according to /27/ or the Parylene (C_8H_8) foil (1.0 µm), covered with Al according to /4, 28/.

3.4 Detector and collimator tests

The double crystal monochromator in non-dispersive (parallel) mode has the advantage of fixed detector position during wavelength scanning. Since only plane crystals will be applied the sensitive area of the detectors must be large, slightly larger than the effective crystal area (70 x 86 mm^2). No spatial resolution is necessary. However, in order to obtain high count rates, which are expected from the JET plasma radiation /3/, multi-wire proportional counter geometry is proposed. It is expected that a counting rate of the order of more than 10^5/s per wire can be obtained, as demonstrated by Charpak et al. /29/.

On the basis of the fundamental properties of multiwire proportional counters /30/, of special developments /31,32/ and mainly on the technological developments of E. Pfeffermann at MPI für Extraterrestrische Physik /27/ a test detector device was built. The device is shown in Fig. 15 . It consists of a relatively large vessel, which avoids background pulse contribution from photo-electron emission at nearby metallic walls. The gas flowing through the vessel can be changed with respect to pressure (from several tens of mbar to more than an atmosphere and gas type (argon with Methane, Xenon,...) /30/, in order to match the optimum counting parameters for the chosen wavelength and counting rate range. The multiwire units consist of a frame oriented in the desired position by spacers. They carry about 80 wires of 10 µm diameter for the anode plane, while the cathode wires are made of 20 µm diameter. The vessel is covered by a 2 µm HOSTAPHAN RE2 foil on a thin tungsten mesh supporting grid which again is supported by a slot type structure, which can be seen in the top flange (right) of Fig. 15.

The tests have just started; results are not yet available. As described in the block diagram of the electronic systems the anode wires will be divided into eight groups of 10 wires each.

The detector electronics is shown in Fig.37 in chap. 4.5. In order to avoid ground loops the detector will be galvanically decoupled

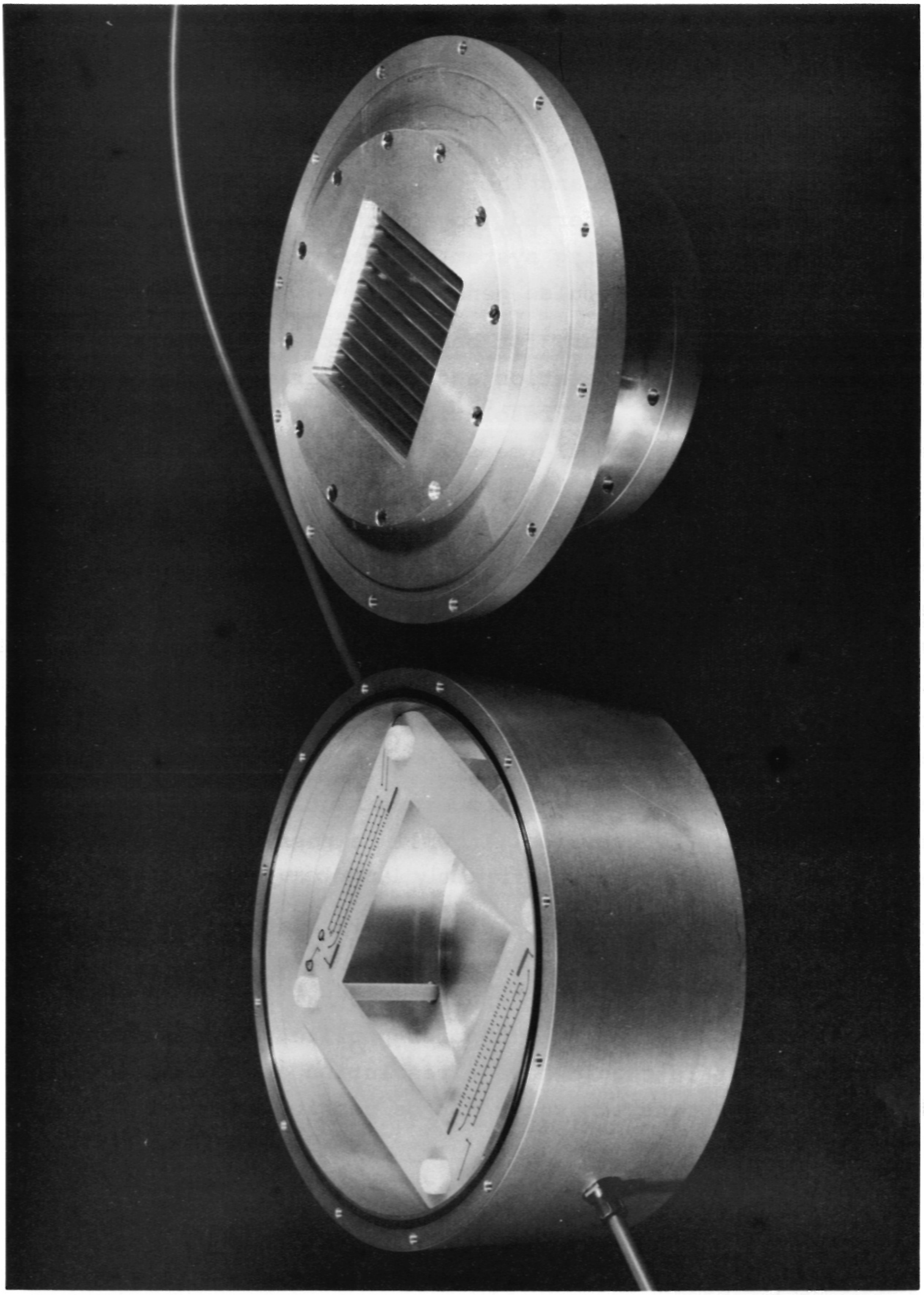

Fig. 15 Multiwire proportional counter test device

from the experiment. The detector wires are connected in 8 groups of 10 wires, each group having a separate preamplifier, mounted close to the detector. Each amplifier chain contains a pulse shaping main amplifier and a window discriminator. The output pulses of the 8 channels are summed up and then counted by a latching scaler. The scaler contents is transferred (together with real-position information from the positioning system) to a memory at load pulses generated by a programmable pulse generator.

The collimator is necessary for beam acceptance limitation for enabling spectral line separation and the separation of the spectral lines from satellites, the resolution being in the order of 600, or - for the case of line profile measurements for ion temperature evaluation by Doppler profile - in the order of 5000.

For the coarse collimator a model Soller collimator made of 49 lamellae of Cu-Be alloy of 0.1 mm thickness was tested. The transmission was measured as function of the angular position $\Delta\varphi$, as plotted in Fig.16. using the $Cu_{K\alpha}$ radiation of the X-ray calibration source. The FWHM of the angular acceptance is roughly equal to the width as expected from the geometrical dimensions. Also the transmission was found to be in the order of the expected value.

This model collimator had smaller cross section than desired for the monochromator in question. It will be possible to reach the necessary resolution with a sufficiently large beam cross section as well.

For the spatial scan double crystal monochromator in question the spectral resolution of about 400 is sufficient to separate triplett- and singulett helium-like Ni- and Fe-spectral lines. It is just low enough not to narrow the full Doppler profile. However, for this application the crystals should have a resolution of $\lambda/\Delta\lambda \gtrsim 400$, because otherwise line separation would not be possible.

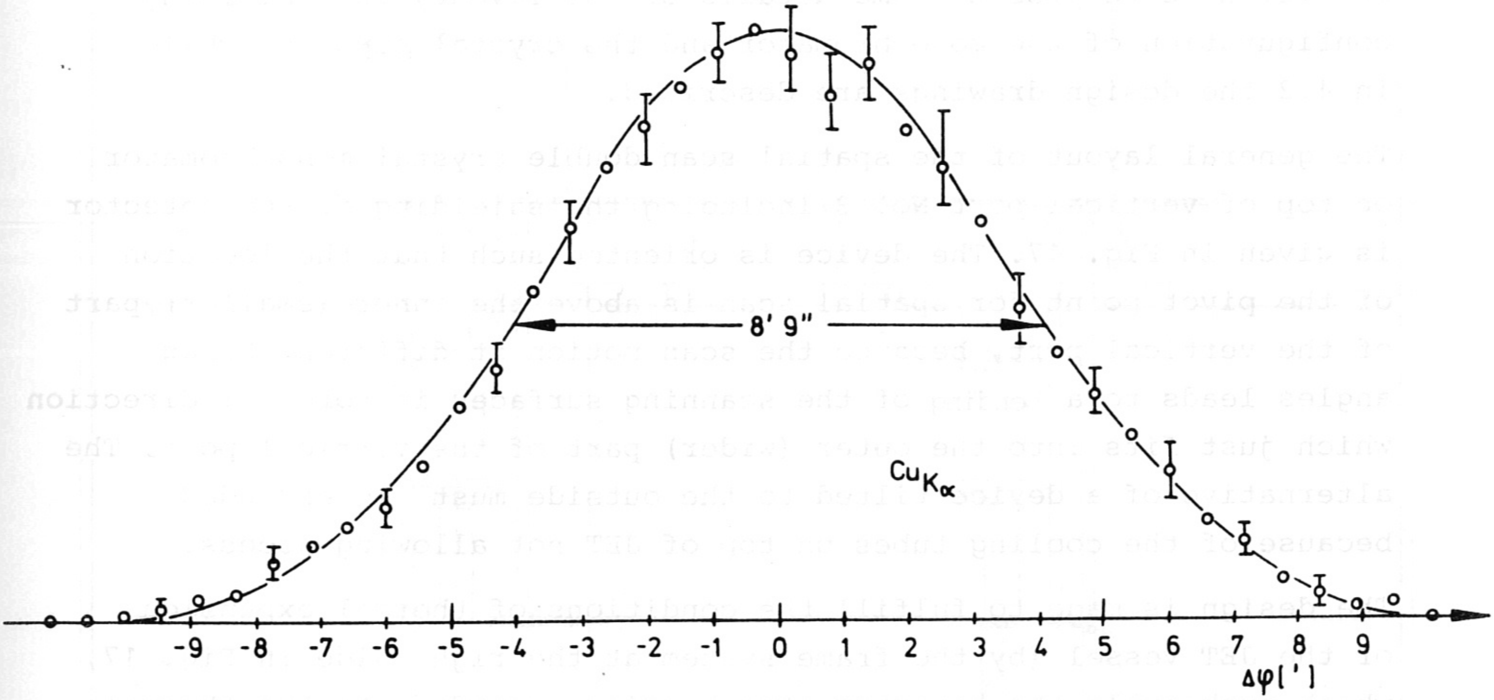

<u>Fig. 16</u> Transmission of Soller collimator versus angle

4. Engineering Design

4.1 General design and shielding

4.1.1 Monochromator layout

The general spatial scan monochromator configuration was described in 2.2. Here we present some details of the layout, the shielding configuration of the monochromator and the crystal support, while in 4.2 the design drawings are described.

The general layout of the spatial scan double crystal monochromator on top of vertical port No. 3 including the shielding of the detector is given in Fig. 17. The device is oriented such that the location of the pivot point for spatial scan is above the inner (smaller) part of the vertical port, because the scan motion at different Bragg angles leads to a bending of the scanning surfaces in toroidal direction which just fits into the outer (wider) part of the vertical port. The alternative of a device tilted to the outside must be excluded because of the cooling tubes on top of JET not allowing access.

The design is made to fulfill the conditions of thermal expansion of the JET vessel (by the frame system at the right side in Fig. 17, which push-pulls the monochromator housing according to the thermal expansion of the vessel)and of sustaining major disruptions by decoupling the monochromator housing from the vertical port via a bellow . The design takes into account that the monochromator vessel and the VAT valve keep away from the water manifolds of the vertical field coil P2 by nearly 50 mm. Moreover, the device can be dismantled by remote handling after possible activation. However, in case of removal of the activated equipment using the RH screwer the monochromator vacuum vessel has to be lifted up by 25 mm in order to give free access for the RH screwer, to open the screws. The vessel can then be lowered down to the original position, to allow the screws to be taken out by means of the nut runner.

The monochromator vessel (because of the decoupling from the vertical port) is supported by pendulum rods hanging on a support structure

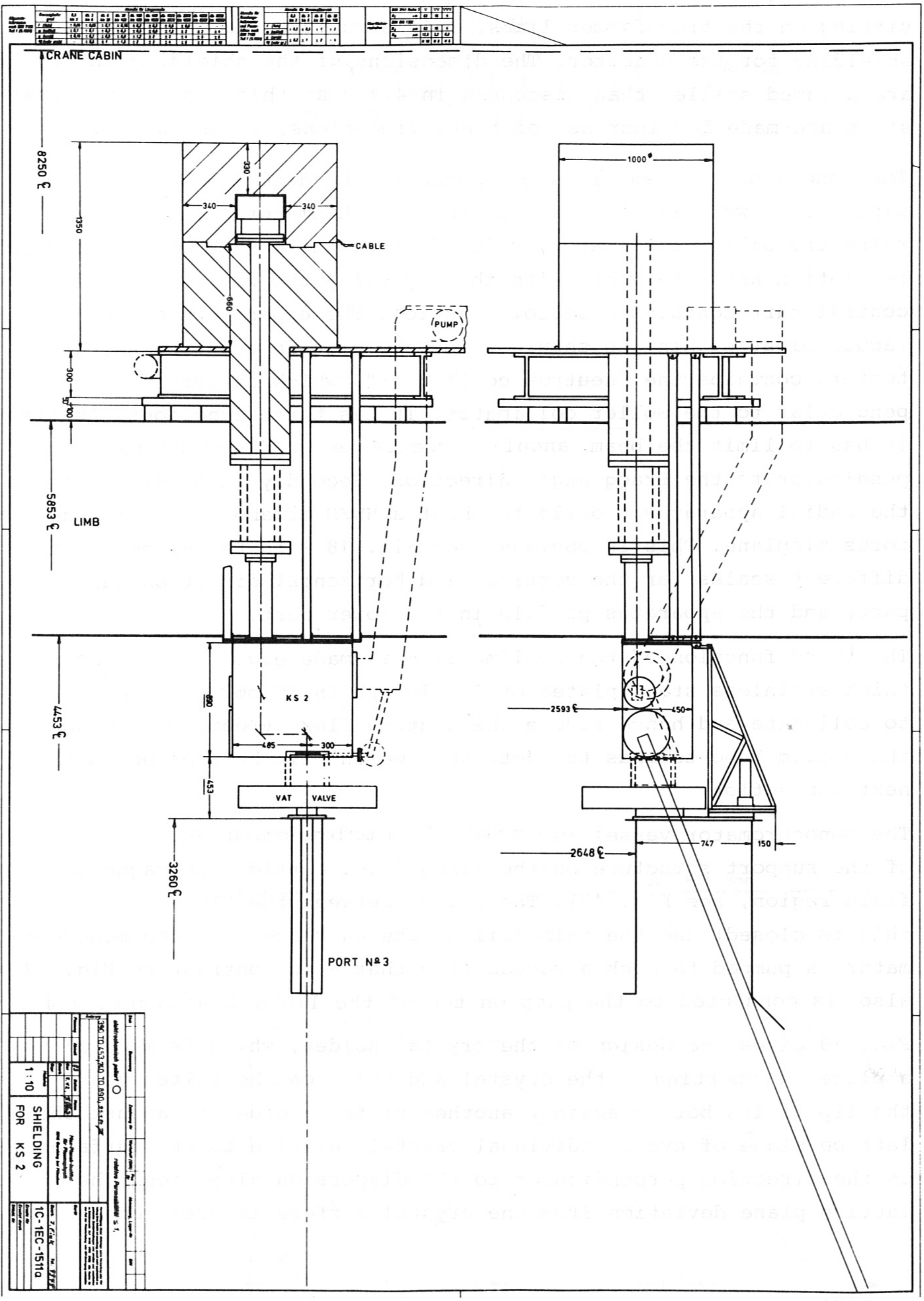

Fig. 17 Layout of the spatial scan double crystal monochromator on top of vertical port No. 3 including detector shielding.

sitting on the transformer limbs. This structure also carries the shielding for the detector. The dimensions of the shielding in Fig. 17 are assumed smaller than discussed in 4.1.2 at this stage, but provisions are made for increase of these dimensions, if necessary.

The monochromator vessel is connected to the detector by a vacuum pipe. Its lower part is fixed to the monochromator because it contains the Soller collimator, which defines the monochromator spectral resolution and - together with the crystal - the wavelength. The central part contains a bellows section. The upper part of the vacuum pipe, within the shielding block, just in front of the detector, contains the "neutron collimator", which is oriented perpendicular to the Soller collimator. It has three functions: At first it has to limit the beam angular acceptance in the direction perpendicular to the Bragg angle direction. Secondly it should limit the radial apparatus profile to about a HWFM of about 7 cm in the torus midplane. This is obvious from Fig. 18 with the geometry in different scales for the vertical and horizontal direction (upper part) and the apparatus profile in the lower part.

The third function of the collimator - if made e.g. of 1.5 mm thick stainless steel plates of 1 m length in 10 mm distance - is to collimate and hence reduce the neutron flux streaming through the vacuum tube towards the detector, which will be treated in the next subsection.

The monochromator vessel is evacuated by a turbomolecular pump on top of the support structure on the limbs (i.e. outside the magnetic field region, see Fig. 17). The volume between the VAT valve (if this is closed) and the thin foil at the entrance into the monochromator is pumped through a vacuum line that - in contrast to Fig. 17 - also is connected to the pump on top of the limbs (see chapt. 4.4).

Fig. 19 gives the design of the crystal holder, which is made of a plate supporting the crystal and which can be tilted via the lip at its bottom against another plate in order to adjust the lattice plane of every individual crystal relative to its surface in the direction perpendicular to the dispersion direction. The lattice plane deviation from the crystal surface in Bragg angle

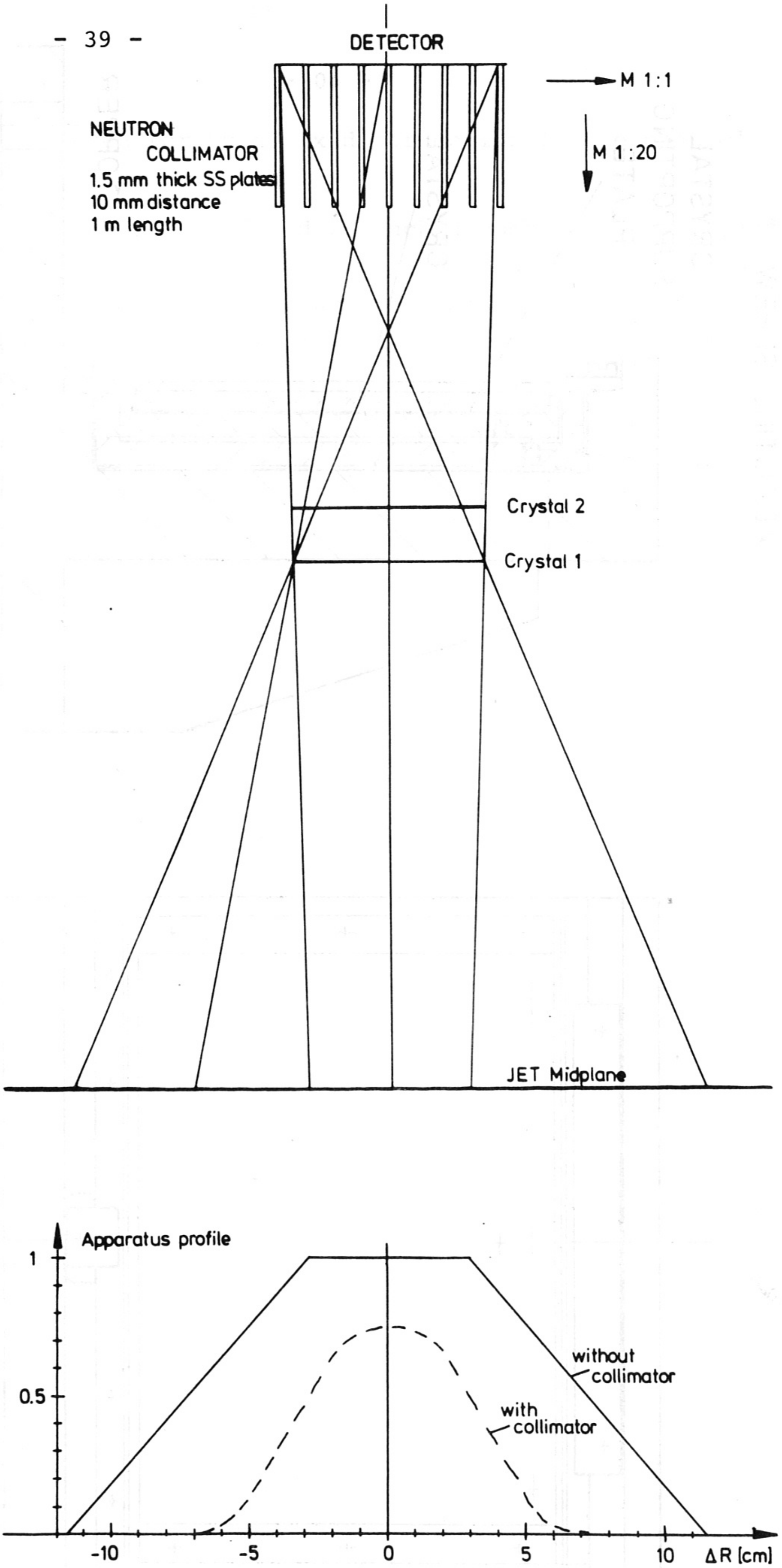

Fig. 18 Neutron collimator geometry (top) and apparatus profile (bottom) for the spatial scan double crystal monochromator

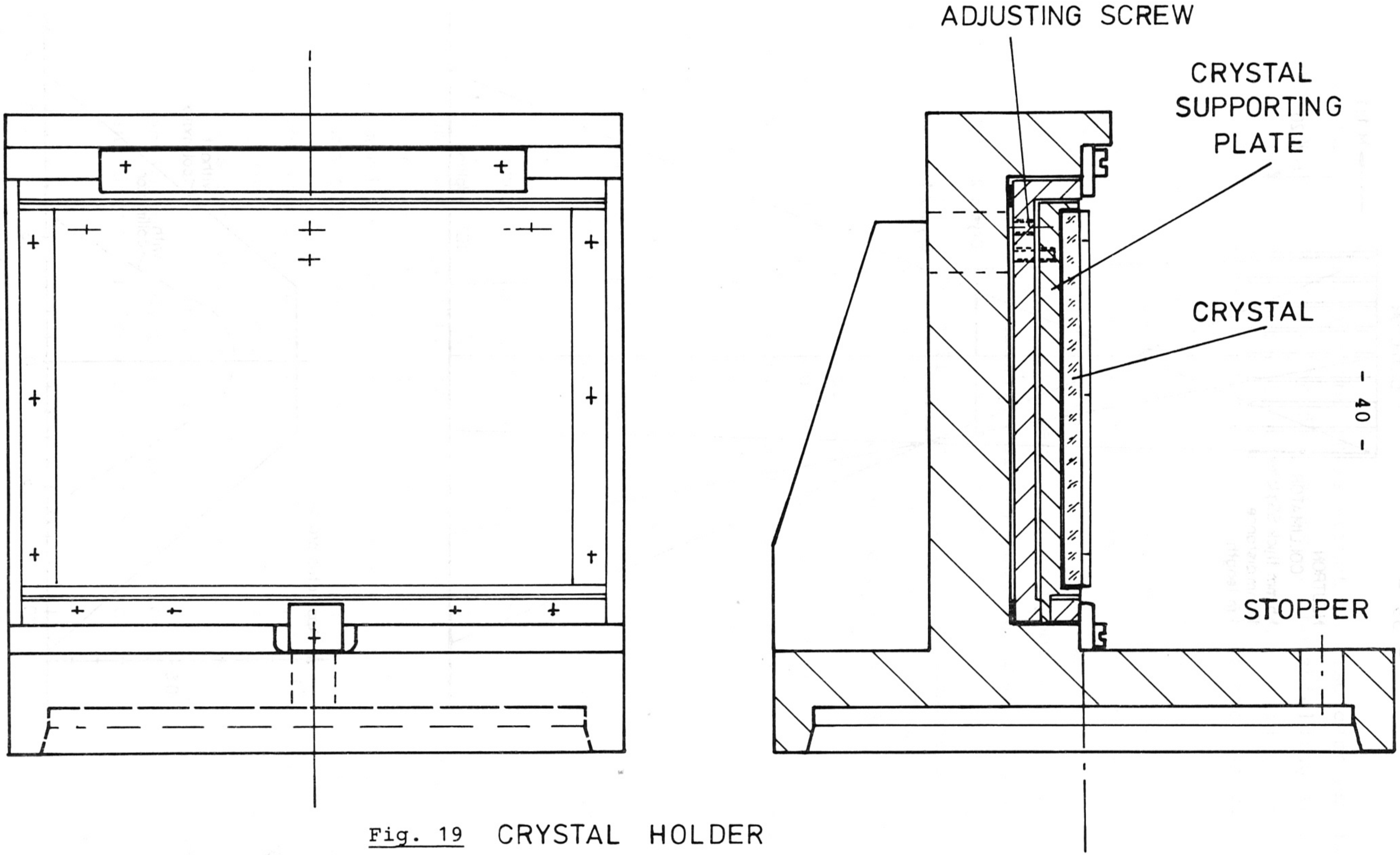

Fig. 19 CRYSTAL HOLDER
M 1:1

direction is accounted for by a fixed correction in the control system.

Every individual crystal is fixed to such a combined support and adjustment unit, which can be attached at well defined position on the crystal rotation tables. Hence changes of crystals should be easy and reproducible. These crystal supports, however, are not yet tested.

4.1.2 Shielding outlay for the JET spatial scan double crystal monochromator

In the spatial scan Bragg spectrometer for JET (KS2) a proportional detector will be used to count soft X-ray photons. On the assumption that the detector will have 80 counting wires, each one being able to tolerate 10^4 counts/s of background counts at a detection probability of 10 % for neutrons and gamma quanta of all energies, the neutron plus gamma flux at the detector (56 cm² sensitive area) must not exceed $\sim 2.5 \times 10^5$ $(n + \gamma)/(cm^2 \cdot s)$.

It is intended to use the spectrometer up to its full specification in a radiation field that results from JET deuterium discharges with a 2.5 MeV neutron source strength of 1.4×10^{16} n/s. At present deuterium discharges with a neutron production rate up to about 7×10^{16} n/s are predicted.

For the outlay of the shielding, that has to attenuate the radiation field by about 4 orders-of-magnitude, the permissible flux of $\sim 2.5 \times 10^5$ $(n + \gamma)/(cm^2 \cdot s)$ at the detector is divided into two roughly equal parts, $\sim 1 \times 10^5$ $(n + \gamma)/(cm^2 \cdot s)$ will pass through the layers of the shielding and an additional $\sim 1 \times 10^5$ $(n + \gamma)/(cm^2 \cdot s)$ will penetrate from the JET port along the open optical (i.e. soft X-ray) path to the detector.

Unshielded fluxes at the detector

A.F.Avery /36/ gives dose rates for deuterium operation of JET "At the vertical viewing port" and "At the roof above the machine". These data scaled to 1.4×10^{16} n/s source strength and converted into neutron and gamma fluxes using suitable choosen flux-to-dose conversion factors* form the basis for the estimates of the unshielded fluxes at the detector position 4 m above one vertical viewing port.

Avery's data "At the vertical viewing port" multiplied with the neutron-open area of the port yields the neutron and gamma quanta currents leaving the port. Port geometry then defines the

---

* For neutrons: 1 rem/s $\hat{=}$ 6.21×10^7 $n/(cm^2 \cdot s)$
for gamma quanta: 1 rem/s $\hat{=}$ 2.05×10^9 $\gamma/(cm^2 \cdot s)$.

opening of the cone into which the radiation penetrates upwards. Distributing the currents over the cross section area of the cone 4 m above the port then results in the following unshielded fluxes originating from the port

$$\phi_n = 1.00 \times 10^9 \ n/(cm^2 \cdot s)$$
$$\phi_\gamma = 2.3 \times 10^8 \ \gamma/(cm^2 \cdot s).$$

Laterally the unshielded detector is irradiated by a flux that can be estimated from Avery's data "At the roof above the machine". The neutron flux at the roof will be about 1/2 multiple scattered neutrons, the other halfe will come directly from the torus. Application of the $1/r^2$-rule for the latter halfe, keeping the former independent of r then gives a flux typical for the outer sides of the proposed shielding of

$$\phi_n = 1.5 \times 10^8 \ n/(cm^2 \cdot s)$$
$$\phi_\gamma = 2.5 \times 10^8 \ \gamma/(cm^2 \cdot s).$$

In the case of the gamma flux the $1/r^2$-rule was applied to the full flux at the roof.

Similarly the flux at the top of the proposed shielding is estimated as

$$\phi_n = 4 \times 10^7 \ n/(cm^2 \cdot s)$$
$$\phi_\gamma = 4 \times 10^7 \ \gamma/(cm^2 \cdot s).$$

The radiation transport model

Radiation transport calculations were performed with the ANISN /37/ discrete ordinates code using DLC-37D /38/ transport cross sections in 100 n + 21 γ group structure. The 1d model consists of concentric spheres with an innermost empty space (40 cm diam.) inside which the resulting fluxes are determined. The isotropically radiating source was just outside the outermost material layer.

Zone	Material	Radius
1	Vacuum	0 cm - 20 cm
2	Lead	20 cm - 50 cm
3	H_2O with B	50 cm - 140 cm
4	Vacuum	140 cm - 142 cm
	Source	141 cm - 142 cm

Table 1: Concentric sphere model for a typical code run (HNK 829).

The source was given the spectrum for both neutrons and gamma quanta which was calculated /39/ for the vicinity of the vacuum vessel of the proposed experiment ZEPHYR during DD discharge. This spectrum should closely resemble the spectrum of radiation leaving a JET port.

Results of transport calculations

Results of the calculations are summarized in table 2 and 3. In both cases the source strength has been adjusted to produce an unshielded flux at the detector that has the same magnitude (and spectrum) as the flux expected at the unshielded detector due to direct irradiation from the next vertical port at JET.

Table 2 shows that $\emptyset_\gamma$ at the detector typically amounts to $\sim 10^{-2}$ of the local $\emptyset_n$ (E > 0.4 eV). The gamma flux is caused by neutron interactions inside the shielding, not by the gamma source at the outside (cf line 1 and 2). For Pb widths of less than 20 cm, in contrast, the outer γ-source is not so perfectly shielded and the detector flux of gamma quanta is dominated by the outer gamma source, since e.g. in table 3, line 6 the detector $\emptyset_\gamma$ amounts to $\sim 10^{-1}$ of the local $\emptyset_n$ rather than 10^{-2} as in the case of 30 cm thick lead layers.

Table 2 shows that the thermal neutron flux can be reduced to less than 1/10 of the "fast" ($E > 0.4$ eV) flux by 0.5 % of B in the water. Since thermal neutrons have only a diffusion length of a few cm in boron-free water, the same effect as borating the whole water volume can be achieved by a boron layer of $\lesssim 100$ mg/cm² of B on the outside of the lead.

Fig. 20 shows ϕ_n ($E > 0.4$ eV) and ϕ_γ for 120 cm total shielding width and varying thickness of lead. For a given shielding thickness a minimum of ($\phi_n(E > 0.4$ eV) + ϕ_γ) is obtained near to 15 cm of lead with 105 cm of water. Since ϕ_γ rises drastically for slightly thinner lead-layers it is suggested to keep the lead width to 17 cm and above. The thermal neutron flux is not considered here, since it is assumed that a B-layer just outside the lead reduces the thermal flux to insignificance.

The first two lines in Table 3 show that the water in the shielding can be substituted by $(CH_2)_n$, which is Paraffine or Polyethylene with a minor deterioration in shielding efficiency (factor of ~ 1.5), only, provided the area density of protons ($\varrho_H \cdot \Delta R$) is maintained. Since the proton density in Polyethylene at a typical density of 0.95 g/cm³ is 122 % of that of water a corresponding gain in width can be achieved.

Proposed shielding outlay

Using the data of table 3 for inter- and extrapolation the following shieldings are proposed:

1. Water based shielding

underneath detector

17 cm Pb
100 mg/cm² B (any chemical form*)
80 cm H_2O
total thickness 97 cm

---

[*] e.g. boron loaded (1 %) Polyethylene is supplied by Reaction Experiments, Inc. Terminal Way, San Carlos, California, USA.

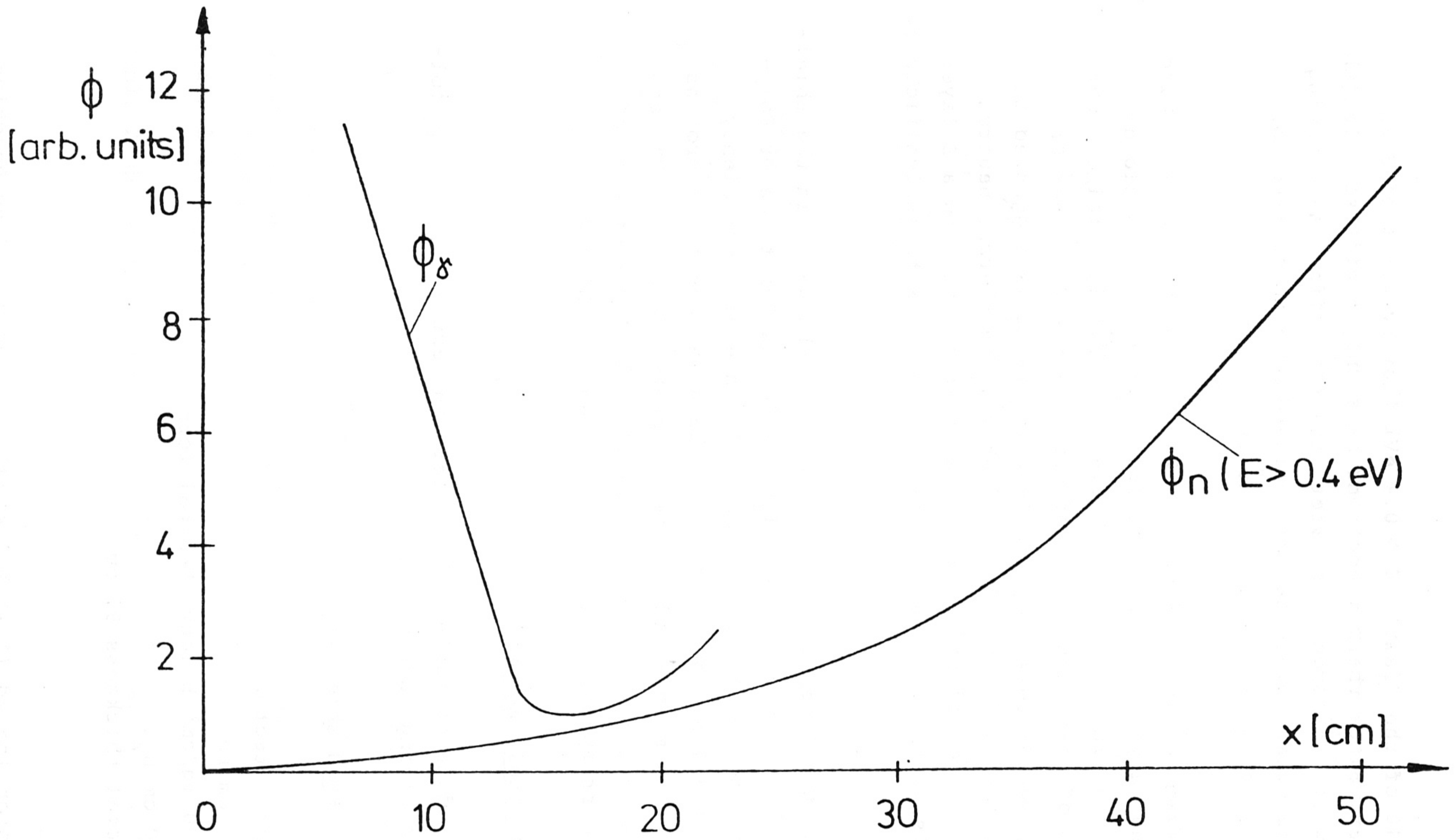

X = Pb thickness

120 - X = H_2O thickness

Fig.20: Neutron and gamma fluxes at the detector for 120 cm shielding width.

lateral to detector

19 cm Pb
100 mg/cm² B
60 cm H_2O
total thickness 79 cm

above detector .

17 cm Pb
100 mg/cm² B
45 cm H_2O
total thickness 62 cm

2. Polyethylene based shielding

underneath detector

19 cm Pb
100 mg/cm² B
64 cm Polyethylene at $\rho = 0.95$ g/cm³
total thickness 83 cm

lateral to detector

20 cm Pb
100 mg/cm² B
54 cm Polyethylene
total thickness 74 cm

above detector

19 cm Pb
100 mg/cm² B
37 cm Polyethylene
total thickness 56 cm

Both the water and the Polyethylene based shieldings will shield the detector to a flux of

ϕ_n (E > 0.4 eV) $\sim$ 6×10^4 n/(cm² · s)
ϕ_n-thermal $\sim$ 1×10^4 n/(cm² · s)
ϕ_γ $\sim$ 1.5×10^4 γ/(cm² · s).

In view of the uncertainties of the detector response to background fluxes and the most interesting plasma discharges with higher neutron source strengths these proposed shieldings can only be considered high risk minimum shieldings. As a cautious approach a shielding one order-of-magnitude more efficient would be appropriate. Such a shield would have a 4 cm wider Pb layer and 24 cm more Polyethylene at all sides.

Radiation passing through the optical duct

The neutron and gamma current leaving the vertical port $I_n \sim 1 \times 10^{14}$ n/s and $I_\gamma \overset{\bullet}{\sim} 2.3 \times 10^{13}$ γ/s causes a directed flux 60 cm above the port of $\sim 9 \times 10^9$ n/(cm² · s) and $\sim 2 \times 10^9$ γ/(cm² · s). That directed flux cannot penetrate through the laterally shifted duct through the shielding to the detector unless the directed flux is dispersed by scattering in materials like the second Bragg crystal, and the walls of the vacuum box. This scattering will thus cause an isotropic source of $\sim 9 \times 10^9$ n/(cm² · s) and $\sim 2 \times 10^9$ γ/(cm² · s) at maximum just underneath the duct through the shielding. For a duct geometry of 2.2 m length and 10 x 10 cm² width, simple ray tracing then results in detector fluxes of

$$\phi_n \approx 1.5 \times 10^6 \text{ n/(cm}^2 \cdot \text{s)}$$
$$\phi_\gamma \approx 3.3 \times 10^5 \ \gamma\text{/(cm}^2 \cdot \text{s)}$$

which is about a factor of 20 above the tolerable fluxes. Since in this case the duct is assumed much longer than the duct length inside the shielding, a secondary shielding around the $\sim$ 140 cm length of duct under the primary shielding is required which could consist of $\sim$ 8 cm Pb and $\sim$ 25 cm Polyethylene (radial widths).

The remaining factor of 20 cm can be achieved by filling the duct with parallel stainless steel plates collimating the optical as well as the neutron and gamma beams penetrating to the detector. For purely optical reasons beam collimation in dispersion direction and perpendicular to that are required. In dispersion direction alone a collimator with 1000 : 1 collimator plate length to width is asked for. If combined with a neutron collimator, neutron and gamma fluxes streaming to the detector would be reduced by a factor of ~ 40.

As mentioned earlier the present design aims at smaller shielding dimensions, but it contains provisions to complete the shielding towards the dimensions found in this section.

Run	Source	Pb width	H_2O width (or $(CH_2)_n$)	Detector flux $\emptyset_n$ (E > 0.4 eV)		Detector flux $\emptyset_n$-thermal		Detector flux $\emptyset_\gamma$	
HNK 838	n only	30 cm	90 cm	2.56×10^4	$\frac{n}{cm^2 \cdot s}$	1.35×10^4	$\frac{n}{cm^2 \cdot s}$	4.15×10^2	$\frac{\gamma}{cm^2 \cdot s}$
HNK 839	n only	30 cm	90 cm* $(CH_2)_n$	3.84×10^4	"	1.90×10^4	"	6.18×10^2	"
HNK 844	n only	1 cm	119 cm	2.39×10^3	"	5.36×10^3	"	2.51×10^6	"
HNK 852	n and γ	10 cm	110 cm	5.43×10^3	"	7.64×10^3	"	1.02×10^5	"
HNK 858	n and γ	15 cm	105 cm	8.13×10^3	"	8.84×10^3	"	1.30×10^4	"
HNK 851	n and γ	20 cm	100 cm	1.20×10^4	"	1.02×10^4	"	1.94×10^3	"
		total shielding width 120 cm in all cases							
HNK 855	n and γ	10 cm	80 cm	5.46×10^4	"	8.15×10^4	"	2.67×10^5	"
HNK 856	n and γ	15 cm	75 cm	8.16×10^4	"	9.84×10^4	"	3.66×10^4	"
HNK 854	n and γ	20 cm	70 cm	2.27×10^5	"	1.33×10^5	"	8.12×10^3	"
		total shielding width 90 cm in all cases							

Table 3: Data to determine composition of detector shielding. Source strength is choosen to give unshielded detector fluxes of $1.00 \times 10^9 \frac{n}{cm^2 \cdot s}$ (and $2.30 \times 10^8 \frac{\gamma}{cm^2 \cdot s}$). Water and $(CH_2)_n$ layers are always unborated.

---

* In this run oxygen atoms are substituted by carbon atoms, keeping the proton density the same as in the case of water.

Run	Source	Weight-percentage of B in water	Detector flux $\emptyset_n$ (E > 0.4 eV)	Detector flux $\emptyset_n$-thermal	Detector flux $\emptyset_\gamma$
HNK 829	n and γ	0.5 %	$2.48 \times 10^4 \frac{n}{cm^2 \cdot s}$	$1.60 \times 10^3 \frac{n}{cm^2 \cdot s}$	$2.60 \times 10^2 \frac{\gamma}{cm^2 \cdot s}$
HNK 837	n only	0.5 %	2.48×10^4 "	1.60×10^3 "	2.46×10^2 "
HNK 836	n only	0.125 %	2.54×10^4 "	4.37×10^3 "	2.89×10^2 "
HNK 840	n only	0.031 %	2.56×10^4 "	8.47×10^3 "	3.46×10^2 "
HNK 838	n only	0	2.56×10^4 "	1.35×10^4 "	4.15×10^2 "

Table 2: Calculations to determine the effect of borating the H_2O shielding layer. Shielding thicknesses are in all cases 30 cm Pb and 90 cm H_2O (with B). Source strength is choosen to give unshielded detector fluxes of $1.00 \times 10^9 \frac{n}{cm^2 \cdot s}$ (and $2.30 \times 10^8 \frac{\gamma}{cm^2 \cdot s}$).

4.2 Technical description of design drawings

4.2.1 Solution of problem

The double crystal spectrometer (the assembly is given in Fig. 21) comprises three main component groups clearly distinguished by function. These are

A) Combined rotation and swivel unit for crystal K1
(Drawing No. S5 DKS 001001) (Fig. 22)

B) Combined rotation and adjustment unit for crystal K2
(Drawing No. S5 DKS 001002) (Fig. 23)

C) Vessel with base plate and collimator
(Drawing No. S5 DKS 001003) (Fig. 24 and 25)

The general plan and the distribution into the groups is sketched in Fig. 26.

The most critical group is the combined rotation and swivel unit for the beam entrance crystal K1 (A). This is where all the functional and ambient problems arise together for the double-crystal monochromator, i.e. high crystal setting precision, 5 Hz high-amplitude oscillation, vacuum, radiation and magnetic field.

The solution for the rotation and swivel unit (A) uses angle encoders, motors, gears and bearings.

The difficulty in selecting components is to ensure that they are compatible with the ambient of vacuum, radiation and magnetic field conditions. As it was not possible to conduct preliminary tests in the context of the design contract, reliable information had to be obtained from suppliers. It was found here that the biggest problems were encountered in procuring shaft encoders conforming to the specifications.

Although for optical encoders it was not possible to obtain any reliable information on their radiation resistance from suppliers, information from KfK Karlsruhe and KFA Jülich revealed that optical encoders subjected to X-radiation in doses of up to 10^8 rad worked perfectly. Optical encoders and multipole resolvers appear to be conditionally suitable for application in double-crystal spectrometers.

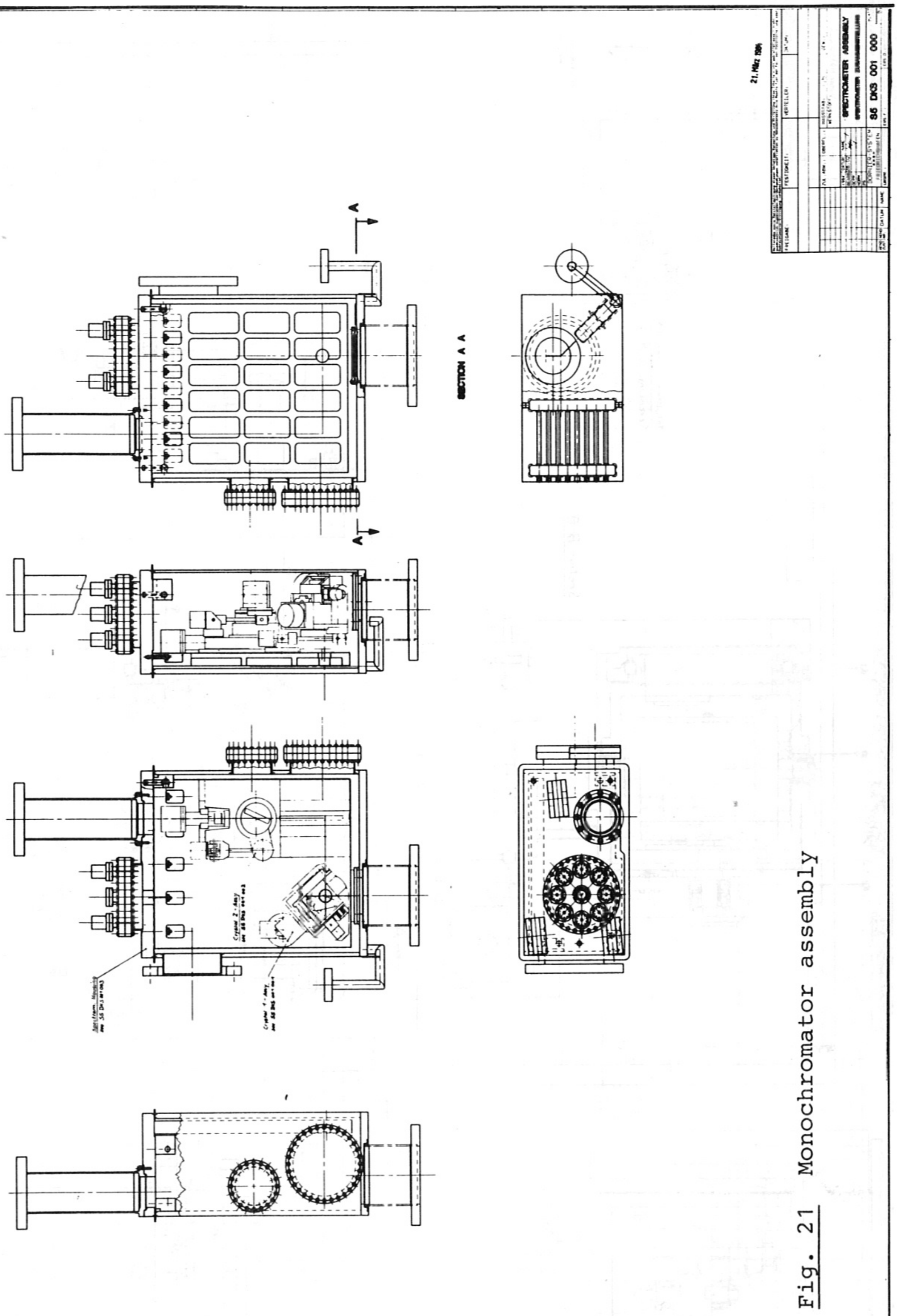

Fig. 21 Monochromator assembly

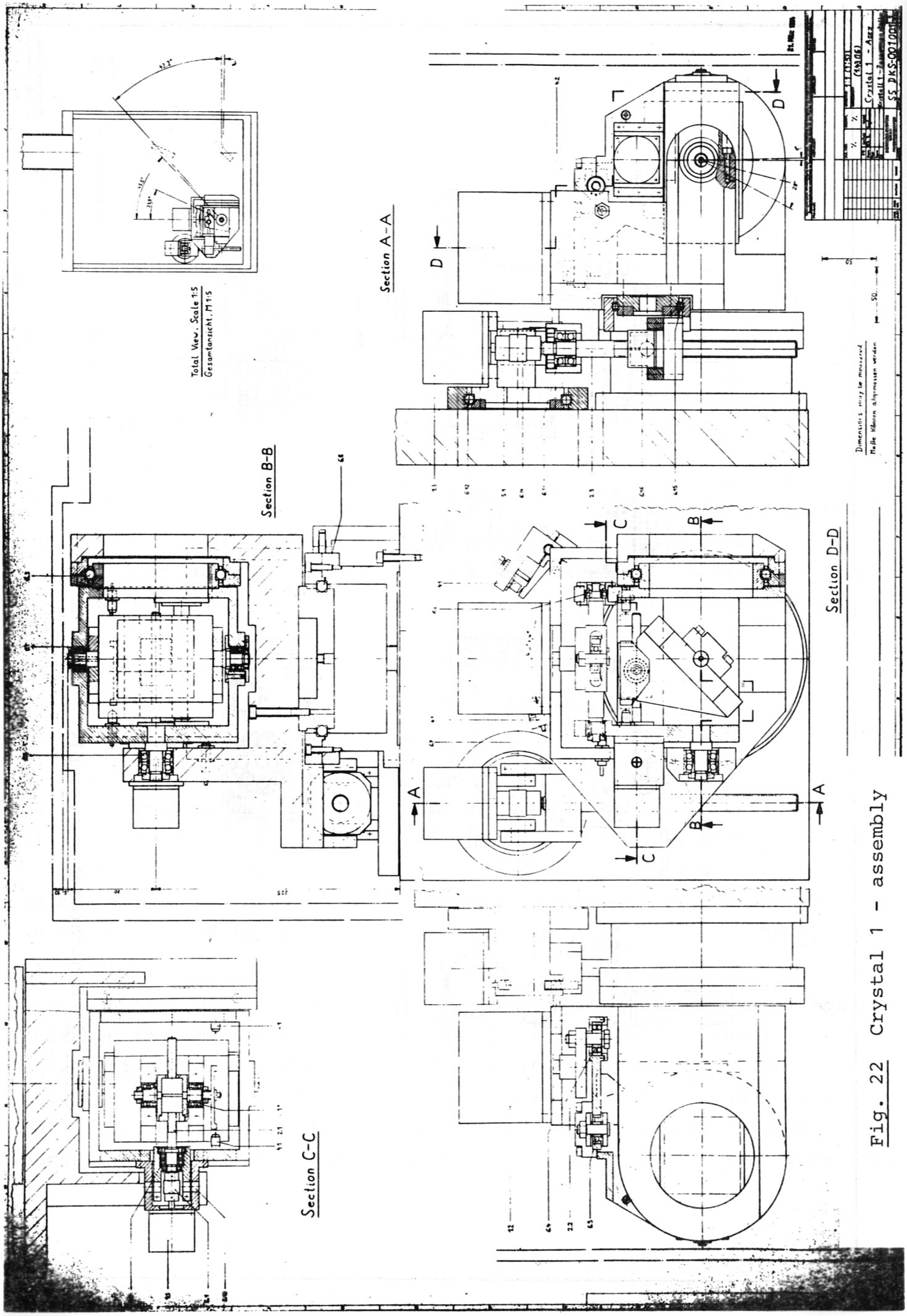

Fig. 22 Crystal 1 - assembly

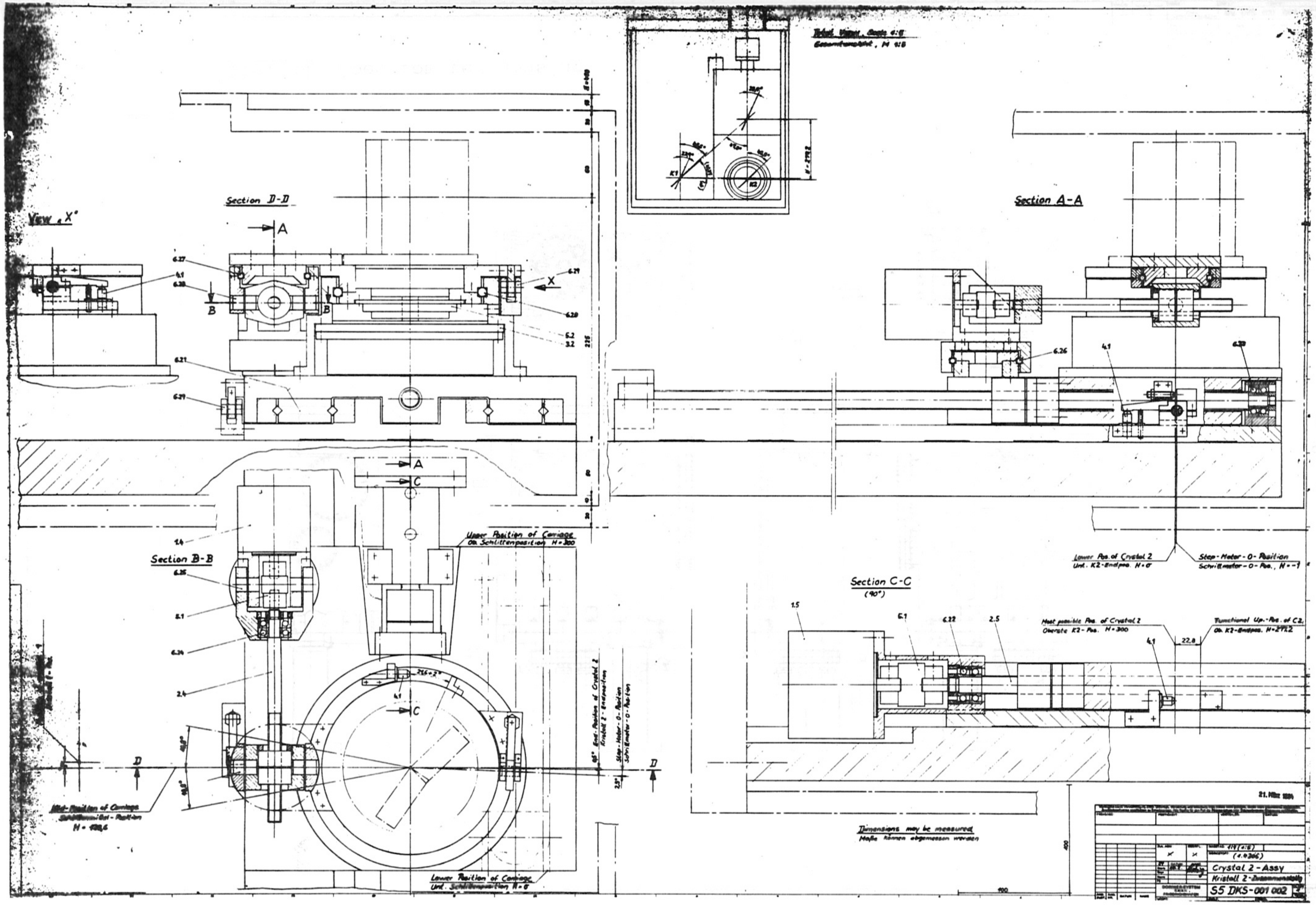

Fig. 23 Crystal 2 - assembly

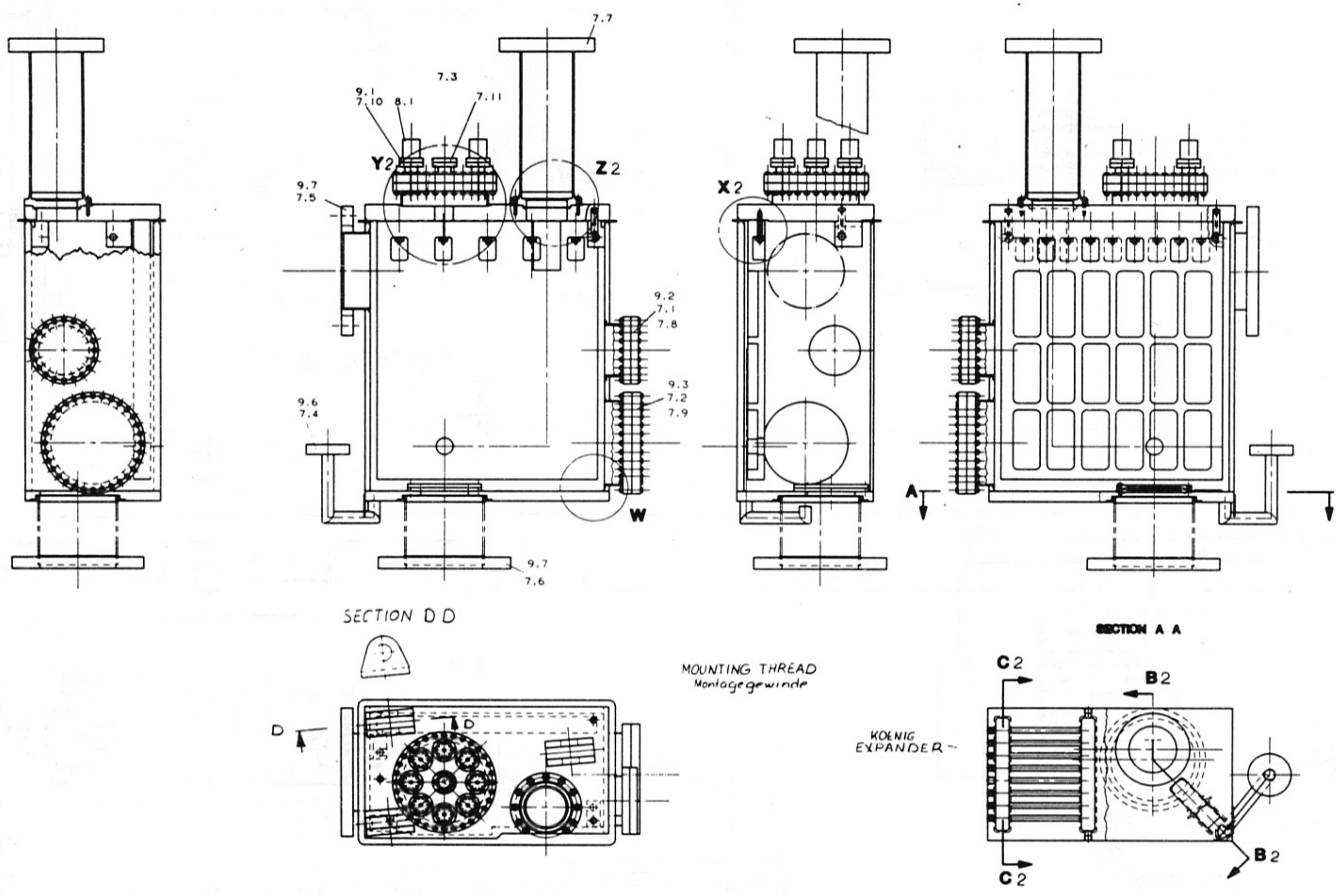

21. März 1984

FREIGABE:
FESTIGKEIT:
VERTEILER:
DATUM:
ZUL. ABW.:
OBERFL.:
MASSSTAB: 1 5
GEW.:
WERKSTOFF:
1984 DATUM NAME
BEARB. 28.2. Kud
SPECTROMETER HOUSING
REZIPIENT MIT KOLLIMATOR
DORNIER-SYSTEM
FRIEDRICHSHAFEN
85 DKS 001 003
ÄNDERUNG ZUST. ÄNDERUNG NR. DATUM NAME

Fig. 24 Spectrometer housing

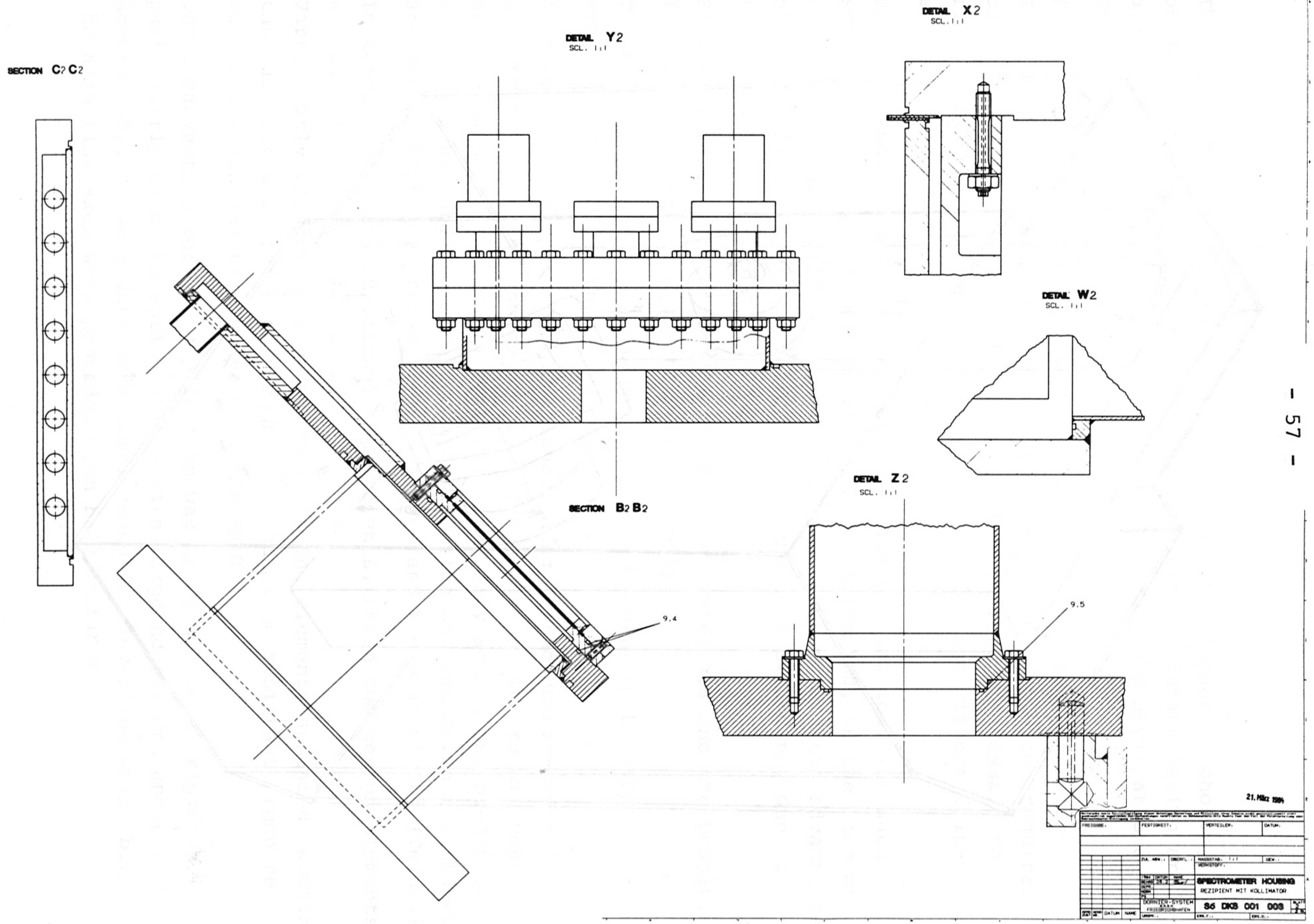

Fig. 25 Spectrometer housing - detail

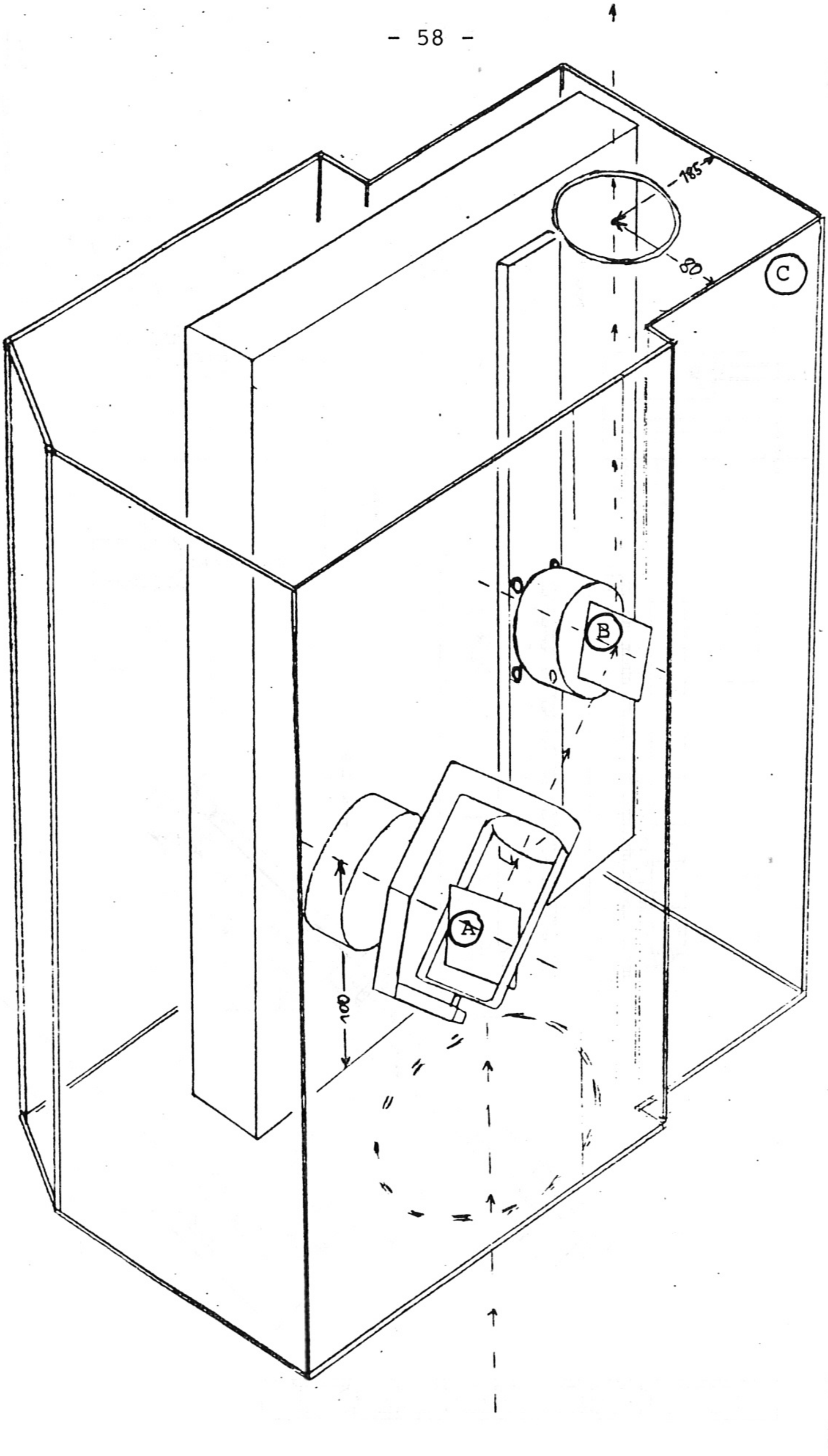

Fig. 26 General plan indicating the three component groups of the spatial scan double crystal monochromator

The combination of stepping motors with limit switches is chosen, because motors of vacuum compatible, radiation resistant design are available and, furthermore, references on comparable applications can be submitted.

The angular resolution of even a high-resolution stepping motor (1000 s/rev) is of course not sufficient for the resolution required of the double crystal spectrometer. It was therefore necessary to find a gear which works absolutely free of play and without slip-stick effect.

It was spindle gears that were selected for application. Threaded spindles can be manufactured with high precision and, in the form of rolling threaded spindles as selected here, they afford the advantages of low nonlinearity (3 to 5 arc seconds) and high efficiency due to rolling kinematics.

Further advantages are freedom in selecting materials and the possibility of prestressing absolutely free of play.

The use of spindle gears was possible here because it is only small angular ranges that have to be set.

Another essential point for the functioning of the double-crystal monochromator is the choice of bearing components. The requirements stipulated here, as freedom from backlash, easy access and precision as well as suitability for vacuum application and radiation resistance are met by both prestressed ball bearings and flexural pivots (Teldix).

In keeping with the functional requirements, these two design elements are used in the monochromator.
Particularly the application of cross spring elements appeared tempting: they are suitable for high vacuum, are radiation resistant, require no lubrication and take up very little space.

One disadvantage for our application was the low lateral rigidity particularly of cross spring joints with large adjustment angles. Accordingly, these joints were mainly used for levelling work, but the adjusting axes were provided with ball bearings.

The work on the rotation and swivel unit K1 had already anticipated various features for the designing of the combined rotation and adjustment unit K2 (B). The same functions were to be performed with the same design elements.

As a suitable linear track only a track on roller bearings proved suitable. In the double-crystal monochromator it is intended to use a longitudinal track with roller bearing system. The roller bearing system is preferred to the ball bearing system because it promises greater rigidity.

There was not much scope available in designing the vessel with collimator (component group C). The vessel configuration is largely prescribed by spatial conditions, the design of spectrometer components, and the choice of materials. The design is described in the following section.

The solutions for the individual components and groups have been described and explained in the foregoing sections. An overall description of the spectrometer design is now presented. Attention is drawn to the following drawings:

Design of double-crystal spectrometer	S5 DKS-001000
Crystal 1, general view	S5 DKS-001001
Crystal 2, general view	S5 DKS-001002
Vessel with collimator	S5 DKS-001003
Calibration arrangement K1	S5 DKS-001004

Mechanics

Combined rotation and swivel unit for crystal K1 (Fig. 27)

The rotation and swivel unit has three functions:

- Bragg angle setting of crystal K1
- swivel axis setting in the direction of the beam emerging from K1
- performance of a 5 Hz swivel motion.

The crystal holder is supported on two sides in angular ball bearings of precision class P4 prestressed in pairs. The angular ball bearings are prestressed and have the compression angle of 25° favourable to high rigidity values. The Bragg angle is set with a precision-threaded spindle with a total pitch error of ± 0.0025 mm over an adjustment range of 300 mm and a nonlinearity of 1 to 2 µm per rotation. The spindle is driven by a stepping motor. The crystal holder, including the adjusting spindle, the stepping motor and the mechanical reference switch, is accommodated in the so-called swivel lantern (see Fig. 27). The swivel lantern is of particularly rigid design to prevent the 5 Hz swivel motion from being transmitted to the fixed Bragg angle position of the crystal holder relative to the lantern. The bearing of the lantern is correspondingly rigid. The principle requires that the beam exit be located in the axis of the swivel lantern, and so the bearing has to be built around the beam (7 x 7 cm). This is accomplished with a 4-point wire bearing (Franke system). The second bearing location is a movable bearing with prestressed angular ball bearings.

The lantern performs a 5 Hz swivel motion with a double amplitude of 29°. It is driven by a stepping motor. The reference position is detected with an inductive proximity switch. The continuous rotation of the motor is transformed to the required $\pm 14.5^{\circ}$ swivel by means of a crank gear. Stable mounting of the swivel lantern is provided by the main fork, to which the whole swivel drive (motor and crank gear) and the inductive reference sensor are also attached. The fork surmounts a specially designed turntable firmly flanged to the base plate of the spectrometer. The turntable is used to set the swivel axis. The drive in this case is also a stepping motor with spindle gear. A mechanical precision reference position switch is also provided.

In anticipation of the description of the control concept it is mentioned here that the operating position is realized solely with the stepping motors, i.e. during spectrometer operation no direct information on angle is available. The stepping motors are controlled by

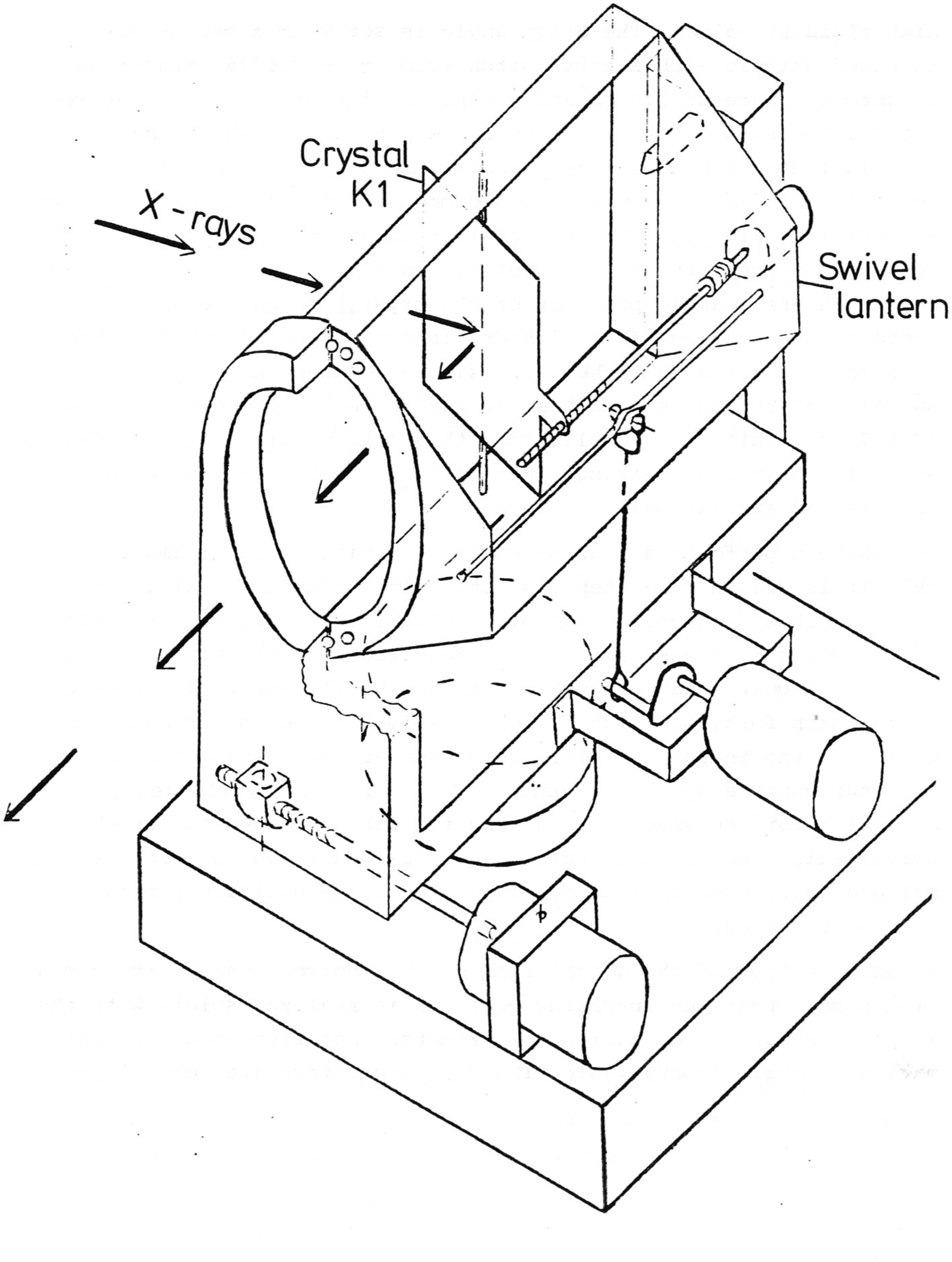

Fig. 27 Combined rotation and swivel unit

computer by means of pairs of calibrated values (number of steps = f (angle)). To determine the actual transmission function in the final installation state without vessel, it is intended to adapt a high-resolution angle encoder (ROD 800) for all independent axes of the rotation and swivel unit. This is shown in drawing S5 DKS 001004. Calibration can be performed separately and consecutively with one and the same angle encoder.

The same encoder can be used later for the fixed installation in the K2 turntable, which is described in the following.

Combined rotation and adjustment unit for crystal K2

The rotation and adjustment unit has two functions:

- Bragg angle setting of crystal K2
- longitudinal positioning of crystal K2 on the intersection of the collimator axis C with the swivel axis S.

The main function of this component group is to select the wavelength, i.e. the Bragg angle has to be set with extreme precision and be maintained. The total angular deviation ought not to exceed ± 5 arc seconds, i.e. as the sum tolerance for both components of this group.

The holder of crystal K2 is reproducibly mounted on a precision turntable which is positioned with a stepping motor by means of a spindle gear with sufficient resolution. Integrated in the turntable is a high-resolution angle encoder which directly controls the rotary motion of the table.

The turntable with drive, angle encoder and mechanical reference positioner is mounted on the carriage of a linear track system. The track system (cross roller deflection system) is positioned with a stepping motor by means of a spindle gear. No special requirements are prescribed in the way of longitudinal positioning precision and the general track quality. Rotation of the table is, however, subject to restriction. In any longitudinal position it ought not to exceed 5 arc seconds (half the total tolerance (see Fig. 28)).

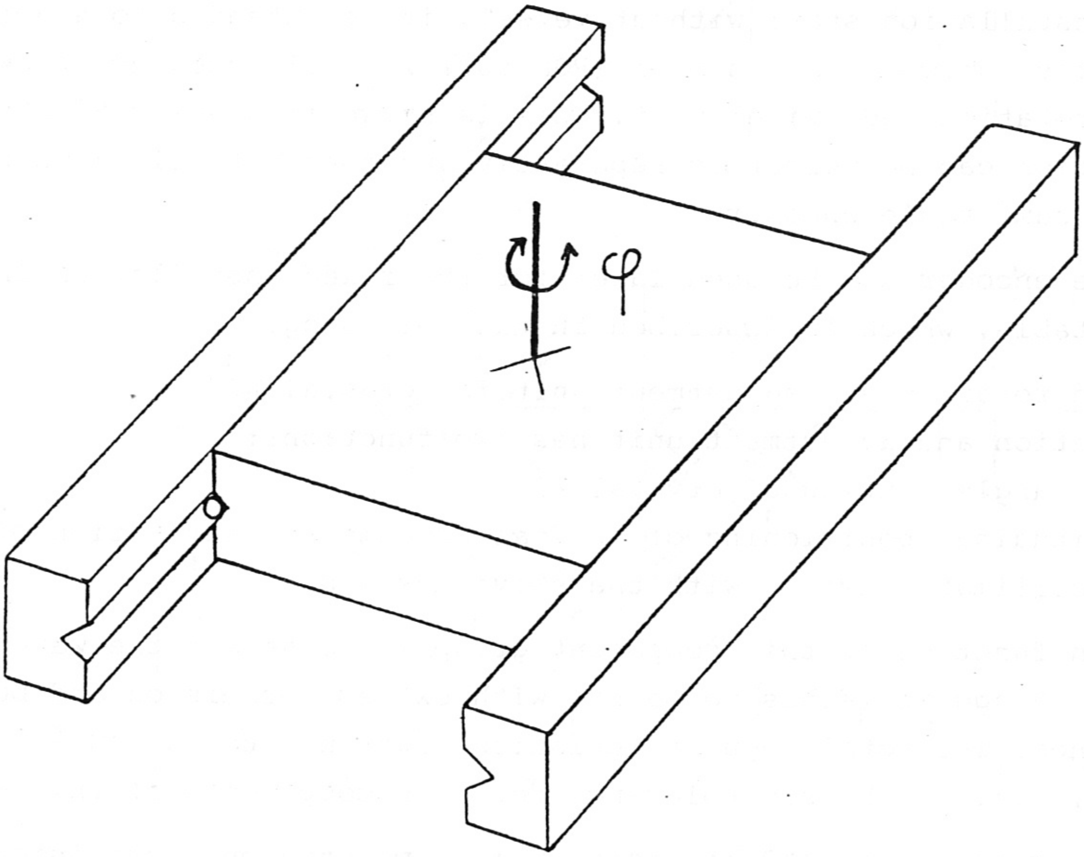

Fig. 28 Definition of table rotation: By mechanical inaccuracies the displacement table performs small angular motions in φ - direction around the vertical axis, while travelling in longitudinal direction. The mechanical accuracy must be such that these angular motions are limited to 5 arc seconds.

Vessel with base plate and collimator

This component group has two main functions:

- provision of a stable, invariant base for the optical components
- production of an evacuable volume with defined connections to the torus and detector.

The two functions are somewhat in contradiction to one another since even very thick walls of such a vessel are deformed on evacuation to an extent exceeding the precision specified here. Solution of this problem calls for separation of the functions. An appropriate design would, however, involve considerable outlay, and so a compromise has been made. The top vessel plate (cover) has to perform both functions. It is accordingly so thick that its deformation is acceptable. This makes the structure of the vessel relatively simple and straightforward (see Fig. 29).

The stable vessel cover is the central component of the vessel. The collimator tube and the spectrometer base plate are exactly aligned with one another on the outside and inside, respectively, and bolted to the cover. The vessel cover also contains the electrical feedthroughs and, on the top side, the points for the spectrometer suspension.

The spectrometer baseplate hangs free in the vessel without any further contact with a vessel wall, so that no special precision is required of the other walls. The vessel and cover are welded together with a "soft" double-flanged seam, i.e. bending moments are not introduced into the cover.

The connection to the torus is effected from the vessel base via a welded corrugated bellows. At this location there is a replaceable foil which separates the vessel volume from the torus port volume. The reason for this is the enhanced vacuum requirement in the port volume: 10^{-8} mbar compared with the 10^{-6} mbar of the vessel volume.

The foil has to be replaceable, the crystals K1 and K2 as well. For this purpose one of the vessel walls is provided with two mounting

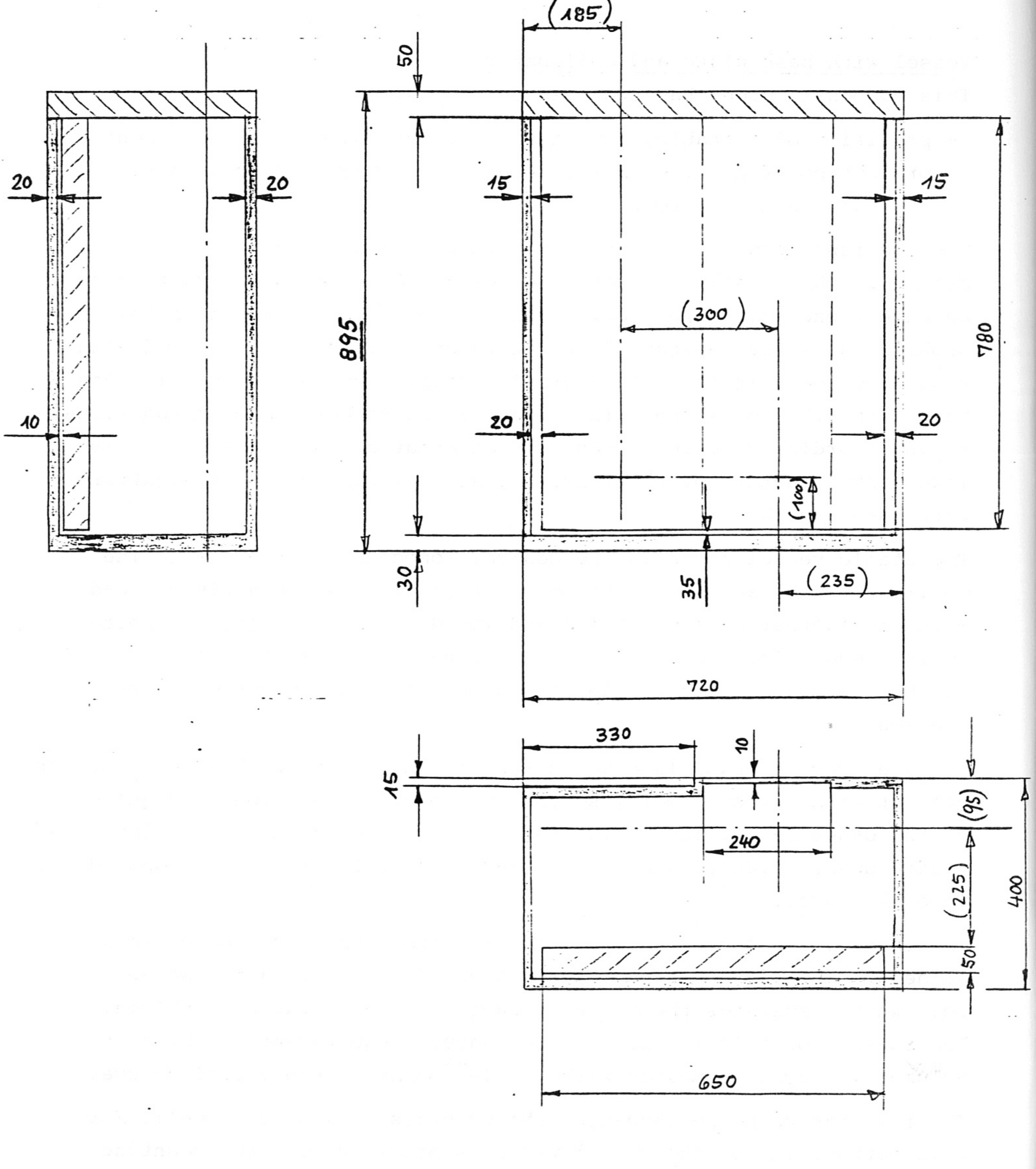

Fig. 29 Vacuum vessel for spatial scan double crystal monochromator

apertures which are sealed with flanges having metal gaskets.

The main vacuum line is connected to the vessel via the JET remote-handling flange. The port volume can be separately evacuated.

4.2.2 Control and drive

The control and drive concept is described in drawing No. S5 DKS-001005 (Fig. 30). The choice of the control and drive concept was largely governed by the choice of components. The correct functioning of high-resolution angle encoders is not guaranteed by the manufacturers for the ambient conditions of the spectrometer.

The control and drive system presented here affords a clear interface to the evaluating computer and works with radiation and vacuum-compatible components.

The central idea is characterized by the positioning by stepping motors with high-precision mechanical reference switches and the calibration before operation by means of a high-resolution angle encoder, which allows to eliminate all systematic errors.

In component group A, the combined rotation and swivel unit, this concept is realized in the same way for all positioning work.

The Bragg angle setting of crystal K1 with the stepping motor and spindle gear, including the link kinematics, affords a resolution of 8.6 arc seconds. The required adjustment range of 21.6° is extended by 2° on each side and provided with mechanical end switches which prevent blocking of the spindle drive. The switch at -2° is a precision switch which also indicates the reference position of the stepping motor.

The block circuit diagram now shows the swivel axis setting. The stepping motor, spindle gear and link kinematics provide a resolution of 3.2 arc seconds. The adjustment range is extended by $\pm 2^{\circ}$ and two end switches are provided, the -2° switch being responsible for indicating the reference position.

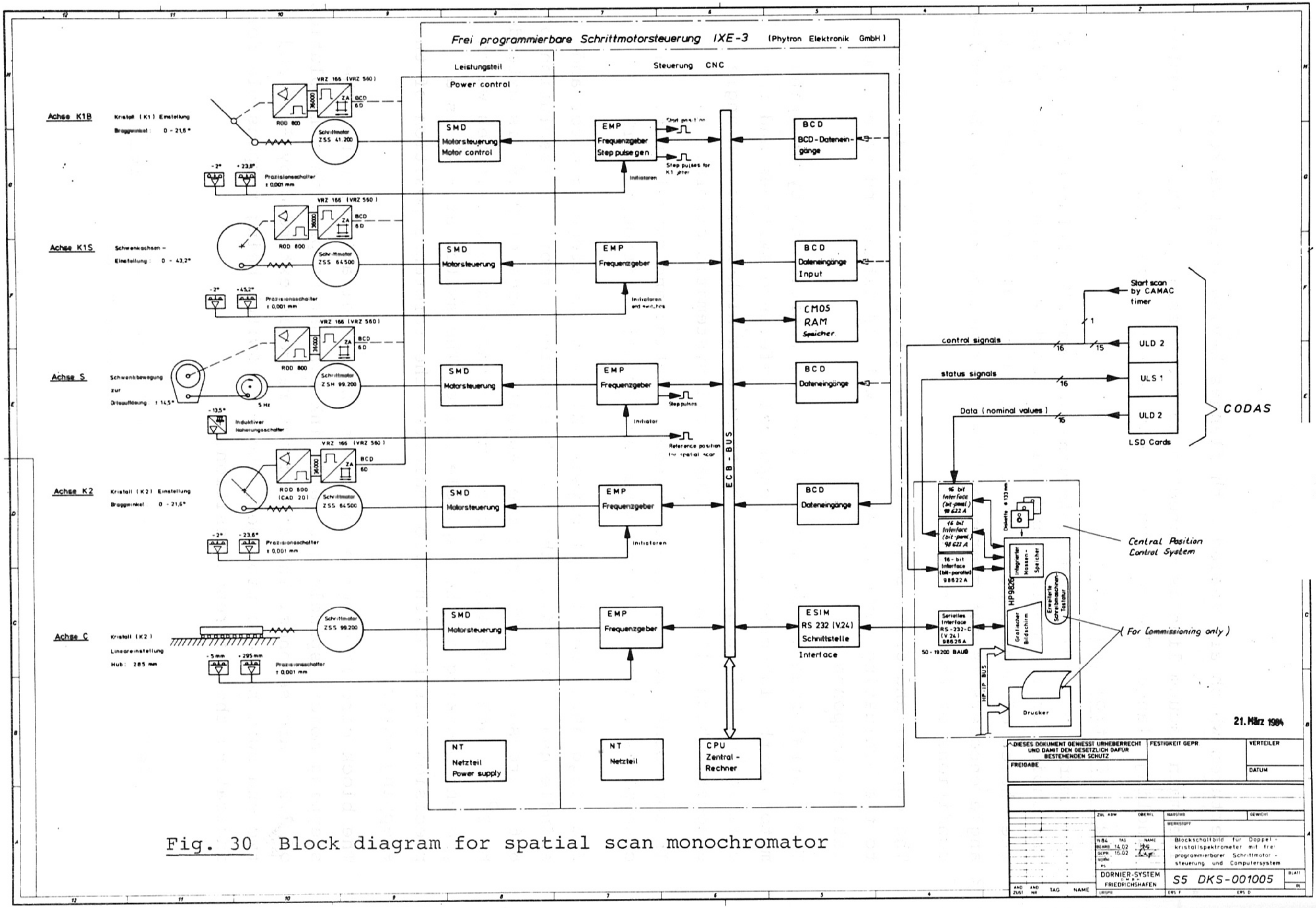

Fig. 30 Block diagram for spatial scan monochromator

The third motion performed by the rotation and swivel unit is the swivel motion with a frequency of 5 Hz. The stepping motor, which runs at a constant 5 r.p.s., acts on a crank gear which moves the swivel lantern ± 14.5° via a connecting rod. The 400 steps of the motor provide a resolution of 4.35 arc minutes, it being possible to fix each step (fall-back position). Serving as reference position switch is an inductive switch at - 13.5° (the vertical). For all axes high-resolution angle encoders can be adapted for calibration (see drawing No. S5 DKS-001004). (Fig. 31)

In principle, the basic idea of the control system described above is also applied to component group B. In keeping with the special requirements there, however, the concept is slightly modified.

The Bragg angle setting for K2 is performed by very same way as for K1, but with a resolution of 1.7 arc seconds. End switches and a reference position switch are also provided. In addition, this setting unit is to have an integrated angle encoder. This will be either an optical encoder with a precision of 2 arc seconds (ROD 800, Heidenhain) or a multipole resolver with a precision of 5 arc seconds (CAD 20, Sagem). The additional incorporation of an encoder at this location seems appropriate since a temperature change of 1° at the spindle already results in an angular shift of 3 arc seconds. Of course, the setting unit will also be calibrated beforehand with the same angle encoder, so that the calibration points are available in the computer in the event of encoder failure.

Only modest requirements are imposed on the positioning precision of the longitudinal track. In addition, the setting spindle acts directly on the carriage, without link kinematics as in the case of the rotation setting units. The stepping motors and spindle gear provide a resolution of 5 µm. Reference and end switches are provided. The modest precision required makes it possible to dispense with prior calibration.

It would be beneficial, however, to include the linear motion in the calibration of the Bragg angle setting for K2. This would make it possible to calibrate out the carriage rotation, which depends solely on the track quality.

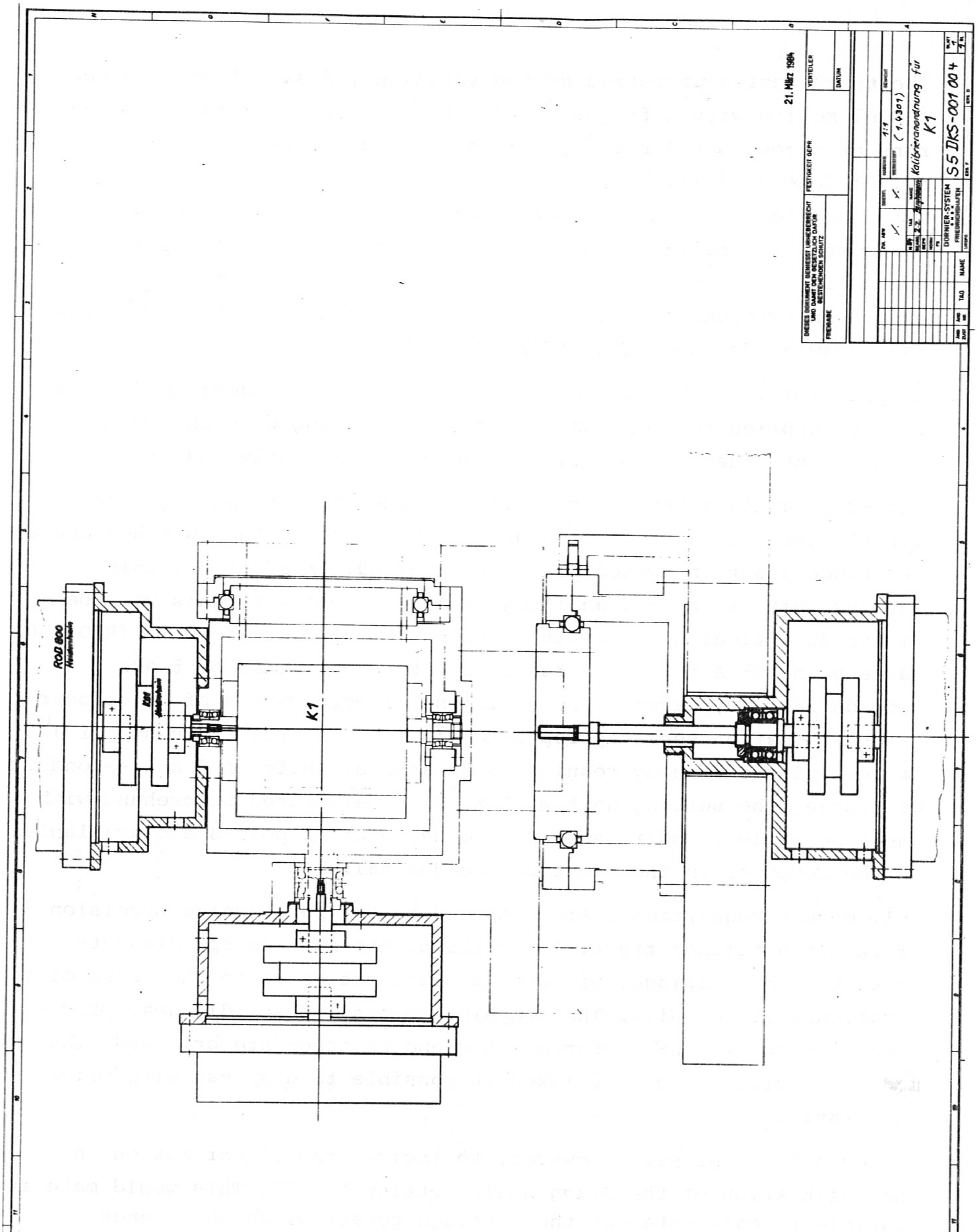

Fig. 31 Calibration device for K1

4.2.3 Expected mechanical accuracy

The necessary high mechanical accuracy of the spatial scan double crystal monochromator mainly concerns the Bragg angle positions of both crystals. The angular accuracy in the "vertical" plane (perpendicular to the Bragg angle direction) with several arc min. as well as that for the spatial scan with many arc min. can be obtained without difficulties. For the Bragg angle positioning of crystal 1 and crystal 2 there are several error sources, the contributions of which to the respective Bragg angle inaccuracies are given in the following table:

Table Mechanical inaccuracies

Error source and its contribution to Bragg angle position	Crystal 1 arc sec.	Swivel axis arc sec.	Crystal 2 arc sec.
Calibration error:			
± 1/2 step width	± 5	± 5	± 1
ROD 800 encoder accuracy	± 1	± 1	± 1
Coupling	± 0.5	± 0.5	± 0.5
Step error in reference switch (± 1 step)	(± 8.6)[+]	(± 3.1)	(± 1.7)
Direct dynamical error by swivel motion	± 0.6	-	-
Error by swivel motion due to motion inaccuracies of the lantern bearings	± 1.2	-	-
Error for 1° C temperature increase of the spindle	(3.3)	(4.3)	(4.2)
Tumbling motion of longitudinal displacement unit	-	-	± 2.5
Base error for crystal 1 due to inaccuracy of swivel axis positioning	± 3	-	-
Sum	± 11.5	± 3	± 5

[+] Values in brackets can be eliminated by calibration

These mechanical accuracies should allow to operate the spatial scan double crystal monochromator for the aims envisaged. Moreover, there is the possibility of wobbling the crystal K1 around the Bragg angle position by about 30 arc seconds with a frequency of up to 30 Hz, which is higher than the swivel frequency. This will allow to test directly (and control) the Bragg angle synchronism during the swivel motion of the crystal K1. This control is also given in the block diagram of Fig. 37 in chapt. 4.5.

4.2.4 Transmission of the spatial scan double crystal monochromator, calibration and expected performance

During the swivel motion of crystal K1 in the swivel lantern there are several items that may change the transmission of the spatial scan double crystal monochromator as function of the swivel angle. First there are the vignetting effects of the port boundaries as well as the change of crystal surface during the swivel motion, which can be calculated. Moreover, there are losses (which for the present design can go up to 15 %) due to the fact that for large angles of the swivel motion (for the spatial scan) the beam has an angle to the poloidal plane and hence is reduced at the support grid of the thin foil. A further dependence originates from the oblique transmission through the thin foil, which effect is strongly wavelength dependent. Another contribution comes from the polarization changes during the spatial scan motion.

All these considerations suggest to apply a large area (homogeneous) X-ray calibration source with the possibility to change the wavelength in order to measure the monochromator transmission for every crystal combination during and as function of the spatial scan motion.

The expected performance of the spatial scan double crystal monochromator is characterized by the count rate for an impurity spectral line at a certain impurity concentration. As carried out in /3/, the count rate is given by

$$\dot{N} = I \cdot T \cdot S \cdot \frac{h_c}{b} \cdot \eta ,$$

where I is the line intensity, T the monochromator transmission (including the geometrical and foil transmission as well as the product of the crystal integral reflectivity R and half the peak reflectivity P(o)/2), S the source area, h_c the crystal height, b the distance of the crystal from the source and η the detector efficiency.

For the He-like Ni XXVII line at $\lambda = 1.59$ Å with the transition $1s\,^1S-2p\,^1P$ the intensity is

$$I = 5.2 \cdot 10^{15} \cdot n_{Ni}/n_e \; [\text{photons}\cdot\text{cm}^{-2}\cdot\text{s}^{-1}\cdot\text{ster}^{-1}]$$

where n_{Ni}/n_e is the (relative) impurity concentration of nickel in the JET plasma of typically 100 cm emission length, an electron density of $3\cdot10^{13}$ cm^{-3} and a temperature of $T_o = 5$ keV.

With $T \simeq 8\cdot10^{-6}$, $S \simeq 80$ cm^2, $h_c \simeq 7$ cm, $b \simeq 400$ cm and $\eta \simeq 0.5$ the count rate is in the order of

$$\dot{N} \simeq 3 \cdot 10^{10} \cdot n_{Ni}/n_e \; [s^{-1}],$$

which indicates that nickel impurity concentrations can be determined by absolute line intensity measurements even at impurity concentrations much less than $n_{Ni}/n_e \simeq 10^{-5}$.

Similar estimates can be made for other impurity species. For quantitative impurity concentration evaluation the above mentioned calibration has to be performed.

4.3 Positioning control

4.3.1 Stepping motor control

A freely programmable stepping motor control unit, Type IXE-3 supplied by Phytron-Elektronik, was chosen for moving and positioning the crystals. The IXE-3 is a processor-controlled path and mode control for connection to an RS-232 interface. The control unit is designed to allow independent setting and operation of the five axes. The necessary information on acceleration and deceleration ramps, speeds and nominal positions for every axial motion is conveyed to the control unit by a control program via the RS-232 interface. It is also possible to transfer status signals about motor operation, end switches and control inputs via the computer interface. If incremental encoders are used for control and calibration purposes, it is also possible to read off their absolute values.

Structure of stepping motor control

The control unit is of modular structure and is accommodated in a 19" rack with 3 vertical units and a total depth of 360 mm. It is supplemented with two 19" power racks of equal dimensions. The power electronics of type series SMD is adapted to the stepping motors and the specific application.

4.3.2 Central position control system

General

As an intelligent link between the motor control unit and the CODAS system a computerized central position control system will be used. Its main purpose is to translate the data (nominal values) and commands received via LSD outputs into the proper motion programmes and to return status signals of the motor control unit to LSD inputs. For the communication with the motor control unit a RS-232 interface will be used. The LSD ports are connected via 3 parallel 16-bit I/0 ports. The central control unit will also store the calibration values obtained by the initial calibration procedure in a non-volatile memory. The HP 9826 is proposed as a powerful and convenient mediumpriced unit to act as central position control system. Besides the extended typewriter keyboard (ASC II letter type), the HP 9826 incorporates an integrated mass store (floppy disk) with 260 K byte and a terminal for alphanumeric and graphic display. Extended BASIC, PASCAL and HPL are optionally available as programming languages. The user store can be enlarged to 512 K byte, depending on the programming language.

A bus-compatible printer is controlled via the integrated HP-IB interface, Data communication is done with the interface (98626 A) via the serial interface.

The keyboard, the terminal, the printer and the floppy disk are only intended for test and commissioning. In the advanced operational phases the system will be operated only via the CODAS interface.

4.3.3 Connection to CODAS

The connection to CODAS is shown in Fig. 37.
As already mentioned, the 16 bit LSD data line is used to transmit the desired nominal values (Bragg angle, constant offset between crystals, fixed spatial scan angle). Additional command and feedback signals control the data transfer of this line.
Other LSD signals are used to define the desired mode of operation (spatial scan, fine wobbling, crystal exchange) and to provide information about the status of the positioning system (ready, in position, error).

The spatial scan and the fine wobbling of the first crystal is started by a CAMAC timer.

The small amplitude wobbling motion of 30 Hz is performed by the Bragg angle drive of crystal 1 with step pulses in either direction generated by the stepping motor control. Both the wobbling and the spatial scan motion are recorded during the measurement phase. For this purpose reference and stepping pulses of the two axes are connected to two CAMAC latching scalers. The positions represented by the scaler contents are stored together with the detector counts (measured by another latching scaler) in a CAMAC memory.

4.4 Vacuum control

The schematic diagram of the vacuum system is shown in Fig. 32. The vacuum system will be controlled by a Simatic control system in connection with two Edwards controllers (Fig. 33 and 34). The symbolic representation of time loops used in the vacuum flow chart is explained in Fig. 35.

Although the foil between the spectrometer and the bellows section can withstand a pressure difference of one bar, it is intended to apply only moderate pressure differences in normal operation. As a first step in the pumpdown sequence the spectrometer and the bellows section will be pumped together to a pressure of approximately 20 mbar. Then the spectrometer valve is closed and the pumping of the bellows continued. In this phase the tightness of the foil can be tested. When a sufficient bellows vacuum is achieved, the torus valve can be opened and the bellows evacuation valve closed. It must be noted that with reasonable pumping time (24 hours) only a bellows pressure in the order of several 10^{-8} mbar can be achieved. After opening the torus valve the spectrometer evacuation is continued. Details of the pumping and venting sequences can be taken from the flow chart Fig. 36.

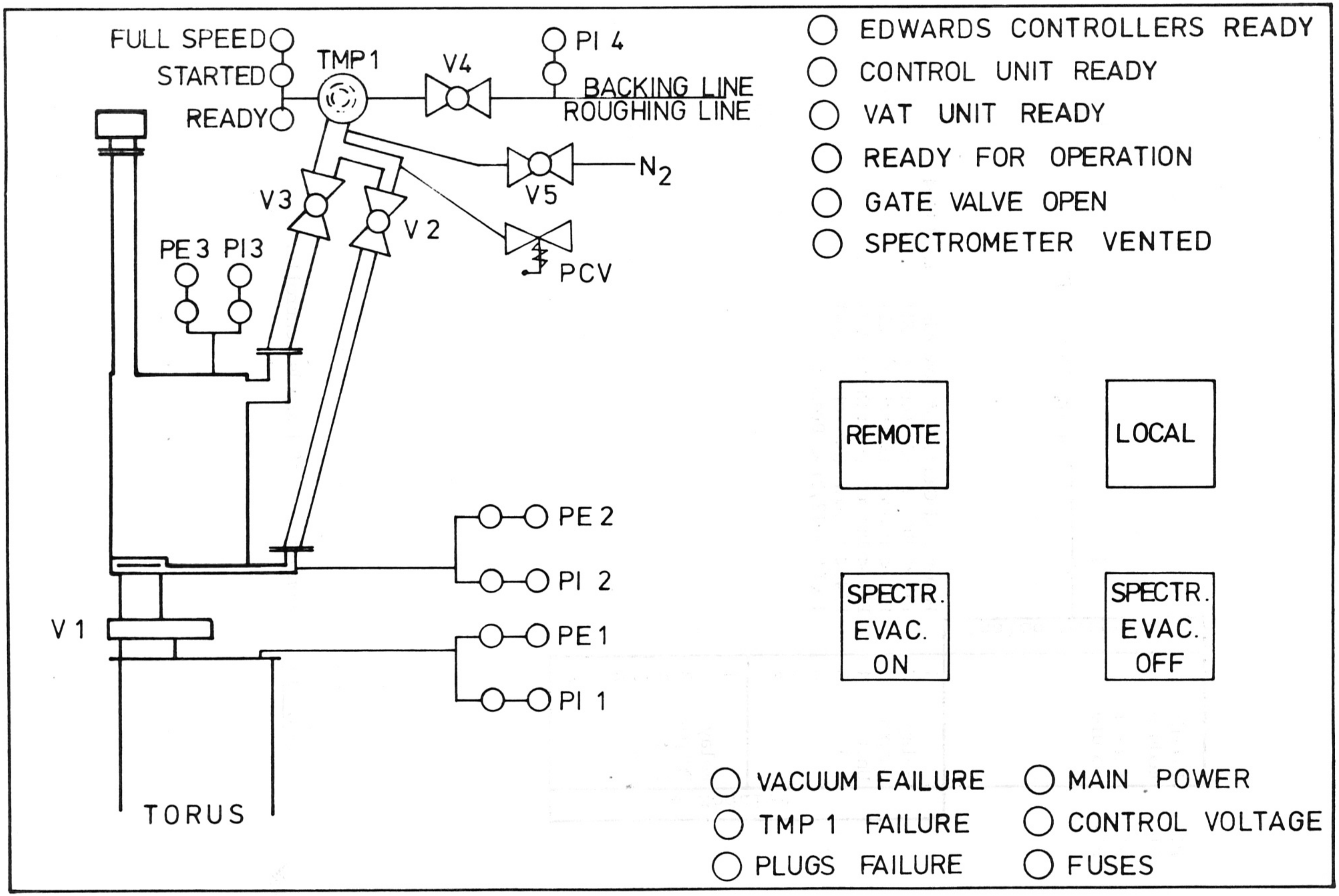

Fig. 32 Vacuum scheme

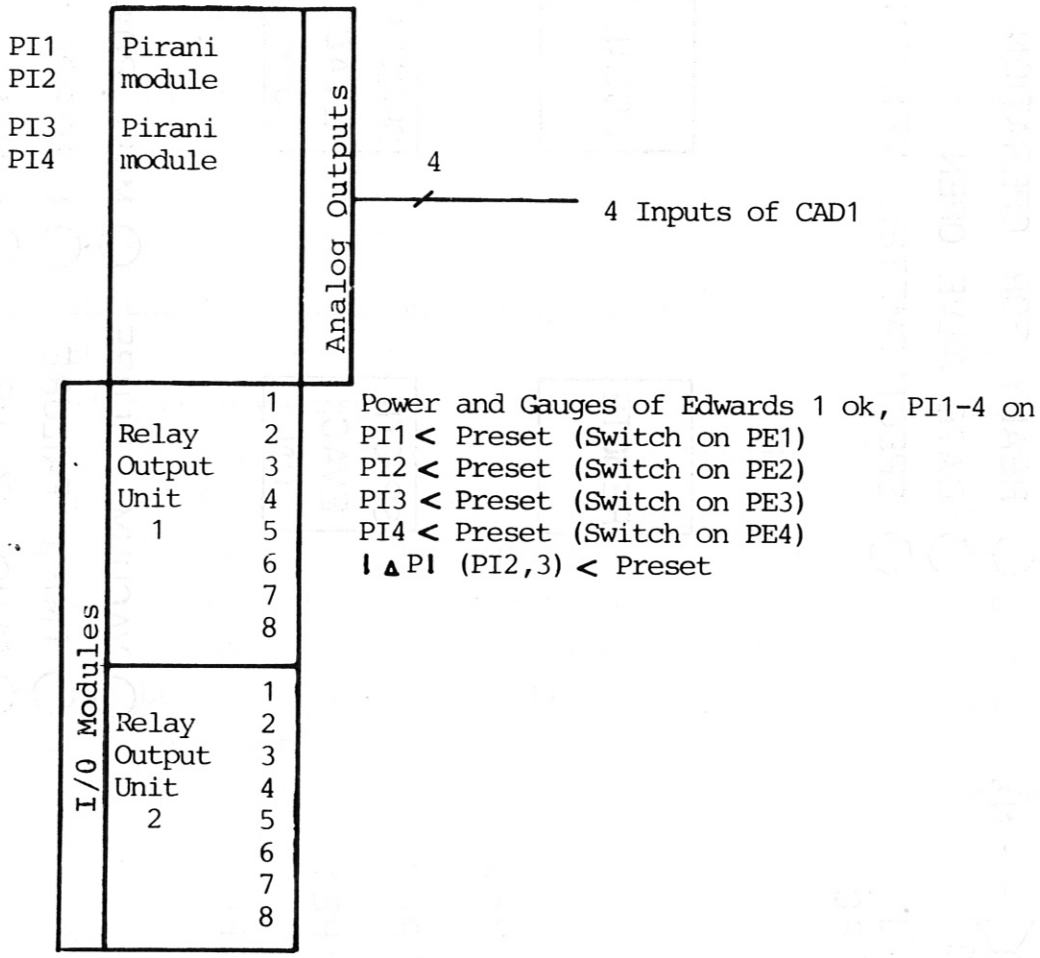

Fig. 33 Connections of Edwards controller 1

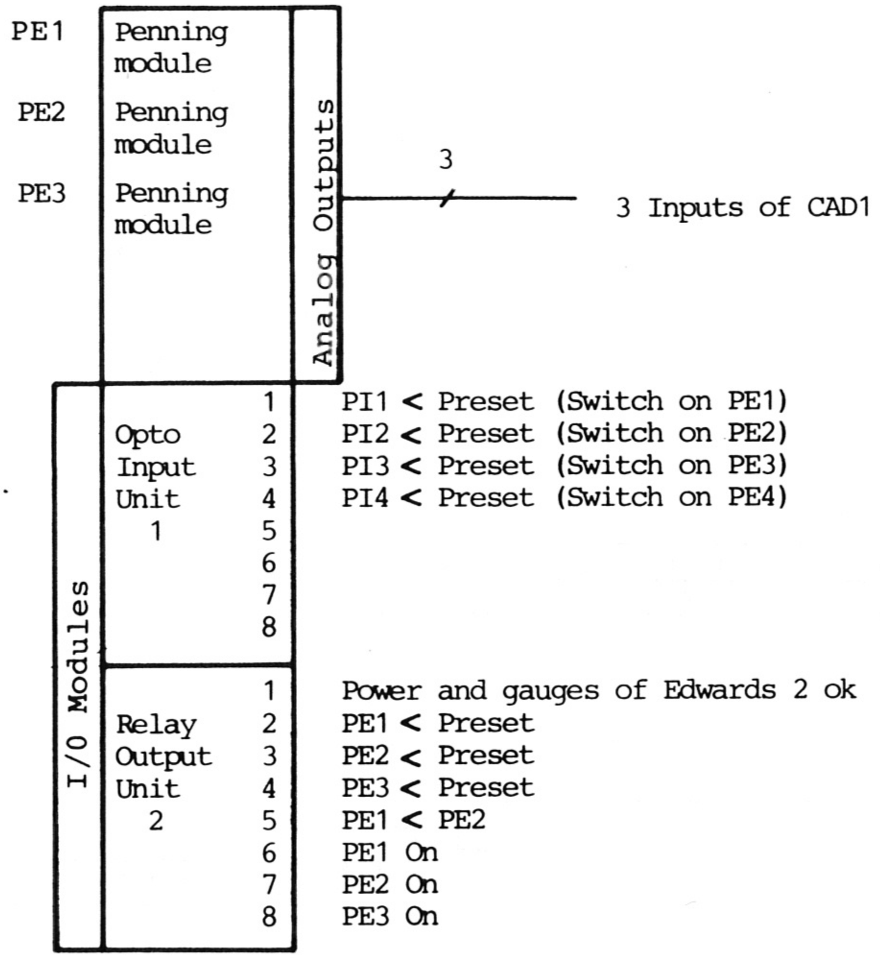

Fig. 34 Connections of Edwards controller 2

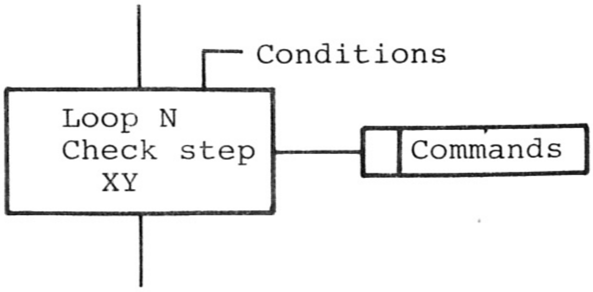

is equivalent to:

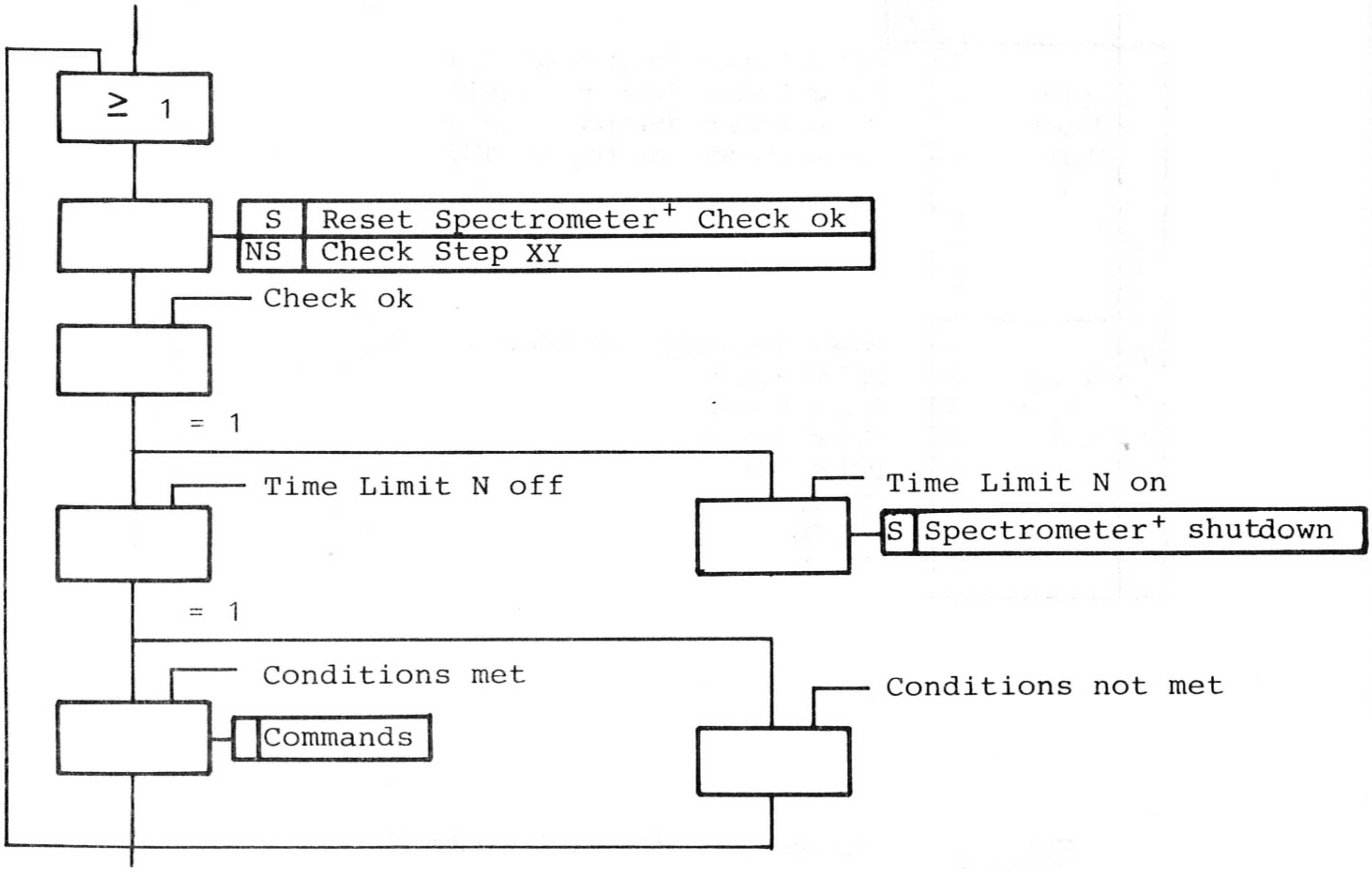

[+] Replace by Beam Line in the beam line system

Fig.35 Explanation of the symbolic representation of time loops used in the vacuum flow chart

1. Select mode of operation

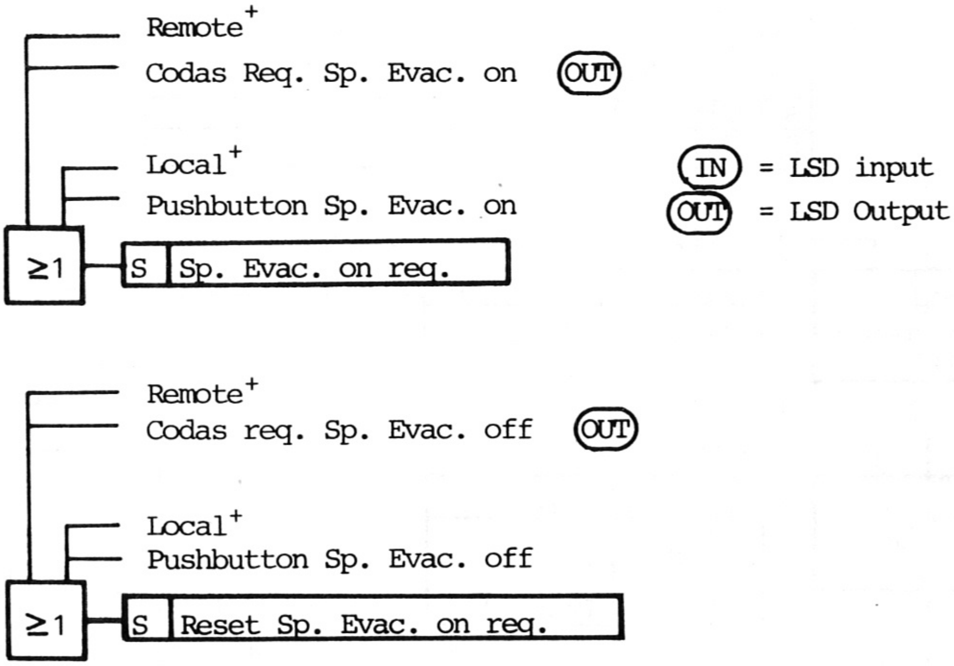

[+] Local-Remote interlock according to CODAS interface specifications (4 LSD inputs, 2 LSD outputs)

Fig. 36 /1 Flow Chart of vacuum control system

2. Spectrometer evacuation

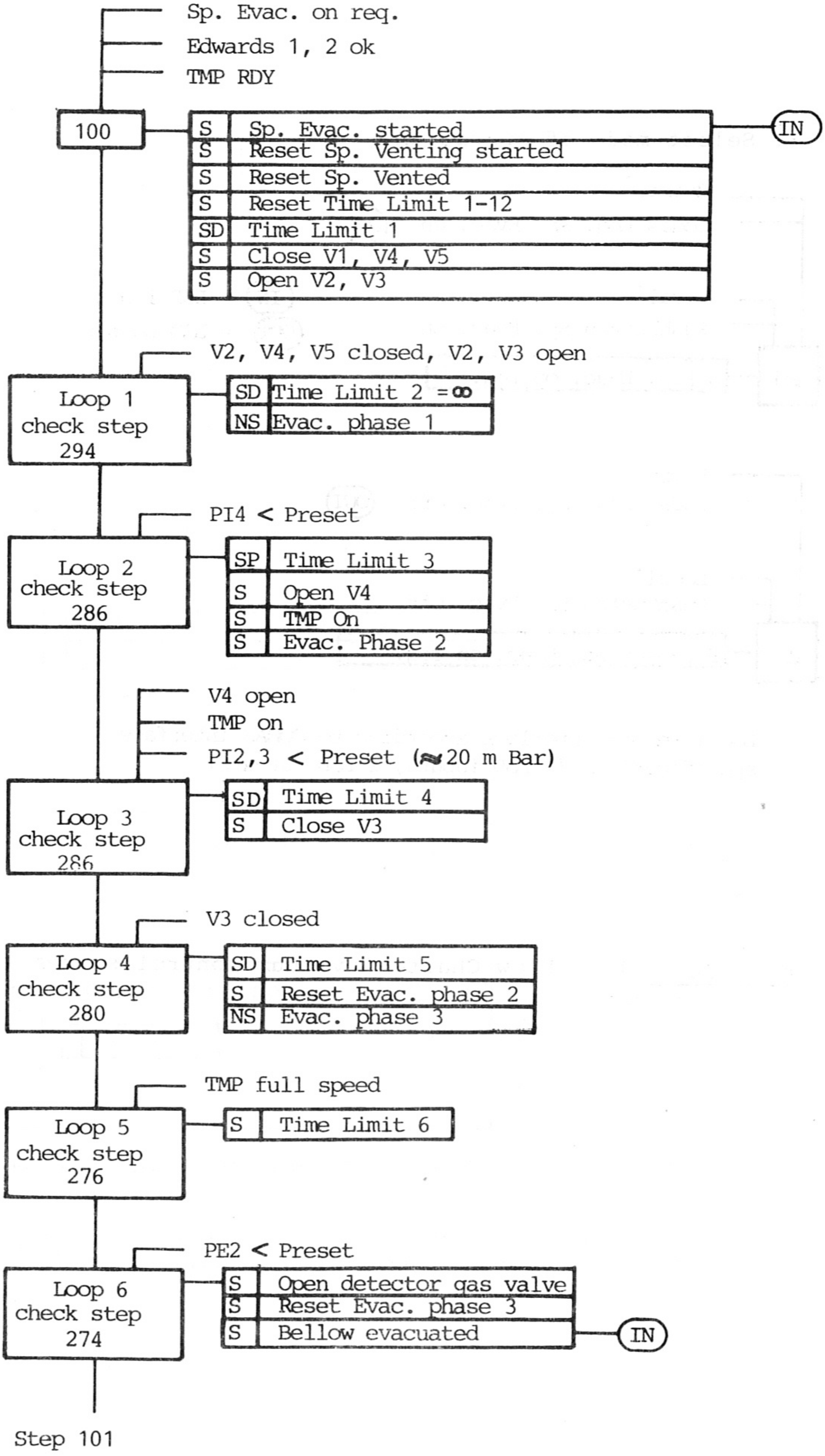

Fig. 36 / 2

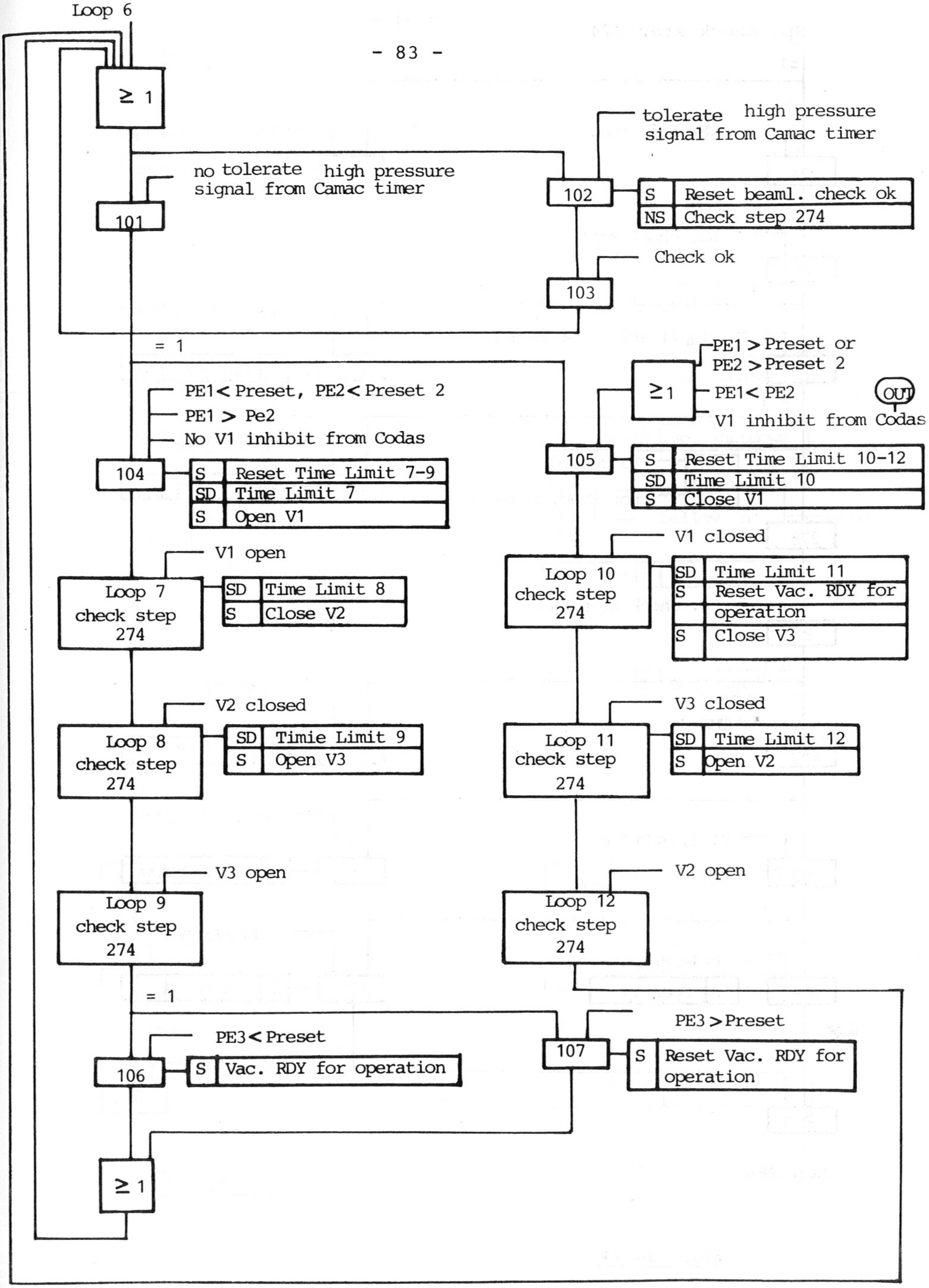
Loop 6
≥ 1
no tolerate high pressure signal from Camac timer
101
tolerate high pressure signal from Camac timer
102
S | Reset beaml. check ok
NS | Check step 274
Check ok
103
= 1
PE1 < Preset, PE2 < Preset 2
PE1 > Pe2
No V1 inhibit from Codas
104
S | Reset Time Limit 7-9
SD | Time Limit 7
S | Open V1
PE1 > Preset or
PE2 > Preset 2
PE1 < PE2
V1 inhibit from Codas
OUT
≥1
105
S | Reset Time Limit 10-12
SD | Time Limit 10
S | Close V1
V1 open
Loop 7 check step 274
SD | Time Limit 8
S | Close V2
V1 closed
Loop 10 check step 274
SD | Time Limit 11
S | Reset Vac. RDY for operation
S | Close V3
V2 closed
Loop 8 check step 274
SD | Timie Limit 9
S | Open V3
V3 closed
Loop 11 check step 274
SD | Time Limit 12
S | Open V2
V3 open
Loop 9 check step 274
V2 open
Loop 12 check step 274
= 1
PE3 < Preset
106
S | Vac. RDY for operation
PE3 > Preset
107
S | Reset Vac. RDY for operation
≥ 1

Fig. 36 /3

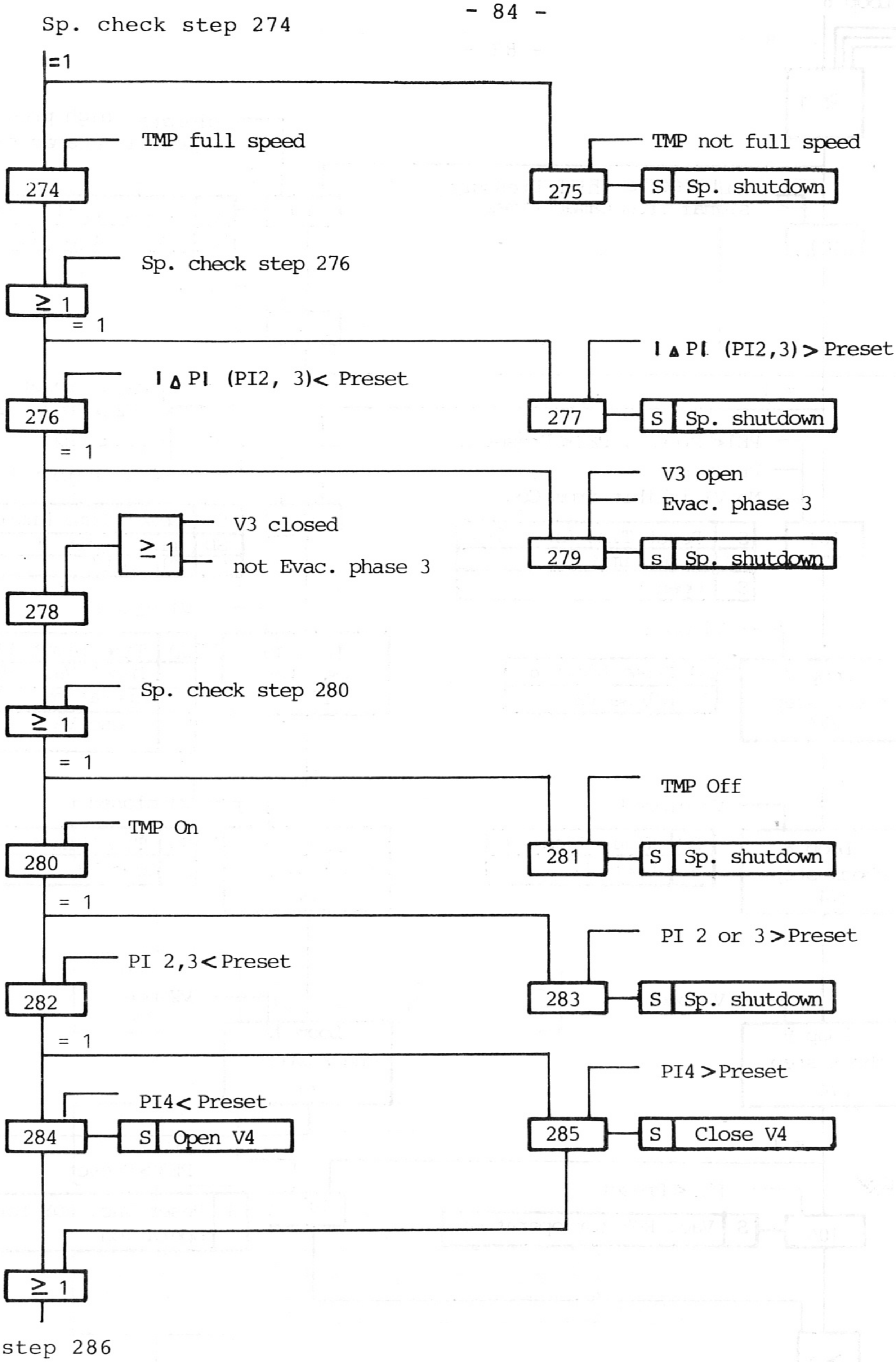
Sp. check step 274
=1
TMP full speed
274
TMP not full speed
275
S
Sp. shutdown
Sp. check step 276
≥ 1
= 1
| Δ P | (PI2, 3) < Preset
276
| Δ P | (PI2,3) > Preset
277
S
Sp. shutdown
= 1
V3 open
Evac. phase 3
≥ 1
V3 closed
not Evac. phase 3
279
s
Sp. shutdown
278
Sp. check step 280
≥ 1
= 1
TMP Off
TMP On
280
281
S
Sp. shutdown
= 1
PI 2 or 3 > Preset
PI 2,3 < Preset
282
283
S
Sp. shutdown
= 1
PI4 > Preset
PI4 < Preset
284
S
Open V4
285
S
Close V4
≥ 1
step 286

Fig. 36 /4

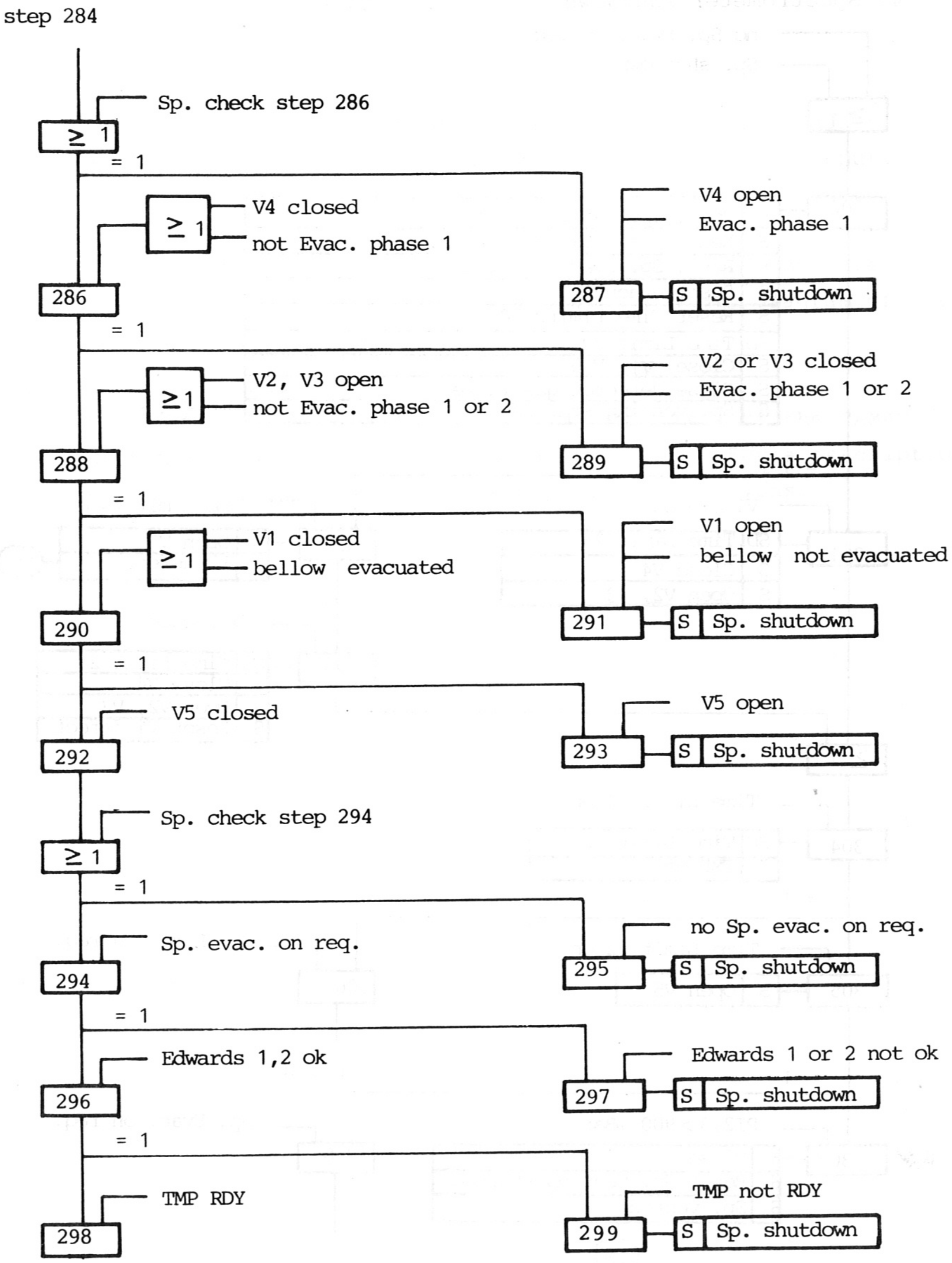
step 284
Sp. check step 286
≥ 1
= 1
V4 closed
not Evac. phase 1
≥ 1
286
V4 open
Evac. phase 1
287
S
Sp. shutdown
= 1
V2, V3 open
not Evac. phase 1 or 2
≥1
288
V2 or V3 closed
Evac. phase 1 or 2
289
S
Sp. shutdown
= 1
V1 closed
bellow evacuated
≥ 1
290
V1 open
bellow not evacuated
291
S
Sp. shutdown
= 1
V5 closed
292
V5 open
293
S
Sp. shutdown
Sp. check step 294
≥ 1
= 1
Sp. evac. on req.
294
no Sp. evac. on req.
295
S
Sp. shutdown
= 1
Edwards 1,2 ok
296
Edwards 1 or 2 not ok
297
S
Sp. shutdown
= 1
TMP RDY
298
TMP not RDY
299
S
Sp. shutdown

Fig.36 /5

4. Spectrometer shutdown

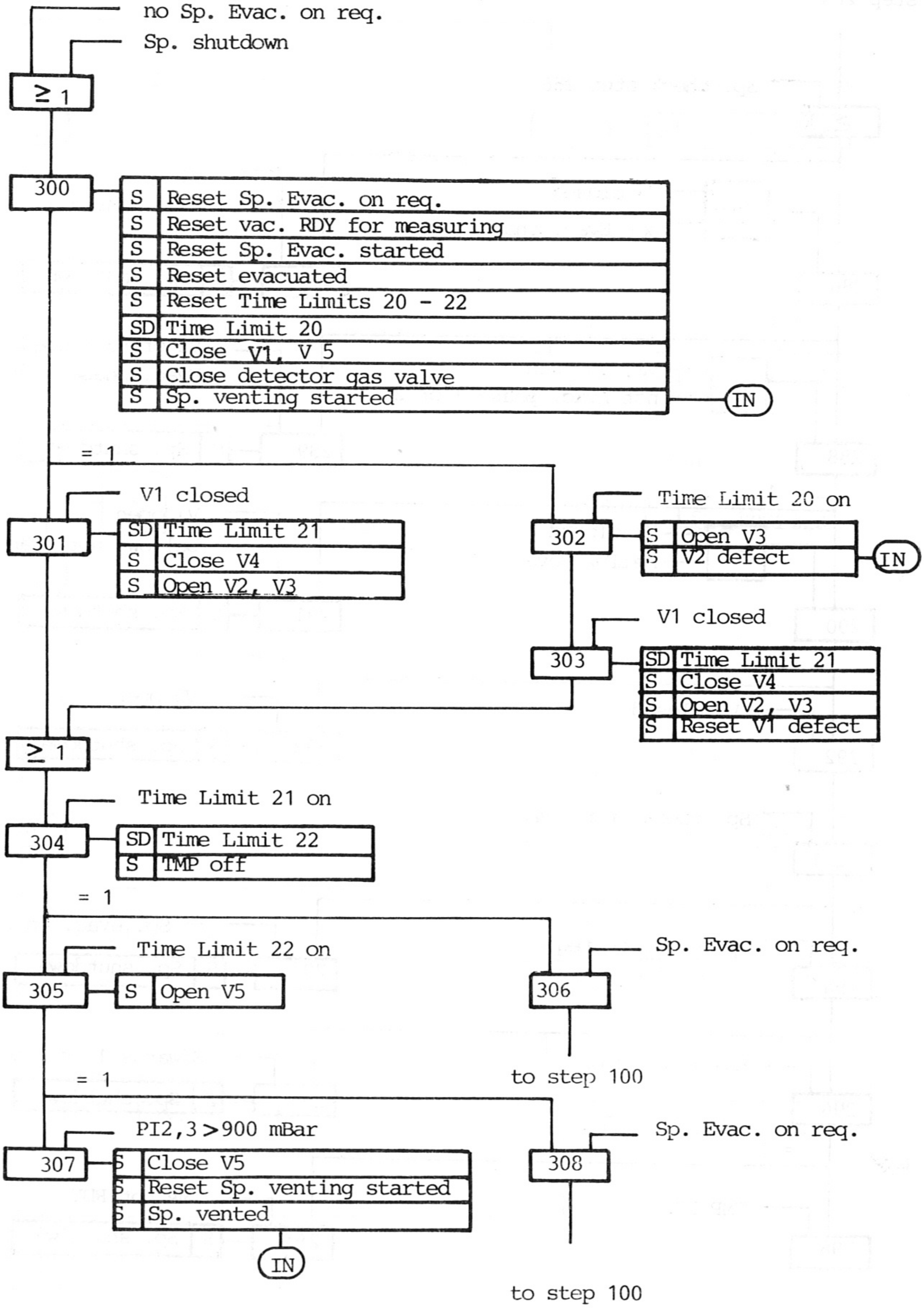

Fig. 36 /6

4.4.1 Connection to CODAS

The connection to CODAS is shown in Fig. 37. The vacuum values measured by the Edwards controllers are passed on to the inputs of a 16-channel CAMAC ADC via analog outputs. Control and feedback signals between CODAS and the Simatic control system are exchanged via LSD. In addition status signals of all vacuum elements are connected to LSD inputs in order to generate a mimic diagram of the vacuum system in the control room.

4.5 Control and data acquisition

A block diagram of the electronic systems and lists of the CAMAC and LSD components are given in Fig. 37 to 39 . For a description of the electronic sub-systems see the preceding sections.

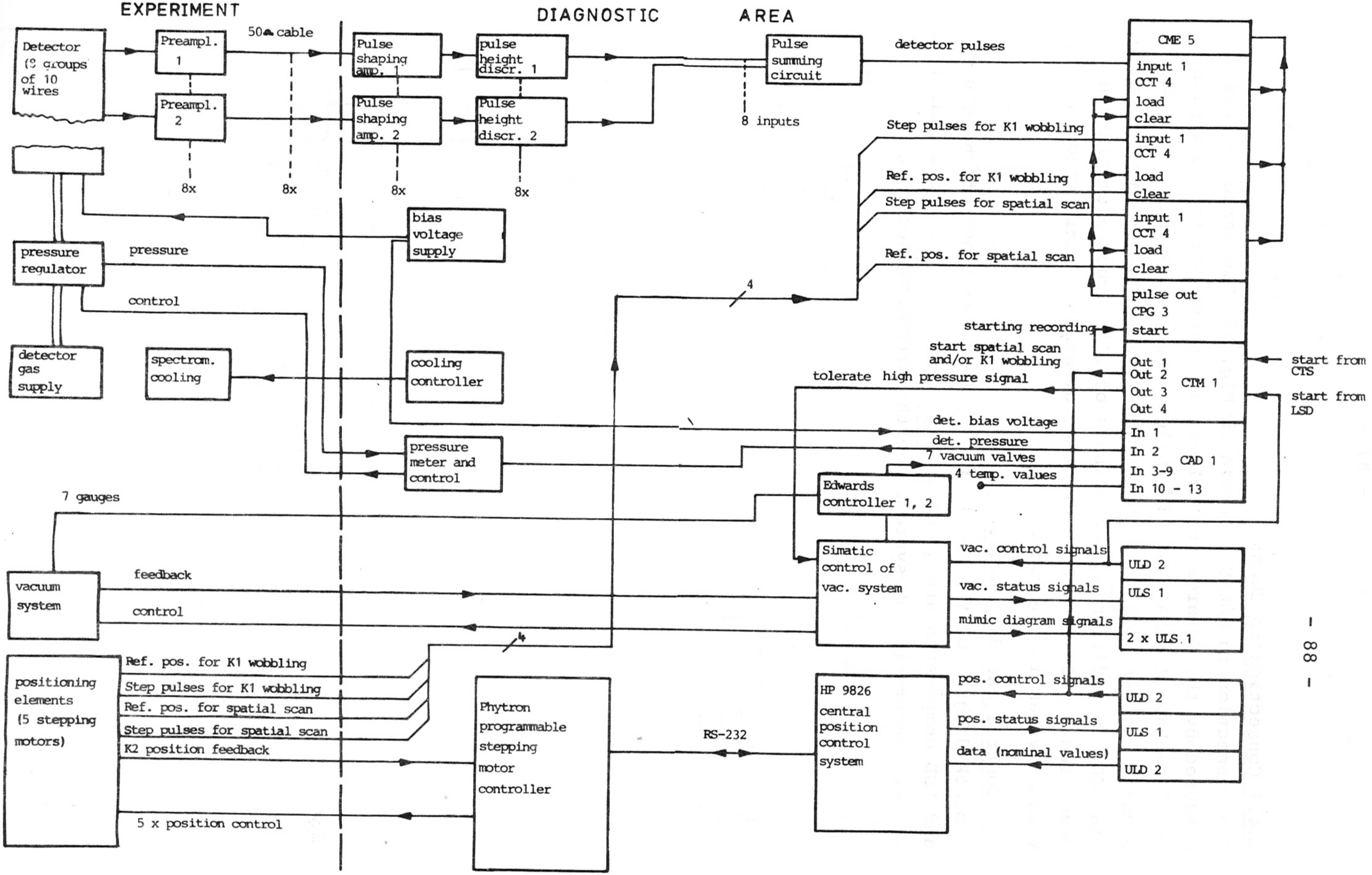

Fig. 37 Block diagram of the electronic systems

connected system	function	
	memory for 3 x CCT 4	CME 5
detector	measure detector pulses	CCT 4
positioning system	measure K2 wobbling position	CCT 4
positioning system	measure spatial scan position	CCT 4
	generate a sequence of load pulses for 3 x CCT 4	CPG 3
vacuum and positioning system	timing of data acquisition vacuum and positioning system	CTM 1
detector, vac.system, temp. probes	monitor 13 analog values	CAD 1
	control of LSD subrack	CLS 2
	crate controller	CCC 2

Fig. 38 Complement of CAMAC crate

CCB 1

vacuum control signals	ULD 2
vacuum status signals	ULS 1
mimic diagram signals	ULS 1
	ULS 1
position control signals	ULD 2
position status signals	ULS 1
nominal position values	ULD 2
connector card	ULC 1
power supply	UPS 1

Fig. 39 Complement of LSD subrack

Acknowledgements

The authors acknowledge the continuous interest and help of Drs. W. Engelhardt, E. Källne, M. Kaufmann and G. Magyar. They thank C. Höss, H. Hopper, Dr. K. Evans, E. Pfeffermann, Dr. G. Rupprecht and G. Schmitt for support and help with the tests. They are especially indepted to Frau Chr. Röder, A. Nicol and S. Ertl for the preparation of the report.

References

/1/ C. Breton, C. DeMichelis, M. Finkenthal, M. Mattioli, "Ionization Equilibrium of Selected Elements from Neon to Tungsten of Interest in Tokamak Plasma Research", EUR-CEA-FC-948 (1978)

/2/ H.W. Drawin, "Plasma Impurities and Cooling", Atomic and Molecular Data for Fusion, IAEA-199, p. 217 (1977)

/3/ W. Engelhardt, J. Fink, G. Fußmann, H. Krause, H.-B. Schilling, U. Schumacher, MPI für Plasmaphysik Report IPP 1/212, IPP III/81 (March 1982)

/4/ S. von Goeler, M. Bitter, S. Cohen, D. Eames, K. Hill, D. Hillis, R. Hulse, G. Lenner, D. Manos, Ph. Roney, W. Roney, N. Sauthof, S. Sesnic, W. Stodiek, F. Tenney, J. Timberlake, Proc. Diagnostics for Fusion Reactor Conditions, Vol. I, EUR 8351-I EN (Varenna 1982), p. 109-127

/5/ B.C. Fawcett, Atomic Data and Nuclear Data Tables 30, 1-26 (1984)

/6/ A.J. Burek, Space Science Instrumentation 2, 53 (1976)

/7/ Z. Hussain, E. Umbach, D.A. Shirley, J. Stöhr, J. Feldhaus, Nucl. Instr. and Meth. 195, 115 (1982)

/8/ K. Kohra, M. Audo, T. Matsushita, H. Hashizume, Nucl. Instr. and Meth. 152, 161 (1978)

/9/ J.H. Beaumont and M. Hart, J. Phys. E:Scient. Instr. 7, 823 (1974)

/10/ B. Yaakobi, A.J. Burek, Laboratory of Laser Energetics Report No. 139, University of Rochester (January 1983)

/11/ M. Cantin, L. Koch-Miramond, B. Mougin, R. Roccia, Proc. Workshop on X-ray Astronomy in the 1980's, NASA Technical Memorandum 83848, p. 523 (Nov. 1981)

/12/ D.B. Brown, M. Fatemi, L.S. Birks, J. Appl. Phys. 45, 1555 (1974)

/13/ J.A. Bearden, A. Hening, Rev. Sci. Instr. 36, 334 (1965)

/14/ R. Bartiromo, R. Gianella, private communication

/15/ R.D. Deslattes, private communication

/16/ E. Lell, N.J. Kreidl, J.R. Hensler, in Progress in Ceramic Science, Vol. 4 (J.E. Burke, ed.), p. 3 (1966), Pergamon Press, Oxford

/17/ R. Jenkins, X-ray Spectr. 1, 23 (1972)

/18/ J. Stöhr, V. Rehn, I. Lindau, R.Z. Bachrach, Nucl. Instr. and Meth. 152, 43 (1978)

/19/ N.G. Alexandropoulos, G.G. Cohen, Appl. Spectroscopy 28, 155 (1974)

/20/ G. Materlik, private communication

/21/ L. Koch-Miramond, private communication

/22/ U. Bonse, I. Hartmann, Z.f.Kristallographie 156, 265 (1981)

/23/ A. Roth, Vacuum Technology, North-Holland Publishing Company 1976, p. 435

/24/ U. Hauser, W. Kerler, Rev. Sci.Instr. 29, 380 (1958)

/25/ H. Johnson, R. Deslattes, Rev. Sci.Instr. 36, 1310 (1965)

/26/ D. Christ, Dr. Rudolph and Prof. Schmal, private communication

/27/ E.Pfeffermann, U. Briel, Adv. Space Res. 2, 255 (1983)

/28/ F. Briggs, R. Lighthill, Report Sandia SC-RR-7105707, Albuquerque/USA (1971)

/29/ G. Charpak, R. Bouclier, T. Bressani, J. Favier, C. Zupancic, Nucl. Instr. Meth. 62, 262 (1968)

/30/ F. Sauli, "Principles of operation of Multiwire Proportional and Drift Chambers", Report CERN 77-09, Geneva 1977

/31/ R.A. Boie, J. Fischer, Y. Inagaki, F.C. Merritt, V. Radeka, L.D. Rogers, D.M. Xi, Nucl. Instr. Meth. 201, 93 (1982)

/32/ J. Källne, E. Källne, L.G. Acentio, C.L. Morris, A.C. Thompson, Nucl. Instr. Meth. 203, 415 (1982)

/33/ R.L. Blake, private communication

/34/ H. Bradt et al., Space Sci. Rev. 8, 471 (1968)

/35/ D.L. McKenzie, P.B. Landecker, J.H. Underwood, Space Science Instrumentation 2, 125 (1976)

/36/ A.F. Avery, Levels of Radiation at JET, 3 Feb. 1982, RPD/AFA/613, marked "Draft, not for publication"

/37/ W.W. Engle, Jr., A User's Manual for ANISN, Report K-1693, Union Carbide Corp., Nucl. Div., Oak Ridge, Tenn. 1967

/38/ RSIC Data Library Collection: Coupled 100-Group Neutron 21 Group Gamma-Ray Cross Sections for EPR Neutronics, Contributed by Neutron Physics Div., Oak Ridge Nat. Lab., Oak Ridge, Tenn.

/39/ H. Brockmann et al., 1D Radiation Analysis for the Fusion Ignition Experiment ZEPHYR, IPP Report IPP 1/173, Nov. 1979

<u>List of drawings</u> (handed over to JET)

Drawing No.

Design of double-crystal spectrometer	S5 DKS-001000
Crystal 1, general view	S5 DKS-001001
Crystal 2, general view	S5 DKS-001002
Vessel with collimator	S5 DKS-001003
Calibration arrangement K1	S5 DKS-001004